

Convective-Reactive Nucleosynthesis in Oxygen-Carbon Shell Mergers

by

Joshua Issa

B.Sc., University of Waterloo, 2023

A Thesis Submitted in Partial Fulfillment of the
Requirements for the Degree of

MASTER OF SCIENCE

in the Department of Physics and Astronomy

© Joshua Issa, 2025
University of Victoria

All rights reserved. This Thesis may not be reproduced in whole or in part, by photocopying or other means, without the permission of the author.

Convective-Reactive Nucleosynthesis in Oxygen-Carbon Shell Mergers

by

Joshua Issa
B.Sc., University of Waterloo, 2023

Supervisory Committee

Dr. F. Herwig, Supervisor
(Department of Physics and Astronomy University of Victoria)

Dr. I. Dillmann, Supervisor
(Department of Physics and Astronomy University of Victoria, Research Scientist at TRI-UMF)

Abstract

O-C shell mergers in massive stars are a site for the production of the p-nuclei via the γ -process. During these mergers, the ingested C-shell material undergoes convective-reactive nucleosynthesis in the O-burning shell where the timescales for advection and nuclear reactions become equal. 1-D stellar models rely on the predictions of mixing length theory which does not match the results of 3-D hydrodynamic simulations in this region. In this paper, we use the $M_{\text{ZAMS}} = 15M_{\odot}$, $Z = 0.02$ model from the NuGrid stellar data set Ritter et al. (2018b) to create a detailed post-processed model of the O-shell during a merger event to investigate how 3-D macrophysics impacts nucleosynthesis. This is done by introducing a convective downturn at the bottom of the O-burning shell, varying the rate of ingesting C-shell material, and implementing a dip in the diffusion profile due to both a GOSH-like event and partial merger. In addition to this, we also investigate the impact of varying the input nuclear physics of all photo-disintegration reactions of unstable p-heavy isotopes from Se–Po by a factor of 10 up and down in a Monte Carlo way in various mixing conditions. The results show that the mixing details have a significant impact on the production of the p-nuclei and influence the impact of the nuclear physics. Introducing a convective downturn has a non-linear, non-monotonic impact on the production of the p-nuclei, with an average spread of 0.96 dex between MLT and downturn scenarios. Increasing the C-shell ingestion rate is found to increase production and has a spread in production of 1.22 – 1.84 dex across MLT and convective downturn scenarios. GOSH-like and partial merger dips were found to decrease production in a uniform way by and has a spread in production including MLT of 0.51 dex. Finally, the nuclear physics impact was found to have cause a spread in the final mass fraction on average 0.56 – 0.79 dex across mixing scenarios which is similar to the spread across the various mixing scenarios. Additionally, we find whether there is a correlation and the strength of it are both dependent on the mixing scenario. We conclude that understanding the mixing details of the O-C shell merger along with the nuclear physics is critical for understanding the production of p-nuclei and that there are comparable model uncertainties as the nuclear physics.

Table of Contents

Supervisory Committee	ii
Abstract	iii
Table of Contents	iv
List of Tables	vi
List of Figures	vii
Acknowledgements	xiii
Dedication	xiv
1 Introduction	1
1.1 Motivation	1
1.2 Stellar Nucleosynthesis in Massive Stars	2
1.2.1 Hydrostatic Burning Phases	2
1.2.2 Neutron Capture Processes	4
1.2.3 <i>p</i> -Nuclei Nucleosynthesis	5
1.2.4 Convective-Reactive Nucleosynthesis	6
1.3 Massive Star Evolution	6
1.3.1 O-C Shell Mergers	8
1.4 1-D Stellar Modelling	8
1.4.1 Mixing Length Theory Approximation	14
1.4.2 Stellar Evolution with MESA	15
1.4.3 Post-Processing with mppnp	15
1.5 3-D Macrophysics	16
1.5.1 Insufficiencies of MLT	18
1.5.2 3-D Simulations of Convective O-Shell Burning and C-Shell Entrainment	18

1.5.3	1-D Implementation of 3-D Hydrodynamics	22
1.6	Thesis Outline	23
2	Impact of 3D-macrophysics and nuclear physics on p-nuclei nucleosynthesis in O–C shell mergers	25
2.1	Introduction	25
2.2	Methodology	28
2.2.1	1-D implementation of 3-D macrophysics	30
2.2.2	Determining nuclear physics impact	35
2.3	Correlations of nuclear reaction rates	35
2.4	Results	38
2.4.1	Convective-reactive production of the p-nuclei	38
2.4.2	Mixing scenario 1: Convective downturns	42
2.4.3	Mixing scenario 2: Varying the ingestion rate	44
2.4.4	Mixing scenario 3: Convective dips from GOSH-like feedback and a partial merger	50
2.4.5	Nuclear physics impact and mixing dependencies	51
2.5	Discussion	55
2.6	Conclusion	67
3	Investigations Beyond the <i>p</i>-Nuclei	69
3.1	Light Odd-Z Isotope Production	69
3.1.1	The Relevance of K	69
3.2	Advective-Reactive <i>r</i> -process	69
4	Summary and Conclusion	73
Bibliography		74

List of Tables

Table 1.1 Details about hydrostatic burning phases in massive stars taken from the $13\text{-}25M_{\odot}$ stars in Table 1 of Woosley et al. (2002)	3
Table 2.1 Reactions correlated with the production/destruction of an isotope unique to an individual mixing scenario.	56
Table 2.2 Reactions correlated with the production/destruction of an isotope shared across all mixing scenarios.	57
Table 2.3 Correlations and ζ slopes between mass fraction and reaction rates for the MLT mixing scenario.	58
Table 2.4 Correlations and ζ slopes between mass fraction and reaction rates for the 3D-inspired mixing scenario.	59
Table 2.5 Correlations and ζ slopes between mass fraction and reaction rates for the 3×3 D-inspired mixing scenario.	60
Table 2.6 Correlations and ζ slopes between mass fraction and reaction rates for the 10×3 D-inspired mixing scenario.	61
Table 2.7 Correlations and ζ slopes between mass fraction and reaction rates for the 50×3 D-inspired mixing scenario.	62

List of Figures

Figure 1.1 Taken from Prialnik (2009) Figure 9.19: Schematic structure of a supernova progenitor star.	7
Figure 1.2 Kippenhahn diagram showing the merger of the convective O and C-burning shells for the $15M_{\odot}$ $Z = 0.02$ model from Ritter et al. (2018b). The O-burning shell extends from $1.55M_{\odot}$ to $1.95M_{\odot}$. The first convective C-burning shell sits directly on top from $1.96M_{\odot}$ to $2.11M_{\odot}$ and additional convective C-burning shells that are subsumed are above. The merger onsets at $\log_{10}(t - t_{\text{end}})/\text{yr} \approx -3.85$ and reaches full extent at ≈ -4	9
Figure 1.3 Evolution of the mass fraction of ^{12}C , ^{16}O , ^{20}Ne , and ^{35}Cl in a convective-reactive environment at the same simulation time with different timesteps. The solid line corresponds to a simulation with timestep of $\Delta t = 0.5\text{s}$, the dashed line corresponds to $\Delta t = 0.1\text{s}$, and the dotted line corresponds to $\Delta t = 0.01\text{s}$	17
Figure 1.4 O-burning shell of the $15M_{\odot}$ $Z = 0.02$ model from Ritter et al. (2018b) at model number 9200 right before the merger with C-shell is fully realized. The O-shell is from 2.79 Mm to 7.49 Mm, the merger region is from 7.49 Mm to 8.56 Mm, and the C-burning shell is from 8.56 Mm to 18 Mm.	19

Figure 1.5 Taken from Jones et al. (2017): Time-averaged radial diffusion coefficient profile calculated from the spherically averaged abundance profiles by the method described in Section 3.5 (brown solid line; black solid line is a fit to the noisy region). The convective velocities computing using MLT agree with the spherically averaged 3D velocities to within about a factor of 2 inside the convection zone but are too large in the vicinity of the CB, resulting in an overestimation of the diffusion coefficient there. Limiting the mixing length to the distance from the CB reproduces the fall-off of the diffusion coefficient inside the convection zone approaching the boundary which is seen in the spherically averaged 3D simulation results.

21

Figure 2.1 Kippenhahn diagram showing the merger of the convective O and C-burning shells. The O-burning shell extends from $1.55M_{\odot}$ to $1.95M_{\odot}$. The first convective C-burning shell sits directly on top from $1.96M_{\odot}$ to $2.11M_{\odot}$ and additional convective C-burning shells that are subsumed are above. The merger onsets at $\log_{10}(t - t_{\text{end}})/\text{yr} \approx -3.85$ and reaches full extent at ≈ -4

29

Figure 2.2 The diffusion coefficient profile predicted by MLT at model number 9160 for the $M_{\text{ZAMS}} = 15M_{\odot}$, $Z = 0.02$ model and the forced merger profile for the O-shell. The red line with triangles is the MLT prediction and the blue line is the forced merger. The black lines are the boundaries of the convective O-burning shell.

31

Figure 2.3 The diffusion coefficient profiles for the 3D-inspired mixing scenarios. The blue dashed line is the merged D_{MLT} profile, the orange line with diamonds, green line with triangles, red line with red circles, and purple line with squares are those calculated using $D_{\text{3D-insp.}}$ with boost factors of 1, 3, 10, and 50 respectively.

33

Figure 2.4 The MLT, GOSH-like, and partial merger diffusion coefficient profiles. The blue dashed line is D_{MLT} , the pink line with triangles and lime line are potential GOSH-like splits in the profile centered at $r = 4.95$ Mm, the purple line has a dip that is $10\times$ deeper. The brown line with circles and the turquoise line are partial mergers $r = 7.5$ Mm, the gray line has a dip that is $10\times$ deeper. The black dashed lines are the edges of the O-shell.

34

Figure 2.5 Examples of strongly correlated mass fractions with reaction rates for four species for the MLT mixing scenario. The blue dots are the values and the red line is the best linear fit to OP_{var} and $\log_{10}(\text{variation factor})$. The top left plot and bottom right plot show strong correlations for ^{74}Se and ^{196}Hg that directly impact the mass fraction. The top right plot shows a correlation for ^{98}Ru where there is considerable spread in the mass fraction. The bottom left plot shows a correlation for ^{184}Os where the mass fraction is strongly affected only for multiplication factors less than 1.

36

Figure 2.6 Nucleosynthetic flux and mass fraction plot for the MLT mixing case at $t = 110$ sec. The blue solid line and brown dashed line are $^{75}\text{Se}(\gamma, n)^{74}\text{Se}$ and $^{74}\text{Se}(n, \gamma)^{75}\text{Se}$ respectively. The red solid line with triangles and black solid line with circles are the mass fractions of ^{74}Se and ^{75}Se respectively.

37

Figure 2.7 Temperature profile and mass fractions after $t = 110$ sec of ingestion for the MLT mixing scenario. The grey solid line is the temperature, the blue solid line with circles is ^{74}Se , the orange dashed line with triangles is ^{92}Mo , the green dotted line with squares is ^{136}Ce , the pink solid line with diamonds is ^{144}Sm , the brown dashed line with circles is ^{156}Dy , and the purple dotted line with triangles is ^{196}Hg

39

Figure 2.8 Nucleosynthetic fluxes f_{ij} at $m = 1.55103M_{\odot}$ for the MLT scenario for $t = 110$ sec of ingestion at 2.833 GK.

40

Figure 2.9 Nucleosynthetic fluxes f_{ij} at $m = 1.58017M_{\odot}$ for the MLT scenario for $t = 110$ sec of ingestion at 2.621 GK.

41

Figure 2.10 The overproduction compared to the solar measurement of the p-nuclei. The blue circle corresponds to the MLT scenario, orange diamond to the 3D-inspired scenario, green square to 3×3D-inspired scenario, right side up red triangle to 10×3D-inspired, and upside down purple triangle to 50×3D-inspired. The thick grey line at $OP = 0$ corresponds to the solar measurement. The average spread in production is 0.96 dex.

43

Figure 2.11 Overproduction compared to solar for the MLT mixing scenario for each ingestion rate. The circle with a black outline corresponds to the base ingestion rate $4 \times 10^{-3} M_{\odot} s^{-1}$, which is the same as the MLT values in Figure 2.10. The square corresponds to a rate of $4 \times 10^{-4} M_{\odot} s^{-1}$, the diamond corresponds to a rate of $4 \times 10^{-5} M_{\odot} s^{-1}$, and the triangle corresponds to no ingestion of C-shell material. The thick grey line at OP = 0 corresponds to the solar measurement. The average spread in production excluding the no ingestion scenario is 1.22 dex.

45

Figure 2.12 Overproduction compared to solar for the 3D-inspired mixing scenario for each ingestion rate. The diamond with a black outline corresponds to the base ingestion rate $4 \times 10^{-3} M_{\odot} s^{-1}$, which is the same as the 3D-inspired values in Figure 2.10. The square corresponds to a rate of $4 \times 10^{-4} M_{\odot} s^{-1}$, the circle corresponds to a rate of $4 \times 10^{-5} M_{\odot} s^{-1}$, and the triangle corresponds to no ingestion of C-shell material. The thick grey line at OP = 0 corresponds to the solar measurement. The average spread in production excluding the no ingestion scenario is 1.58 dex.

46

Figure 2.13 Overproduction compared to solar for the 3×3 D-inspired mixing scenario for each ingestion rate. The square with a black outline corresponds to the base ingestion rate $4 \times 10^{-3} M_{\odot} s^{-1}$, which is the same as the 3×3 D-inspired values in Figure 2.10. The diamond corresponds to a rate of $4 \times 10^{-4} M_{\odot} s^{-1}$, the circle corresponds to a rate of $4 \times 10^{-5} M_{\odot} s^{-1}$, and the triangle corresponds to no ingestion of C-shell material. The thick grey line at OP = 0 corresponds to the solar measurement. The average spread in production excluding the no ingestion scenario is 1.65 dex.

47

Figure 2.14 Overproduction compared to solar for the 10×3 D-inspired mixing scenario for each ingestion rate. The triangle with a black outline corresponds to the base ingestion rate $4 \times 10^{-3} M_{\odot} s^{-1}$, which is the same as the 10×3 D-inspired values in Figure 2.10. The diamond corresponds to a rate of $4 \times 10^{-4} M_{\odot} s^{-1}$, the circle corresponds to a rate of $4 \times 10^{-5} M_{\odot} s^{-1}$, and the square corresponds to no ingestion of C-shell material. If a point would be plotted out of range, it is denoted with an arrow and its value. The thick grey line at OP = 0 corresponds to the solar measurement. The average spread in production excluding the no ingestion scenario is 1.78 dex.

48

Figure 2.15 Overproduction compared to solar for the $50 \times 3D$ -inspired mixing scenario for each ingestion rate. The upside down triangle with a black outline corresponds to the base ingestion rate $4 \times 10^{-3} M_{\odot} s^{-1}$, which is the same as the $50 \times 3D$ -inspired values in Figure 2.10. The diamond corresponds to a rate of $4 \times 10^{-4} M_{\odot} s^{-1}$, the circle corresponds to a rate of $4 \times 10^{-5} M_{\odot} s^{-1}$, and the square corresponds to no ingestion of C-shell material. If a point would be plotted out of range, it is denoted with an arrow and its value. The thick grey line at $OP = 0$ corresponds to the solar measurement. The average spread in production excluding the no ingestion scenario is 1.84 dex.

49

Figure 2.16 The overproduction of all p-nuclei with respect to the solar amount. The blue circle corresponds to the MLT scenario, pink diamond to GOSH-like scenario, lime square to deeper GOSH-like scenario, right side up brown triangle to partial merger scenario, and upside down turquoise triangle to deeper partial merger scenario. The thick grey line at $OP = 0$ corresponds to the solar measurement. The average spread in production is 0.51 dex.

50

Figure 2.17 Histogram showing the spread due to varying (γ, p) , (γ, n) , (γ, α) and corresponding capture rates for unstable p-heavy isotopes from Se-Po for the MLT mixing scenario. Colour and size correspond to the logarithmic binning of Monte Carlo runs. The thick grey line at $OP = 0$ corresponds to the solar measurement. The average spread in production is 0.56 dex.

52

Figure 2.18 Histogram showing the spread due to varying (γ, p) , (γ, n) , (γ, α) and corresponding capture rates for unstable p-heavy isotopes from Se-Po for the $3D$ -inspired mixing scenario. The thick grey line at $OP = 0$ corresponds to the solar measurement. The average spread in production is 0.59 dex.

53

Figure 2.19 Histogram showing the spread due to varying (γ, p) , (γ, n) , (γ, α) and corresponding capture rates for unstable p-heavy isotopes from Se-Po for the $3 \times 3D$ -inspired mixing scenario. The thick grey line at $OP = 0$ corresponds to the solar measurement. The average spread in production is 0.69 dex.

53

Figure 2.20 Histogram showing the spread due to varying (γ, p) , (γ, n) , (γ, α) and corresponding capture rates for unstable p-heavy isotopes from Se-Po for the $10 \times 3D$ -inspired mixing scenario. The thick grey line at OP = 0 corresponds to the solar measurement. The average spread in production is 0.76 dex.	54
Figure 2.21 Histogram showing the spread due to varying (γ, p) , (γ, n) , (γ, α) and corresponding capture rates for unstable p-heavy isotopes from Se-Po for the $50 \times 3D$ -inspired mixing scenario. The thick grey line at OP = 0 corresponds to the solar measurement. The average spread in production is 0.79 dex.	54
Figure 2.22 Maximum and minimum overproduction compared to solar for all convective downturn scenarios, GOSH-like scenarios, partial merger scenarios, and ingestion rates excluding the scenario of no C-shell ingestion. The thick grey line at OP = 0 corresponds to the solar measurement. The average spread in production is 2.45 dex.	63
Figure 2.23 Comparing the results of the grains data to the various mixing scenarios considered in this paper for $\delta(^{92}\text{Mo}/^{96}\text{Mo})$ and $\delta(^{94}\text{Mo}/^{96}\text{Mo})$. Grey points correspond to grains data with 1σ error bars and coloured points for the mixing scenarios.	65
Figure 2.24 Comparing the results of the grains data to the various mixing scenarios considered in this paper for $\delta(^{98}\text{Ru}/^{100}\text{Ru})$ and $\delta(^{96}\text{Ru}/^{100}\text{Ru})$. Grey points correspond to grains data with 1σ error bars and coloured points for the mixing scenarios.	66
Figure 3.1 In isotope timescale.	70
Figure 3.2 Pairwise distance.	71
Figure 3.3 Fraction of exchanging mass.	72

Acknowledgements

This thesis did not happen by accident, nor by some unique gift I alone have. I would like to thank of primary importance Dr. Falk Herwig and Dr. Iris Dillmann. Without your patience, teaching and supporting me through all my doubts and mistakes, this work would not have happened. Thank you for all the doors you have opened and the opportunities you have given me. I would also like to thank Dr. Pavel Denissenkov for his constant availability to answer all my programming questions and showing me how to use all the tools I needed to do this work. I am deeply grateful to have learned from you all.

To my parents, who have always been supportive of me. Thank you to my mother who taught me how to critically engage in the world and refuse to take things at face value. Thank you to my father who taught me what a life long dedication to learning looks like and insisting that I become a doctor of stars.

To Sneha, my companion. Words can't begin to express how grateful I am for your support and love, always being there and excited for every step that I have taken in this journey. Thank you for the FaceTime calls to wake me up in the morning, and the late night scrolls through Instagram together. Thank you for the motivation every day to work hard and shoot for the stars.

To Mr. Hordyk who told me I would do great things, Mr. Koiter who taught me physics and sparked my love for it, and Mr. Blyleven who took me from a student who couldn't program Hello World to helping me land my first programming job, thank you for shaping me to be the scientist I am today. I still hear your advice to this day, and I am the better for it.

To my friends in Victoria and Vancouver who have been there through the frustrations and the joys. Thank you Praneet, Maeve, Mallory, Daniel, Bryn, Diego, Dhwani, Layla, Aviv, Ruxin, and Jono. Grad school without you all would have been a sad and lonely place.

I acknowledge and respect the Lək'ʷəŋən (Songhees and Xʷsepsəm/Eskwimalt) Peoples on whose territory I live and work on, and the Lək'ʷəŋən and WSÁNEĆ Peoples whose historical relationships with the land continue to this day.

Well, I am just a humble theologian, and as far as I am concerned the whole of astronomy can be summed up by saying ‘Twinkle, twinkle little star, how I wonder what you are.’

- Karl Barth

Dedication

To my parents who taught me how to see the world, my high school teachers who gave me my passion for computational physics, and to my fiancée who has been my biggest supporter in grad school and in life. Thank you.

Chapter 1

Introduction

1.1 Motivation

1-D stellar evolution is a field that depends on the assumptions of spherical symmetry and mixing length theory. While these assumptions have some success describing the early nuclear burning stages of massive stars, they break down in the advanced burning stages (Bazan and Arnett, 1994). The convective O-burning shell and its potential merger with a convective C-burning shell are advanced burning stages shortly before the core collapse of a star where 1-D assumptions break down and 3-D hydrodynamics becomes necessary to model the macrophysical flows (Meakin and Arnett, 2007; Jones et al., 2017; Andrassy et al., 2020). This poses a problem for nucleosynthesis calculations, as the stellar structure can be complex, with asymmetric hotspots of burning leading to substantial differences in production compared to 1-D (Bazan and Arnett, 1994; Rizzuti et al., 2024a).

The p -nuclei are 35 proton-rich stable isotopes heavier than iron that are largely not produced in the neutron capture processes typical of these elements (Burbidge et al., 1957; Woosley and Howard, 1978). Although many astrophysical sites have been proposed for their production (Woosley and Hoffman, 1992; Schatz et al., 1998; Rauscher et al., 2002; Travaglio et al., 2015), no single site has been found to have the necessary conditions to produce all of the p -nuclei. One of the sites that has been found to produce the p -nuclei is the O-burning shell of a massive star first suggested in the context of a core collapse supernova by (Woosley and Howard, 1978). Since then, it has been found that pre-explosive O-shell burning is able to produce these nuclei during the O-C shell merger (Rauscher et al., 2002; Ritter et al., 2018a; Roberti et al., 2023). Additionally, it has been found that the nucleosynthesis in the O-C merger dominates the production of the p -nuclei regardless of the energy of the supernova explosion (Roberti et al., 2024), highlighting the importance of understanding this astrophysical site. Additionally, the O-C merger has been found to be a critical site for

the production of the odd-Z isotopes P, Cl, K, and Sc which have been underproduced in galactic chemical evolution models (Ritter et al., 2018a; Roberti et al., 2025).

The O-C shell merger is a 3-D hydrodynamic environment with large asymmetric flows and hotspots of burning that are not captured by 1-D stellar evolution models. This is problematic for understanding the peculiar nucleosynthesis of this region as current 1-D stellar evolution models rely on mixing length theory to describe the convective motions of this environment. The purpose of this work is to explore the impact on nucleosynthesis of varying the mixing conditions of the O-shell during C-shell entrainment, particularly for the *p*-nuclei.

1.2 Stellar Nucleosynthesis in Massive Stars

Stellar nucleosynthesis is the process by which elements are formed through nuclear reactions in stars. Burbidge et al. (1957) set the foundation for the field describing the synthesis of all elements in hydrostatic and explosive burning. From theoretical calculations, they described the nucleosynthesis of all isotopes in stars via a series of burning stages and nuclear processes while proposing the likely astrophysical sites. In the following years, through observational data and computational developments, the work remains a foundational text to stellar nuclear astrophysics.¹ Shortly after, Henyey et al. (1964) proposed a method for calculating nucleosynthesis of the CNO cycle in stars. Since then, the field has expanded to modelling the nucleosynthesis of isotopes during all stages of stellar evolution and produce data sets of stellar models at any mass and metallicity (Pignatari et al., 2016b; Ritter et al., 2018b; Battino et al., 2019).

1.2.1 Hydrostatic Burning Phases

Hydrostatic burning describes the nuclear fusion processes that occurs in during the lifetime of a star, where the energy produced by nuclear reactions balance the gravitational forces and allowing the star to maintain hydrostatic equilibrium. Each of these burning phases is characterized by a specific temperature, density, and timescale where the nucleosynthesis takes place.

¹One is reminded of Alfred North Whitehead's quote: *The safest general characterization of the European philosophical tradition is that it consists of a series of footnotes to Plato.* Or in our case, B²FH.

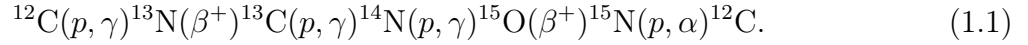
Table 1.1: Details about hydrostatic burning phases in massive stars taken from the $13\text{-}25M_{\odot}$ stars in Table 1 of Woosley et al. (2002)

Burning Phase	Temperature (10^7 K)	Density (g cm $^{-3}$)	Timescale (yrs)
H-burning	3.44 - 3.81	6.66 - 3.81	$13.5 - 6.70 \times 10^7$
He-burning	17.2 - 19.6	$1.73 - 0.762 \times 10^3$	$2.67 - 0.839 \times 10^7$
C-burning	81.5 - 84.1	$3.13 - 1.29 \times 10^5$	$2.82 - 0.522 \times 10^3$
Ne-burning	169 - 157	$10.8 - 3.95 \times 10^6$	0.341 - 0.891
O-burning	189 - 209	$8.19 - 3.60 \times 10^6$	4.77 - 0.402
Si-burning	328 - 365	$4.83 - 3.01 \times 10^7$	$48.8 - 2.0 \times 10^{-3}$

H-burning

H-burning is the first stage of hydrostatic burning in the core of a star. There are two processes by which this happens, the pp chain and the CNO cycle. In low mass stars

The conversion of hydrogen to helium via nuclear fusion occurs primarily through the proton-proton (pp) chains and the CNO cycles. In massive stars, the CNO cycle dominates due to higher central temperatures ($T \gtrsim 15 \times 10^6$ K):



The net result is four protons converted to a helium nucleus, releasing energy via positrons and neutrinos.

He-burning

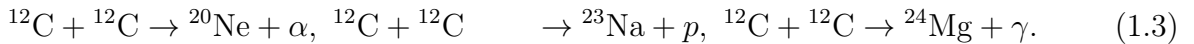
Once hydrogen is exhausted in the core, helium burning is ignited via the triple-alpha process:



The $^{12}\text{C}/^{16}\text{O}$ ratio has significant consequences for later burning stages and the final core structure. This phase operates at $T \sim 2 \times 10^8$ K.

C-burning

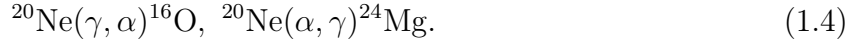
At $T \sim 6 \times 10^8$ K, carbon fusion begins:



This burning typically occurs in a convective core or shell, depending on the stellar mass and prior evolution.

Ne-burning

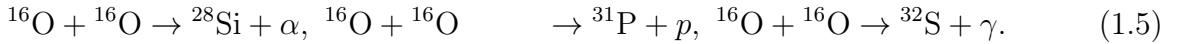
Neon burning occurs via photodisintegration reactions at $T \sim 1.2 \times 10^9$ K:



This process mainly produces Mg and reinforces O production. It is typically confined to a shell.

O-burning

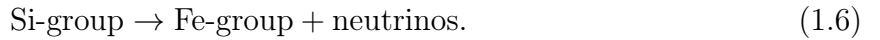
At $T \sim 1.5 \times 10^9$ K, oxygen nuclei fuse to form Si-group elements:



These products mark the onset of the “alpha-rich” freeze-out zone.

Si-burning

Silicon burning initiates at $T \gtrsim 2.7 \times 10^9$ K, leading to nuclear statistical equilibrium (NSE) dominated by iron-peak elements:



This final hydrostatic phase proceeds through a series of photo-disintegration and rearrangement reactions that populate nuclei such as ^{54}Fe , ^{56}Ni , and ^{58}Ni .

1.2.2 Neutron Capture Processes

***s*-Process**

The slow neutron capture process occurs during He- and C-shell burning via reactions such as:



In $12 - 20\text{M}_\odot$ stars, the weak s-process dominates, producing elements up to Sr-Y-Zr region.

i-Process

The intermediate neutron capture process occurs at neutron densities $n_n \sim 10^{13}\text{--}10^{15} \text{ cm}^{-3}$, between those typical of the s- and r-processes. It may be triggered in convective-reactive environments, e.g., O-C shell mergers, where hydrogen ingestion drives neutron bursts.

r-Process

The rapid neutron capture process requires extreme conditions ($n_n \gtrsim 10^{20} \text{ cm}^{-3}$) and short timescales. While unlikely in $12\text{--}20 M_\odot$ stars, it is included for completeness and is typically associated with neutron star mergers or magneto-rotational CCSNe.

1.2.3 *p*-Nuclei Nucleosynthesis

The classical p-nuclei are proton-rich isotopes not formed via s- or r-processes. In massive stars, these nuclei are produced via photodisintegration reactions:

rp-Process

Occurs in proton-rich, explosive environments (e.g., X-ray bursts), where rapid proton captures compete with β^+ decays.

νp-Process

Occurs in the neutrino-driven wind of core-collapse supernovae. Antineutrino absorption on protons produces neutrons that allow for bypassing rp-waiting points:

$$\bar{\nu}_e + p \rightarrow n + e^+. \quad (1.8)$$

γ -process

The main process responsible for p-nucleus production in massive stars. Involves successive photodisintegration reactions:

$$(\gamma, n), (\gamma, p), (\gamma, \alpha). \quad (1.9)$$

Pre-Explosive γ -process

Occurs during late hydrostatic O/Ne-shell burning in stars with $M \gtrsim 12 M_\odot$, at $T \sim 2\text{--}3 \times 10^9 \text{ K}$.

Explosive γ -process

Triggered during the passage of the supernova shock through the O-Ne layers, reaching $T \sim 3\text{--}4 \times 10^9 \text{ K}$.

1.2.4 Convective-Reactive Nucleosynthesis

Convective-reactive nucleosynthesis refers to processes where nuclear burning and convective mixing operate on comparable timescales. This often occurs in unstable mixing regions, such as O-C shell mergers, where hydrogen is ingested into He-, C-, or O-rich layers.

This regime is characterized by the Dämkohler number:

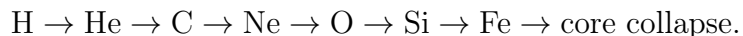
$$D_\alpha = \frac{\tau_{\text{transport}}}{\tau_{\text{reaction}}}. \quad (1.10)$$

- $D_\alpha \gg 1$: burning is slow; mixing dominates \Rightarrow homogenization.
- $D_\alpha \ll 1$: burning is fast; negligible mixing \Rightarrow localized nucleosynthesis.
- $D_\alpha \sim 1$: feedback between burning and transport \Rightarrow fully coupled convective-reactive regime.

Such conditions may trigger neutron bursts and exotic nucleosynthesis pathways (e.g., i-process), potentially contributing to chemical anomalies in metal-poor stars and globular clusters.

1.3 Massive Star Evolution

Stars with an initial mass $> 8M_\odot$ undergo the series of nuclear burning phases described above.



These burning phases lead to the structure of the star being separated convective shells with primary burning structures, as seen in Figure 1.1.

After the formation of the Fe-core and the star begins to rapidly contract as nuclear burning no longer can balance the gravitational force. This leads to a Type II supernova explosion where further shockwave induced nucleosynthesis can occur Prialnik (2009). The core of the star leaves behind a neutron star or black hole, and all other material is ejected into the interstellar medium. The exact location of where mass is ejected from changes the

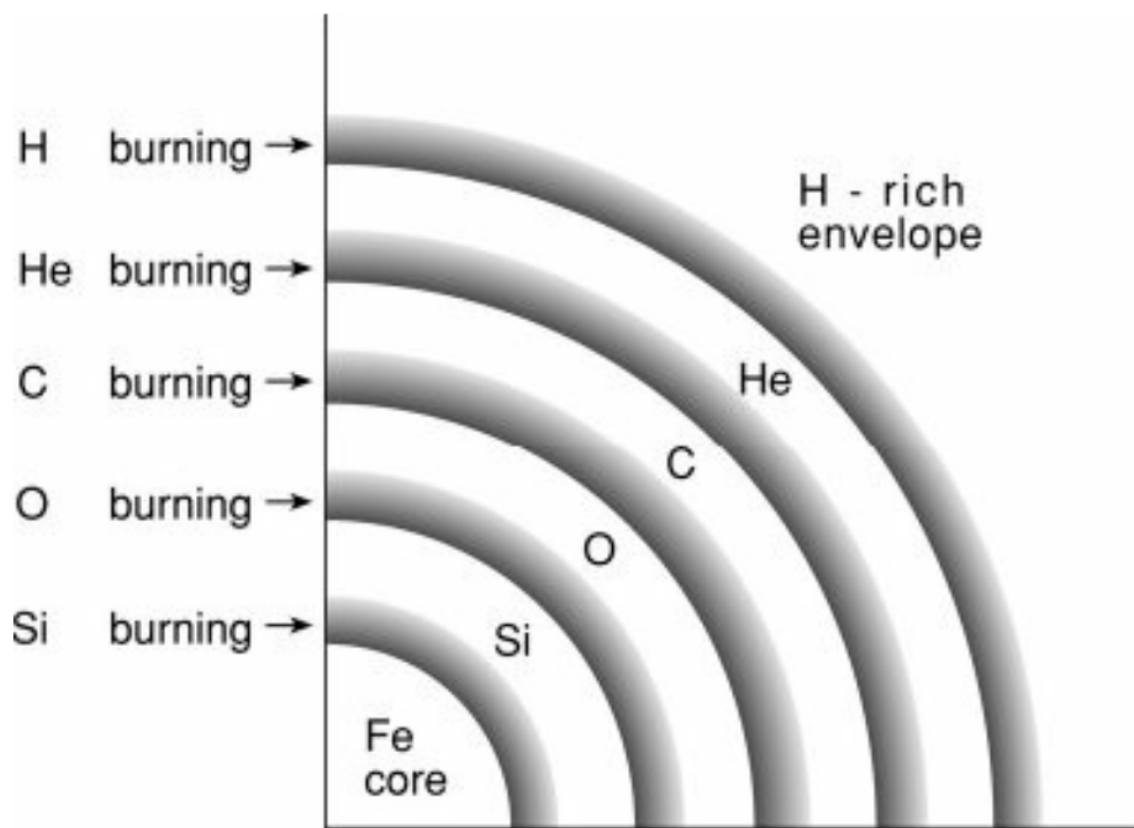


Figure 1.1: Taken from Prialnik (2009) Figure 9.19: Schematic structure of a supernova progenitor star.

yields of massive star nucleosynthesis as anything under it will remain in the star. Ritter et al. (2018b) place this mass cut for massive stars around the position of the Si/O-shell.

1.3.1 O-C Shell Mergers

In the final stages of advanced O-shell stellar burning, hours before the core collapse of the star, anywhere from 20% to 40% of 1-D massive star models have been found to have a merger of the O-, Ne-, and C-shells Rauscher et al. (2002); Ritter et al. (2018a); Collins et al. (2018); Roberti et al. (2023, 2025). This phenomenon is known as an O-C shell merger. Figure 1.2 shows a Kippenhahn diagram of the merger of the O- and C-burning shells for a $15M_{\odot}$, $Z = 0.02$ model from Ritter et al. (2018b).

These mergers occur when the convective O- and C-shells grow large enough to overlap, forming a single extended convective region. These mergers are known to have peculiar markers of nucleosynthesis because the convective-reactive environment of the O-shell, such as the production of the odd-Z elements P, Cl, K, and Sc which are underproduced in galactic chemical evolution calculations Ritter et al. (2018a); Roberti et al. (2025). In addition to these isotopes, the O-C shell merger has been a location for the production of the *p*-nuclei Rauscher et al. (2002); Ritter et al. (2018a); Roberti et al. (2023). As C-shell material containing stable *s*- and *r*-process seeds is ingested into the much hotter O-shell temperatures, they undergo γ -process. The O-C shell merger nucleosynthesis has been found to dominate this production independent of the peak energy of the supernova explosion Roberti et al. (2024).

O-C shell mergers have also been understood to be important for seeding asymmetries important for the supernova Müller (2016); Collins et al. (2018); Müller (2020); Yadav et al. (2020); Andrassy et al. (2020). The shell mergers are highly asymmetric and provide perturbations necessary for the supernova explosion in the O-shell Collins et al. (2018).

1.4 1-D Stellar Modelling

Stars are 3-D fluids that are governed by the Navier-Stokes equations where the fluid is undergoing a series of nuclear reactions. The hydrodynamical equations are given in Kippenhahn et al. (2013).

$$\frac{\partial \rho}{\partial t} + \nabla \cdot (\rho \mathbf{v}) = 0 \quad (1.11)$$

$$\rho \left(\frac{\partial \vec{v}}{\partial t} + (\vec{v} \cdot \nabla) \vec{v} \right) = -\nabla P - \rho \nabla \Phi \quad (1.12)$$

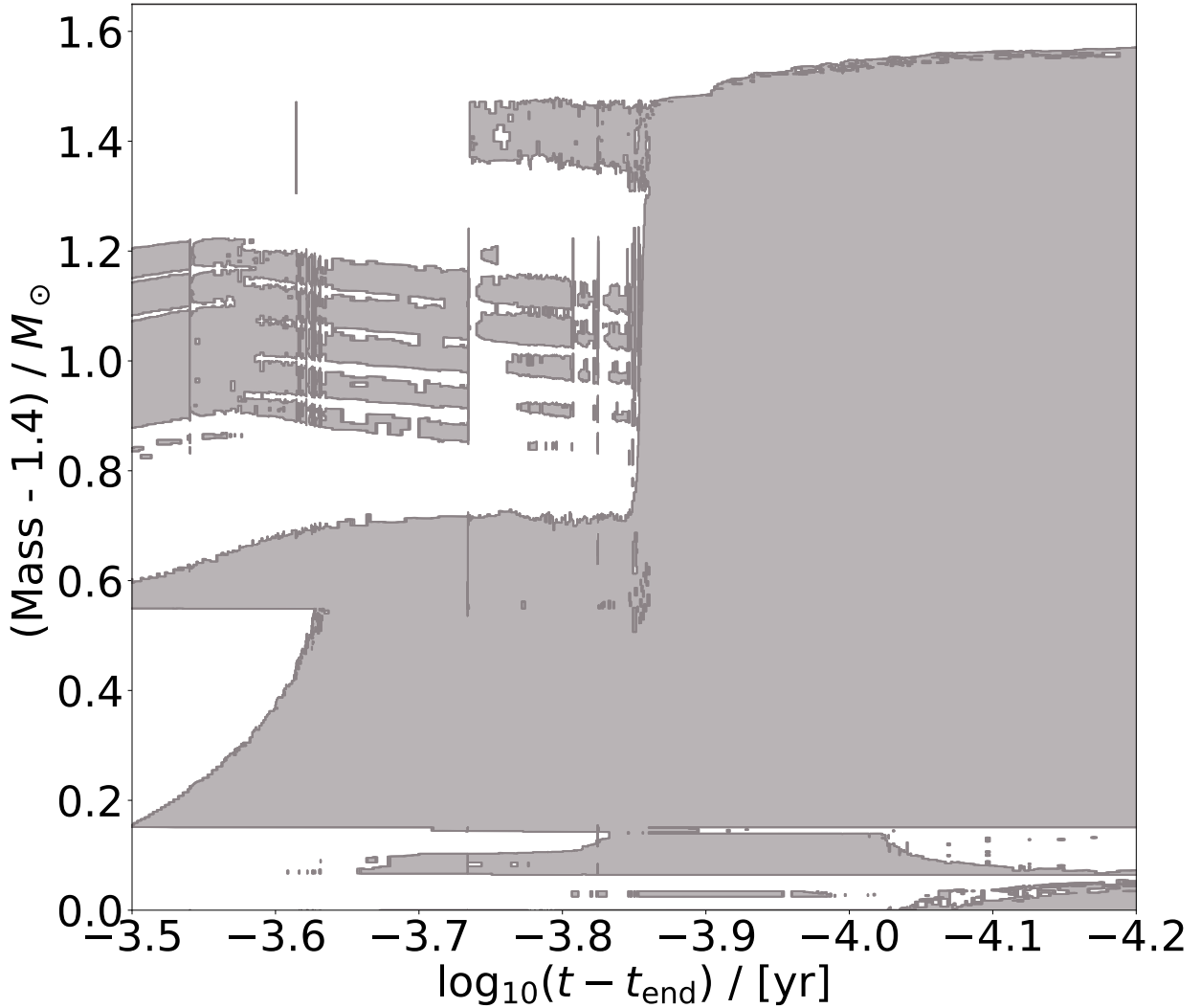


Figure 1.2: Kippenhahn diagram showing the merger of the convective O and C-burning shells for the $15M_{\odot}$ $Z = 0.02$ model from Ritter et al. (2018b). The O-burning shell extends from $1.55M_{\odot}$ to $1.95M_{\odot}$. The first convective C-burning shell sits directly on top from $1.96M_{\odot}$ to $2.11M_{\odot}$ and additional convective C-burning shells that are subsumed are above. The merger onsets at $\log_{10}(t - t_{\text{end}})/\text{yr} \approx -3.85$ and reaches full extent at ≈ -4 .

$$\frac{dE}{dt} = -\frac{P}{\rho} \nabla \cdot \vec{v} + \epsilon - \frac{1}{\rho} \nabla \cdot \vec{F} \quad (1.13)$$

$$\nabla^2 \Phi = 4\pi G \rho \quad (1.14)$$

where ρ is the density, \mathbf{v} is the velocity, P is the pressure, Φ is the gravitational potential, E is the specific internal energy, ϵ is the energy generation rate, and \vec{F} is the energy flux.

These equations are solvable in 3-D for simulations, to couple them with a nuclear network becomes too computationally expensive to solve. Some studies are able to calculate both the hydrodynamical and nuclear netowrk equations together Rizzuti et al. (2024b), but even involve limited nuclear networks. Additionally, 3-D simulations are prohibited by the computational cost of evolving a star through its entire evolution for the amount of time necessary. Because of this, it is necessary to have a 1-D approximation to be able to study the whole of stellar evolution.

1-D stellar modelling requires the assumption of spherical symmetry. Under this assumption, all variable become functions of the radial coordinate r and time t . However, it is typical in stellar evolution to consider a mass coordinate m rather than the radial coorinate r . This means that all of our stellar evolution variables can be written as a function of mass and time.

$$\rho = \rho(m, t) \quad P = P(m, t) \quad T = T(m, t) \quad L = L(m, t) \quad r = r(m, t)$$

We can derive each of these quantities relevant for stellar structure. First, radius is simplest as it can be determined by writing mass in terms of a spherical density $m = \frac{4}{3}\pi r^3 \rho$, differentiating, and rearranging.

$$\frac{\partial r}{\partial m} = \left(4\pi r^2 \rho(m, t) \right)^{-1} \quad (1.15)$$

Next, let us impose a fundamental assumption in 1-D stellar modelling: hydrostatic equilibrium. Under this assumption, the mass shells of the star are static so that the star does not grow or shrink in time because pressure and gravitational force are in equilbrium which would mean $\vec{v} = 0$. Taking both spherical symmetry and hydrostatic equilibrium, Equations 1.12 and 1.14 reduce to

$$\frac{\partial P}{\partial r} + \rho \frac{\partial \Phi}{\partial r} = 0$$

$$\frac{1}{r^2} \frac{d}{dr} \left(r^2 \frac{d\Phi}{dr} \right) = 4\pi G\rho$$

We can use the final equation here to get an explicit form of $\frac{\partial\Phi}{\partial r}$ by integrating and using the relationship between r and m to get that

$$\frac{\partial\Phi}{\partial r} = \frac{Gm}{r^2}$$

Using the form of $\frac{\partial\Phi}{\partial r}$ with Equation 1.15 we can rewrite the pressure equation to get

$$\frac{\partial P}{\partial m} = -\frac{Gm}{4\pi r^4} \quad (1.16)$$

Let's now consider how to get the luminosity in a similar form. Applying spherical symmetry, hydrostatic equilibrium, the relationship $L = 4\pi r^2 F$, and Equation 1.15 to Equation 1.13 we find with some rearranging that

$$\frac{dL}{dm} = \epsilon - \frac{dE}{dt}$$

ϵ in stars comes from nuclear reactions that generate energy and lose energy from neutrinos and so can be written as $\epsilon = \epsilon_{\text{nuc}} - \epsilon_\nu$. The energy E can be derived from thermodynamics and when fully written out the evolution of luminosity following Equation 10.3 in Kippenhahn et al. (2013) is

$$\frac{\partial L}{\partial m} = \epsilon_{\text{nuc}} - \epsilon_\nu - c_P \frac{\partial T}{\partial t} + \frac{\delta}{\rho} \frac{\partial P}{\partial t} \quad (1.17)$$

Consider now the temperature of the star. Let us assert that there is a generic temperature gradient to the star

$$\nabla \equiv \frac{T}{P} \frac{dP}{dT} = \frac{T}{P} \frac{\partial P}{\partial m} \cdot \frac{\partial m}{\partial T}$$

Using Equation 1.16, we can rearrange and find that

$$\frac{\partial T}{\partial m} = -\frac{GmT}{4\pi r^4 P} \nabla \quad (1.18)$$

The temperature gradient that we assert describes the transport of energy by either radiation or adiabatic movement of fluid elements and can be described by $\nabla = \nabla_{\text{rad}} + \nabla_{\text{ad}}$. The steeper the gradient, the more difficult it is for energy to be transported from r_1 to r_2 .

Let us consider the scenario where energy is being more efficiently transported by photons ($\nabla_{\text{rad}} < \nabla_{\text{ad}}$). We can derive an explicit form for the temperature gradient from first

principles following the derivation in Chapter 5 of Kippenhahn et al. (2013). First, suppose that we have photons travelling in a medium that have some mean free path that they travel before interacting. It is clear that the only interaction inside of the star would be with the plasma. The more dense the star is, the shorter the mean free path will be, hence

$$\ell_{\text{mfp}} = (\kappa\rho)^{-1}$$

where ρ is the density of the star at r and κ is the opacity which by dimensional analysis has units of $\text{cm}^2 \text{ g}^{-1}$.

Assuming that we are in local thermal equilibrium and that the mean free path is much smaller than the size of the star, we can assume that we are able to describe the motions of the photons by a diffusive process. Generically, in diffusive processes the flux can be described by

$$\mathbf{j} = -D \nabla n$$

where n is the particle density and $D = \frac{1}{3}v\ell$ is the diffusion coefficient where v is the mean velocity and ℓ is the mean free path of those particles.

Since we are describing photons and not particles, let us consider the energy density $U = aT^4$, where a is the radiation constant, rather than n and its flux F rather than \mathbf{j} . This also means that the velocity $v = c$ and that the mean free path $\ell = (\kappa\rho)^{-1}$. Putting these together we find that

$$F = -\frac{1}{3}\frac{c}{\kappa\rho} \nabla(aT^4) = -\frac{4ac}{3}\frac{T^3}{\kappa\rho} \frac{\partial T}{\partial r}$$

Knowing that the flux can be described by $F = 4\pi r^2 L$, we can rearrange our formula to find that the radiative temperature gradient is given by

$$\nabla_{\text{rad}} = \left. \frac{\partial T}{\partial r} \right|_{\text{rad}} = -\frac{3}{16\pi ac} \frac{\kappa\rho L}{r^2 T^3} \quad (1.19)$$

Let us now consider the scenario where energy is transported mostly efficiently by the adibatic motions of fluid elements ($\nabla_{\text{rad}} > \nabla_{\text{ad}}$). This would describe the scenario in a convective region where warmer fluid elements are rising to the top and cooler elements are sinking to the bottom. Assuming that the fluid in stars can be described by the ideal gas law, we can find that

$$P = \frac{\mathcal{R}}{\mu} \rho T \rightarrow \ln P = \ln \rho + \ln T + \ln \left(\frac{\mathcal{R}}{\mu} \right) \rightarrow \frac{d \ln P}{dr} = \frac{d \ln \rho}{dr} + \frac{d \ln T}{dr}$$

Assuming that the gas behaves adiabatically, following Chapter 19 of Kippenhahn et al. (2013) we know that

$$P \propto \rho^\gamma \rightarrow \frac{d \ln P}{dr} = \gamma \frac{d \ln \rho}{dr}$$

where γ is the polytopic index. We can insert the relationship for $d \ln \rho$ into the ideal gas law to find that

$$\frac{d \ln P}{d \ln r} = \frac{1}{\gamma} \frac{d \ln P}{d \ln r} + \frac{d \ln T}{dr} \rightarrow \frac{d \ln T}{dr} = \left(1 - \frac{1}{\gamma}\right) \frac{d \ln P}{d \ln r}$$

The generic form $\frac{d \ln A}{dx} = \frac{1}{A} \frac{dA}{dx}$ and so we can rewrite this as

$$\nabla_{\text{ad}} = \frac{\partial T}{\partial r} \Big|_{\text{ad}} = \left(1 - \frac{1}{\gamma}\right) \frac{T}{P} \frac{dP}{dr} \quad (1.20)$$

In the radiative transport case, the only quantity that evolves is the temperature as photons are moving around, but in the adiabatic transport case fluid elements that have their own unique chemical composition μ in addition to their own temperature are moving around. Therefore, in the radiative case only the temperature is equilibrated, but in the adiabatic case temperature and chemical composition are equilibrated. Additionally, for the motions of a fluid to be adiabatic, it is assumed that it has a constant entropy gradient. If a region was radiative but slowly becomes adiabatic, it must be the case that the entropy gradient also equilibrates as the region forms.

Stellar modelling is also concerned with the evolution of the chemical composition of the star. The chemical composition in a star can be described by both the nuclear reactions that occur to change the composition and the motions to mix the composition. The following follows the lecture content of Herwig (2023) and description by Langer et al. (1985).

The mass fraction of an individual isotope is given as X_i where the sum of all isotopes $\sum_i X_i = 1$, and is related to the mole fraction $Y = X/A$ where A is the atomic mass of the isotope. The energy generation of a star comes from the nuclear reactions that occur in the star and can be described by

$$\frac{d\mathbf{X}_j}{dt} \Big|_{\text{burn}} = \hat{F}_j \cdot \mathbf{X}_j \quad (1.21)$$

where \mathbf{X}_j is the vector of mass fractions at some position j and \hat{F}_j are the nuclear reactions that the isotopes undergo. These reactions are typically written in number density as opposed to mass fraction which is given by $N_i = Y_i \rho N_A$ where N_A is the Avogadro number and

$Y_i = X_i/A_i$ is the mole fraction and A_i is the mass number.

$$\frac{dN_i}{dt} = N_l N_k \langle \sigma v \rangle_{lk} - N_i N_j \langle \sigma v \rangle_{ij} + \dots + N_n \lambda_n - N_p \lambda_p \quad (1.22)$$

where $\langle \sigma v \rangle_{ij}$ is the average of the product of the cross section and relative velocities in the centre of mass frame and λ is rate of β decays.

The mixing of isotopes in the star is described by the diffusion equation:

$$\left. \frac{dX_i}{dt} \right|_{\text{mix}} = \frac{\partial}{\partial m} \left[(4\pi r^2 \rho)^2 D \frac{dX_i}{dm} \right] \quad (1.23)$$

where X_i is the mass fraction of a particular isotope.

1.4.1 Mixing Length Theory Approximation

Prandtl (1925) was first to describe the turbulent flow of water through a channel by considering a characteristic length scale the eddies would travel before mixing with their surroundings. Following his insight, Böhm-Vitense (1958) developed the first stellar model using the idea of a characteristic length scale to describe the convective motions of the Sun.

Turbulent motions are complex 3-D flows involving eddies of different shapes, velocities, and distances they travel before mixing with their environment. Rather than describing the flow of every individual fluid element, instead consider that on average, each fluid element travels a distance ℓ before mixing with its surroundings. In addition to this, assume that the average size of the fluid elements is equal to this travel distance ℓ . This is the mixing length theory (MLT) approximation. In addition to ℓ , these balls of fluid also have other average properties such as their velocity \bar{v} and therefore an average timescale they travel for before mixing with their surroundings $\tau = \ell/\bar{v}$ (Kippenhahn et al., 2013; Cox and Giuli, 1968; Joyce and Tayar, 2023). In stars, the mixing length is given by:

$$\ell_{\text{MLT}} = \alpha_{\text{MLT}} H_P, \quad (1.24)$$

where H_P is the pressure scale height and α_{MLT} is a dimensionless free parameter and can be chosen to match stellar evolution tracks to empirical data (Joyce and Tayar, 2023).

Prandtl (1925) used this assumption to describe the turbulent flows by a diffusion process, and this description of the motion is still the understood physical picture that MLT relies on (Joyce and Tayar, 2023). In the MLT approximation, the motion of fluid elements is

characterized by a diffusion coefficient:

$$D_{\text{MLT}} = \frac{1}{3} v_{\text{conv}} \ell_{\text{MLT}} \quad (1.25)$$

where v_{conv} are the average convective velocities of the fluid elements and ℓ_{MLT} is the mixing length. The timescale can also be re-written in terms of this diffusion coefficient and the mixing length (Herwig et al., 2011).

$$\tau_{\text{MLT}} = \ell_{\text{MLT}}^2 / D_{\text{MLT}} \quad (1.26)$$

1.4.2 Stellar Evolution with MESA

The **M**odules for **E**xperiments in **S**tellar **A**strophysics (**MESA**) code is an open-source 1-D stellar evolution framework used in stellar astrophysics that allows the computation of the structure and evolution of stars from pre-main-sequence to advanced stages of burning up to core-collapse (Paxton et al., 2010). One of **MESA**'s distinguishing features is its implicit, fully coupled solution of the structure, nuclear burning, and mixing equations. The code employs a Newton-Raphson method to simultaneously solve the coupled set of equations of 1-D stellar structure, diffusion of species, and nuclear reactions. The coupled equations allow **MESA** to resolve multi-timescale problems. In convective regions, **MESA** adopts a time-dependent diffusive mixing approximation, solving the mixing and burning processes within the same timestep using operator coupling:

$$\left(\frac{dX_i}{dt} \right)_{\text{total}} = \left(\frac{dX_i}{dt} \right)_{\text{nuc}} + \left(\frac{dX_i}{dt} \right)_{\text{mix}}, \quad (1.27)$$

where X_i is the mass fraction of isotope i , and both terms are evaluated and advanced implicitly in a coupled fashion. Species mixing in **MESA** is taken to be diffusion Paxton et al. (2010). **MESA** can include nuclear networks of hundreds of isotopes. However, solving large coupled equations takes a lot of computational power, and so stellar evolution calculations typically use reduced networks to capture the reactions that are relevant to energy generation without tracking full nucleosynthetic yields.

1.4.3 Post-Processing with mppnp

To obtain detailed nucleosynthesis predictions, post-processing stellar models is needed. One such code is **multi-zone post-processing network parallel** (**mppnp**) created by

the NuGrid collaboration². `mppnp` is a parallelized multi-zone code that takes in already evolved stellar structure and species from `MESA` and calculates the full nucleosynthesis of thousands of isotopes and tens of thousands of reactions.

Unlike the coupled equations of `MESA`, `mppnp` adopts an operator-split approach where it solves nuclear reactions and mixing separately in alternating steps.

1. The abundances X_i are updated via an implicit solver for nuclear reactions, using the supplied temperature and density histories.
2. The resulting abundances are then mixed by diffusion.
3. Optionally, an ingestion step can be included where a species is ingested at the top of region and mixed in.

By decoupling the nuclear physics from the stellar structure, `mppnp` is able to calculate large nuclear networks, but it also poses a problem for convective-reactive nucleosynthesis. In regular convective burning, the $D_\alpha \ll 1$ as the timescale for mixing is much faster than nuclear burning (and vice versa for radiative burning), but in convective-reactive environments $D_\alpha = 1$. Because these timescales are near equal, the evolution of the mass fraction is coupled to both operators. Therefore, it is important when calculating the results of a convective-reactive environment, that all timescales are resolved enough so that there is little change in the final result.

As shown in Figure 1.3, there is a noticeable change in the final mass fraction of the isotopic abundances. While these lighter isotopes ^{12}C , ^{16}O , and ^{20}Ne are not drastically changed, the final production of heavier isotopes such as the p -nuclei can be orders of magnitude.

In addition to the importance for timescale resolution, there is also spatial resolution. Changing the number of mass zones in the simulation can change the final result as the mixing of the isotopes depends on the number of fluid elements that can be resolved. By ensuring that the number of mass zones is high enough, the mixing can be resolved to a point where the final result is not changed by the number of mass zones.

1.5 3-D Macrophysics

Despite the value of 1-D stellar evolution codes, stars are 3-D objects that exhibit non-spherical features. The simplifications made by spherical symmetry and the MLT approximation do not sufficiently capture the 3-D physics of convection. Because of this, there are modelling inconsistencies between 1-D MLT predictions and 3-D hydrodynamic simulations.

²Details about the NuGrid collaboration and its code can be found at <https://nugrid.github.io/>.

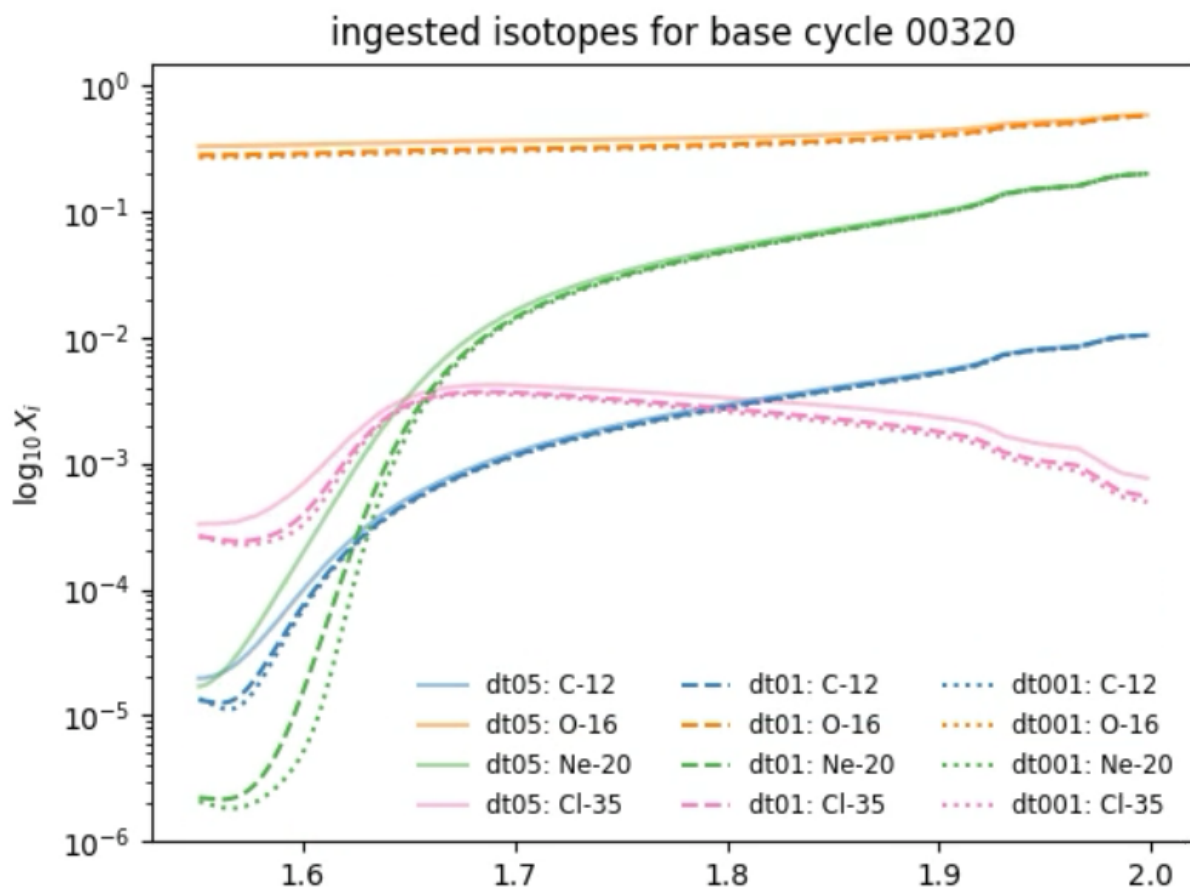


Figure 1.3: Evolution of the mass fraction of ^{12}C , ^{16}O , ^{20}Ne , and ^{35}Cl in a convective-reactive environment at the same simulation time with different timesteps. The solid line corresponds to a simulation with timestep of $\Delta t = 0.5\text{s}$, the dashed line corresponds to $\Delta t = 0.1\text{s}$, and the dotted line corresponds to $\Delta t = 0.01\text{s}$.

1.5.1 Insufficiencies of MLT

As explained before, MLT assumes that there is some average length ℓ_{MLT} that all fluid elements travel in a convective environment before mixing with their surroundings.

One of the problems with MLT is how it treats the boundaries of a convective region where we find $\nabla_{\text{ad}} = \nabla_{\text{rad}}$. According to Equation 1.25, the diffusive coefficient for mixing is equal to the convective velocities. Outside the boundary of a convective region, suddenly $v_{\text{conv}} = 0$ which would imply an unphysical infinite acceleration to stop the fluid at the edges. To more accurately treat the boundaries, stellar evolution codes like MESA implement a convective overshooting parameterization where

$$D_{\text{OV}} = D_{\text{conv},0} \times \exp\left(-\frac{2z}{f\lambda_{P,0}}\right) \quad (1.28)$$

where $D_{\text{conv},0}$ is the diffusion coefficient at the boundary, $\lambda_{P,0}$ is the pressure scale height at that location, z is the position in the radiative zone, and f is a free parameter so that the diffusion drops off exponentially rather than immediately Paxton et al. (2010).

As described in Renzini (1987), there are some fundamental issues in using MLT to describe a convective region. One big issue is that the mixing length is assumed to be both the average distance a fluid element travels and its size. If the convective region you want to describe is smaller than the mixing length, then you will be unable to resolve the mixing, as it is smaller than a single fluid element. This applies to both convective regions and the overshooting region, which is a fraction of the pressure scale height. Therefore, for MLT to be a valid description, you must have a sufficiently small ℓ_{MLT} .

As recognized by Bazan and Arnett (1994), the O-burning shell cannot adequately be described by MLT. For example, Figure 1.4 shows the $15M_{\odot}$, $Z = 0.02$ model from Ritter et al. (2018b) as it is merging. The O-burning shell has a size of 4.7 Mm, merging region 1.07 Mm, and C-burning shell 9.44 Mm. At best, the regions can resolve 3.2, 0.3, and 2.2 fluid elements respectively. Clearly, these regions are not well resolved by MLT – especially the merger region. INSERT THIS PARAGRAPH HERE

1.5.2 3-D Simulations of Convective O-Shell Burning and C-Shell Entrainment

Multidimensional hydrodynamic simulations have been done of O-shell burning and C-shell entrainment in massive stars. Bazan and Arnett (1994) performed a 2-D simulation of O-burning where they show that the convective motions and temperature are non-radially, spherically asymmetric and mix through radiative layers by a penetrative convection rather

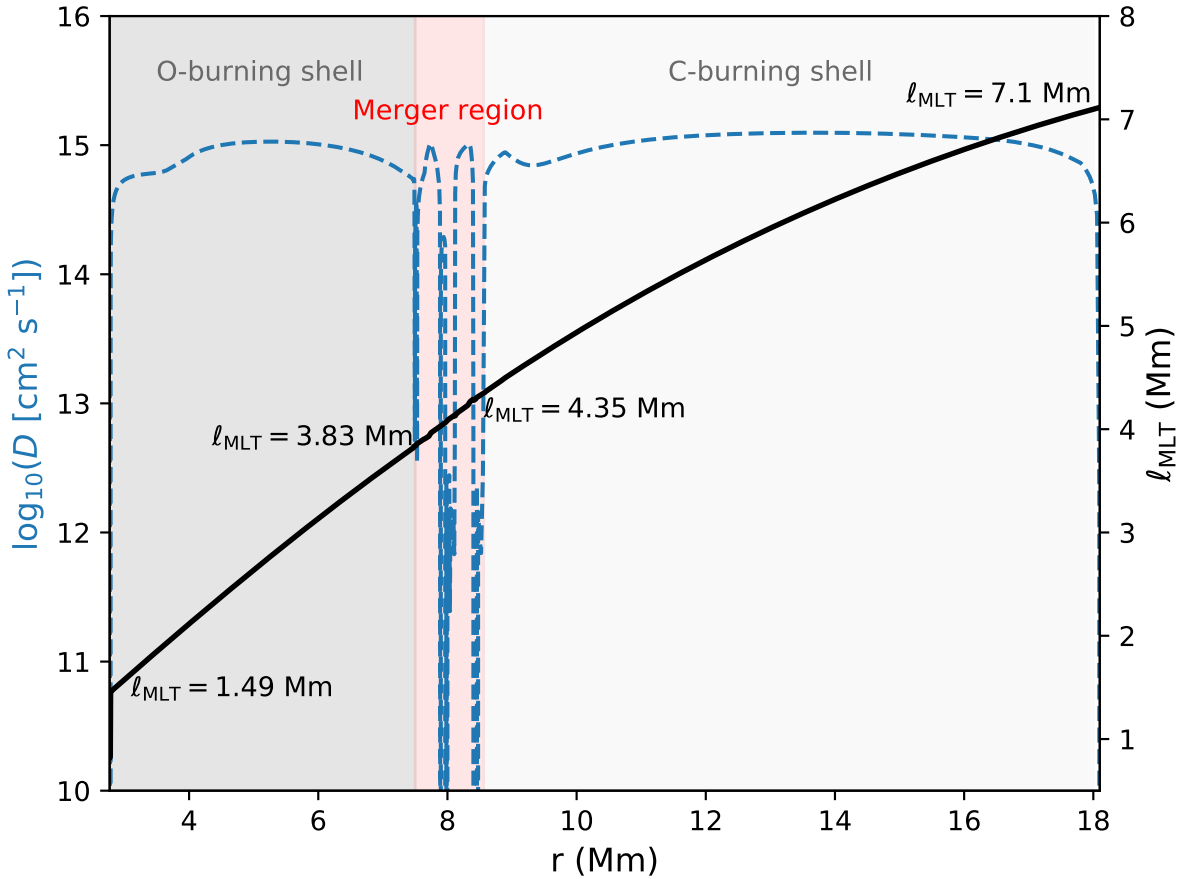


Figure 1.4: O-burning shell of the $15M_{\odot}$ $Z = 0.02$ model from Ritter et al. (2018b) at model number 9200 right before the merger with C-shell is fully realized. The O-shell is from 2.79 Mm to 7.49 Mm , the merger region is from 7.49 Mm to 8.56 Mm , and the C-burning shell is from 8.56 Mm to 18 Mm .

than a simple overshoot.

Meakin and Arnett (2006) performed a 2-D simulation of both the O- and C-burning shells with a limited nuclear network and compared to a 3-D simulation of just the O-shell. They found that the non-convective region between the two shells had comparable velocities to the convective shells and that the convective shells have large, round vortices and asymmetric density perturbations. Additionally, they found that the convective motions excited waves in the radiative layer that allowed for C-shell entrainment into the O-shell at $\sim 10^{-4} M_{\odot} s^{-1}$. Because of this entrainment, they found there would be sudden O-flames burning in the O-shell that would turn on and off. However, they note that their 3-D O-shell simulation show plumes rather than vortices to describe the flow and caution against using 2-D simulations to describe the convective motions in this scenario.

Meakin and Arnett (2007) also find this mixing difference between 2 and 3-D simulation of O-shells, and they also find that the 3-D radial velocity decreases gradually at the top of the shell and sharply at the bottom, which cannot be explained by a constant α_{MLT} . This is explained by the distance to the convective boundary acting as an upper limit to the mixing length, as fluid elements cannot travel a full mixing length if the remaining space they have is less than it. They also find turbulent entrainment of material from the stable layer above the O-shell.

Jones et al. (2017) in their 3-D simulation of O-shell burning that the 3-D radial velocity profile exhibits the same gradual decrease at the upper boundary and find an entrainment from the stable layer of $1.33 \times 10^{-6} M_{\odot} s^{-1}$. As they show in Figure 1.5, the diffusion coefficient from MLT does not match the shape of what is estimated in 3-D as well underestimating the velocities. However, they provide a recommendation for 1-D modelling to better match the 3-D diffusion profile shape:

$$D_{RCMD} = v_{MLT} \times \min(\alpha H_P, |r - r_{SC}|) \quad (1.29)$$

where $\alpha H_P = \ell$ is the mixing length, r is the radius in the convective region, and r_{SC} is the distance to the convective boundary. This is rooted in the same insight by Meakin and Arnett (2007) that fluid elements may be too close to the convective boundary to move a full mixing length. In addition to this, they apply the same insight of distance to convective boundary to convective overshooting and find good agreement with the spherically average 3-D D .

Arnett et al. (2019) – I honestly don't understand this one yet

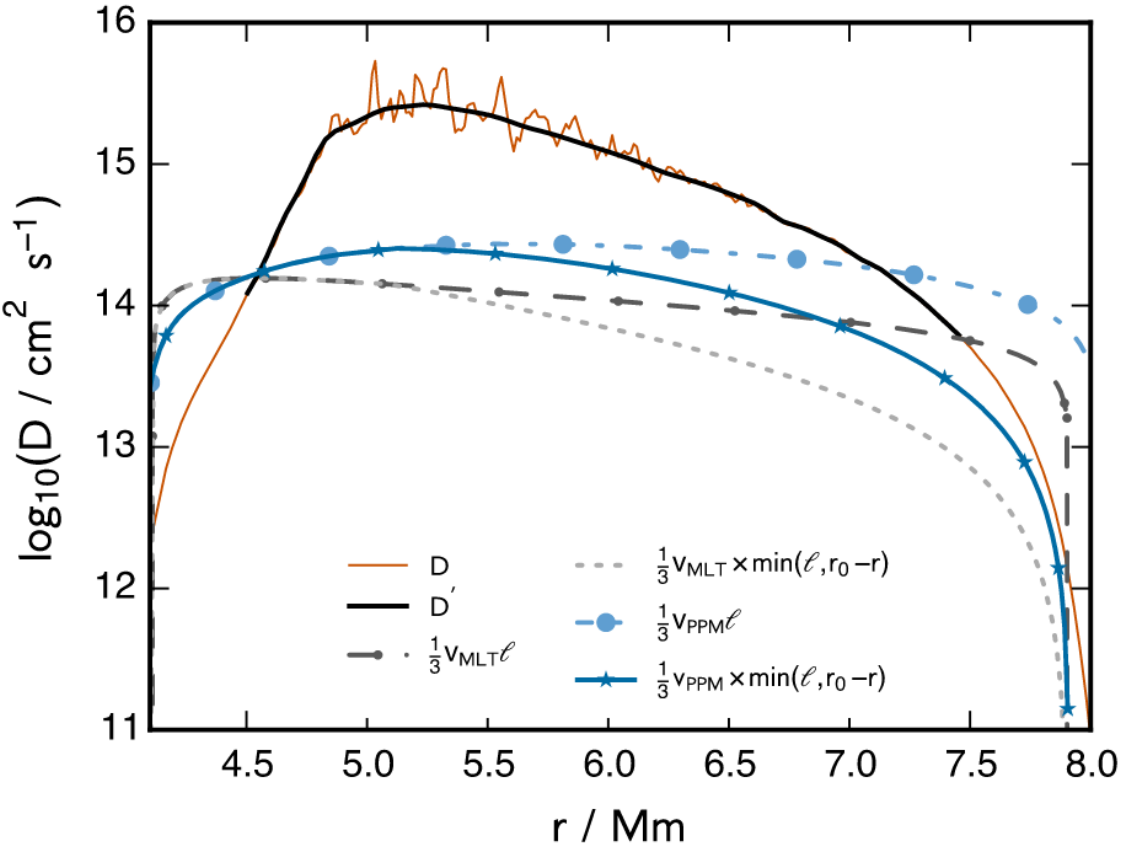


Figure 1.5: Taken from Jones et al. (2017): Time-averaged radial diffusion coefficient profile calculated from the spherically averaged abundance profiles by the method described in Section 3.5 (brown solid line; black solid line is a fit to the noisy region). The convective velocities computing using MLT agree with the spherically averaged 3D velocities to within about a factor of 2 inside the convection zone but are too large in the vicinity of the CB, resulting in an overestimation of the diffusion coefficient there. Limiting the mixing length to the distance from the CB reproduces the fall-off of the diffusion coefficient inside the convection zone approaching the boundary which is seen in the spherically averaged 3D simulation results.

Yadav et al. (2020) in their 3-D simulation of an O-Ne shell merger where they find 3-D has much faster convective velocities than predicted in 1-D, and as the Ne-shell merges strong plumes carry the material to the bottom of the O-shell where burn in a convective-reactive environment. The asymmetric plume distribution leads to local hotspots of burning causing as difference in the Si, O, and Ne mass fractions when compared to 1-D.

Andrassy et al. (2020) performed 3-D simulation of C-ingestion into a convective O-shell and found a range of possible ingestion rates from $9.5 \times 10^{-8} M_{\odot} s^{-1}$ to $1.18 \times 10^{-8} M_{\odot} s^{-4}$ and v_{rms} from 38 km s^{-1} to 181 km s^{-1} depending on the luminosity of $^{12}\text{C} + ^{12}\text{C}$, $^{16}\text{O} + ^{16}\text{O}$, and $^{12}\text{C} + ^{16}\text{O}$. In their simulations they find large scale asymmetries in the luminosity and density during entrainment. The radial velocity profile they find exhibits a gradual decline at the top of the O-shell, but also a less steep decline at the bottom of the shell. In addition to this, they boost the energy of C-burning and find large scale asymmetric oscillations like the Global Oscillation of Shell H-ingestion (GOSH) as found in Herwig et al. (2014). GOSHs can lead to increased entrainment of material, but also quench convective motions.

Rizzuti et al. (2024a) performed a 3-D hydrodynamic simulation of an O-C shell merger with a limited nuclear network and find significant differences from their 1-D model. In the 1-D model, the top convective boundary of the O-shell grows until it merges with the Ne/C-shell above it, but in the 3-D simulation the bottom of the C-shell grows until it merges with the Ne and O-shells under it. Like Jones et al. (2017), they find that 1-D convective velocities are a few factors lower than the 3-D simulation. Because of the differences in 1-D and 3-D they find that there are significant differences in the mass fraction of species like ^{20}Ne , ^{24}Mg , and ^{28}Si .

1.5.3 1-D Implementation of 3-D Hydrodynamics

Despite the insufficiencies of 1-D stellar evolution, 3-D hydrodynamic codes are unable to calculate the nucleosynthesis for complex processes such as the γ -process where thousands of isotopes can be involved. Nucleosynthetic yields have to be calculated then in 1-D, but the insufficiencies of 1-D can be mitigated by adopting the results of 3-D hydrodynamics and testing a variety of mixing scenarios. Specific to O-shell burning in O-C shell mergers, the following are possible to investigate in 1-D to explore the impact on nucleosynthesis.

- The shape of the radially averaged 3-D diffusion coefficient profile exhibits a downturn at the boundaries of the O-shell that is not seen in 1-D (Meakin and Arnett, 2007; Jones et al., 2017).

- Convective velocities are higher in 3-D hydrodynamic simulations than predicted by mixing length theory (Jones et al., 2017; Rizzuti et al., 2024a).
- The entrainment rate of C-shell material into the O-shell could be anywhere from $10^{-8} M_{\odot} s^{-1}$ to $10^{-4} M_{\odot} s^{-1}$ (Andrassy et al., 2020).
- Asymmetric non-radial instabilities are present due to energy feedback which could lead to convective quenching (Andrassy et al., 2020).

To address the shape a gradual downturn to D_{conv} Equation 1.25 from Jones et al. (2017) is adopted, but at the bottom of the O-shell instead of the top. This is done because we are simulating the nucleosynthesis during an O-C shell merger, and so the upper convective boundary is already connected to the C-shell above. To address lower convective velocities in 1-D, a series of boost factors can be applied to D . To address the variability of C-shell entrainment, a variety of entrainment rates can be adopted in a 1-D post-processed model. Finally, to address energy feedback such as the GOSH-like events seen in Andrassy et al. (2020), a simple dip in the convective profile can be adopted:

$$D_{\text{dip}} = D_{\text{MLT}} - (D_{\text{MLT}} - c) \times \exp \left[-\frac{(r - a)^2}{w^2} \right] \quad (1.30)$$

where c is the depth of the dip, a is the location of the dip, and w is width of the dip. Using the results of 3-D hydrodynamic simulations, we can explore the possible impact on nucleosynthesis from macrophysics.

1.6 Thesis Outline

Chapter 2: Impact of 3D-macrophysics and nuclear physics on p-nuclei nucleosynthesis in O-C shell mergers

In Chapter 2, I describe the impact of a 1-D implementation of 3-D hydrodynamic concerns on the production of the p-nuclei. I explore how the nature of convective-reactive nucleosynthesis for the p-nuclei, how the mixing concerns mentioned in Section 1.5.3. In addition to this, I present the results of a nuclear reaction correlation study and investigate how the mixing concerns change the correlation results. I also provide a discussion where I explain the potential impacts and limitations of this work.

Chapter 3: Additional Work

In Chapter 3, I describe how this work can continue to be applied to the production of the light odd-Z isotopes. In particular, I highlight how the isotopes ^{39}K , ^{40}K , and ^{41}K are impacted by these mixing concerns as it may have relevance to the formation of exoplanets and whether it would have an atmosphere capable of Earth-like life. I also provide some preliminary work done investigating whether advective-reactive nucleosynthesis matters for the *r*-process in the post-processing of trajectories that have escaped a black hole.

Chapter 2

Impact of 3D-macrophysics and nuclear physics on p-nuclei nucleosynthesis in O–C shell mergers

The following work has been written and prepared for submission to peer-review. Small changes have been made to fit the thesis format, but the content remains unchanged. All work was done in collaboration with my supervisor Dr. Falk Herwig and from Dr. Pavel Denissenkov. Dr. Denissenkov supplied the initial code used to create the post-processed models, analysis tools, and training necessary to understand how to use the code. I have modified this code and created new tools to perform the analysis, but his contributions were essential to the initial stages. Dr. Herwig has provided guidance and support throughout the project in his role as my supervisor.

2.1 Introduction

The question of how to replicate the solar pattern of the 35 stable “p-nuclei”¹ has been a long-standing problem in nucleosynthesis. It was originally considered that these isotopes had no contribution from the *s*- and *r*-processes, and it was proposed by Burbidge et al. (1957) that they were created via (p, γ) , (n, γ) , and (γ, n) reactions in Type II supernovae (SNe) in a process called the *p*-process. A variety of processes and astrophysical sites have been discussed as a site for the production of the p-nuclei, but there is not a single site for the production of them all. Woosley and Hoffman (1992) found that the α -rich freezeout in supernova can produce ^{74}Se – ^{92}Mo . Fröhlich et al. (2006) and Arcones and Montes (2011) both found that high neutrino fluxes during a supernova can create a proton rich environment in a process called the νp -process that produce ^{74}Se – ^{108}Cd . Schatz et al. (1998) suggest that

¹They are ^{74}Se , ^{78}Kr , ^{84}Sr , ^{92}Mo , ^{94}Mo , ^{96}Ru , ^{98}Ru , ^{102}Pd , ^{106}Cd , ^{108}Cd , ^{113}In , ^{112}Sn , ^{113}Sn , ^{115}Sn , ^{120}Te , ^{124}Xe , ^{126}Xe , ^{130}Ba , ^{132}Ba , ^{138}La , ^{136}Ce , ^{138}Ce , ^{144}Sm , ^{152}Gd , ^{156}Dy , ^{158}Dy , ^{162}Er , ^{164}Er , ^{168}Yb , ^{174}Hf , $^{180\text{m}}\text{Ta}$, ^{180}W , ^{184}Os , ^{190}Pt , ^{196}Hg

a hydrogen-rich accretion disk around a neutron star could undergo a series of rapid proton captures called the *rp*-process that produce ^{74}Se – ^{98}Ru . Xiong et al. (2024) propose that neutrino induced reactions of *r*-process material in a νr -process could produce the p-nuclei from ^{78}Kr – ^{138}La and argue that these conditions could be met in the winds of a proto-neutron star. Goriely et al. (2002) propose that a proton-poor but neutron boosted region could undergo proton-captures similar to the *rp*-process but can extend to the heavier p-nuclei as well as the light in a process called the *pn*-process during He-detonation of a C-O white dwarf’s ejected envelope. Travaglio et al. (2011) found that they could produce p-nuclei via the photo-disintegration of *s*-process material via the γ -process in SNIa could produce the not only the p-nuclei, but also the notoriously underproduced isotopes $^{92,94}\text{Mo}$ and $^{96,98}\text{Ru}$. In a follow-up paper, Travaglio et al. (2015) found that the *s*-process distribution of seed material for the γ -process was very significant on the production of p-nuclei in this scenario, especially the heaviest ones, and that there is a heavy metallicity dependency on the lightest three p-nuclei. Battino et al. (2020) found that rapidly accreting white dwarfs that have H-flashes achieve neutron densities necessary for the *i*-process that modify the seed distribution so that it could produce the p-nuclei in the range $96 < A < 196$ during the subsequent SNIa. In massive stars, Pignatari et al. (2016a) argue that the weak *s*-process can modify the seeds before the CCSN to boost production of the p-nuclei via the γ -process during the explosion.

There is contention whether all of the classical 35 isotopes are “p-nuclei”. Bisterzo et al. (2011) found that ^{152}Gd , ^{164}Er , and ^{180}Ta have 70.5%, 75.5%, and 74.5% respectively have *s*-process contribution. Dillmann et al. (2008) argues that ^{113}In and ^{115}Sn are made in β -decays post *r*-process via isomeric states. Goriely et al. (2001) found that (γ, n) was too weak to produce ^{138}La , and instead that it is made by ν_e -capture on ^{138}Ba during the explosion of a $M_{\text{ZAMS}} = 25M_\odot$ star. Arnould and Goriely (2003) say that it is possible that ^{180m}Ta could have contributions from ν -induced nucleosynthesis similar to ^{138}La . Sieverding et al. (2018) also found that the ν -process is important for ^{113}In , ^{138}La , and ^{180}Ta .

In this paper, we will be focused on how the γ -process in massive stars pre-supernova produce the p-nuclei. The γ -process describes the flow of (γ, n) , (γ, p) , and (γ, α) reactions on the stable *s*-, *i*-, and *r*-process seeds that are already present Rauscher et al. (2013). Arnould (1976) argue that hydrostatic O-burning at temperatures of 2 GK could be a site for the production of p-nuclei, and Woosley and Howard (1978) continued to describe the production of p-nuclei by photo-disintegrating the heavy elements at temperatures of 2 – 3 GK during explosive carbon and oxygen burning. Rauscher et al. (2002) found in their $M_{\text{ZAMS}} = 20M_\odot$ massive star model had pre-explosive production of the p-nuclei during a merger

of the convective oxygen, carbon, neon shells right shortly before the model underwent a core collapse supernova (CCSN). Rauscher et al. (2013) say that the effective temperature range for producing the p-nuclei by the γ -process and the νp -process is $1.5 \leq T \leq 3$ GK. Although the γ -process can produce across the mass range, there are known problems with this process. Woosley and Heger (2007) found that the γ -process in the supernova of massive stars was deficient for those between $A = 90 - 130$ and Arnould and Goriely (2003) note that particularly $^{92,94}\text{Mo}$ and $^{96,98}\text{Ru}$ are underproduced by the γ -process in CCSN. Further, Rayet et al. (1990) and Dillmann et al. (2008) argue that ^{113}In , ^{115}Sn , ^{152}Gd , ^{164}Er and ^{180m}Ta are weakly produced or even destroyed during the γ -process and should not even be considered as p-nuclei.

Roberti et al. (2023) looked at two massive star models with O-C shell mergers and found that most of the p-nuclei with $A > 110$ were dominantly produced during the merger and not from explosive CCSN nucleosynthesis. These stellar models were the $M_{\text{ZAMS}} = 15M_{\odot}$, $Z = 0.02$ from Ritter et al. (2018b) and $M_{\text{ZAMS}} = 20M_{\odot}$, $Z = 0.02$ model from Rauscher et al. (2002). Roberti et al. (2024) found this result to be independent of the peak energy of the CCSN. This is a concern because the mixing details of how the material moves in these 1-D stellar models are described by mixing length theory (MLT) which is a time-averaged theory over a pressure scale height. Bazan and Arnett (1994) found in their 2D simulation of convective O-burning that the region was not accurately described by MLT and was spherically asymmetric. They also speculate that the details of nucleosynthesis would be affected by this, which was confirmed in the 3-D simulations of a O-C merger by Rizzuti et al. (2024a). The way that mergers occur in Rizzuti et al. (2024a) is also significantly different to how it occurs in 1-D. In their 1-D model, just as in Ritter et al. (2018b), the upper boundary of the convective O-shell grows in extent, but in their 3-D merger models the bottom boundary of the convective C-shell extends down and subsumes the convective Ne- and O-burning shells. This underscores how different the macrophysics in 3-D can be compared to 1-D. Herwig et al. (2011) also found that MLT does not accurately describe how mixing occurs in convective-reactive environments. Additionally, in their 3-D O-shell burning simulation, Jones et al. (2017) found that MLT both underestimates the convective velocities and the qualitative shape of those velocities when compared to the 3-D radially averaged velocities. Andrassy et al. (2020) found in their 3-D O-C shell mergers that the merger had large-scale non-radial asymmetries that significantly deviated from the spherically symmetric scenario. These asymmetries are also seen in the 3-D O-Ne shell merger simulations of Yadav et al. (2020). Collins et al. (2018) also argue that MLT does not accurately describe the convective shell burning velocities as well as both the properites

of the shell mergers and how it responds to nuclear burning. They also identify that the O-burning shell in the O-C shell merger would not be well-mixed as the C-shell material burns as it mixed downwards. This is a marker of this being a convective-reactive environment as seen in Ritter et al. (2018a). It is clear that a 1-D spherically symmetric MLT is inadequate to describe the mixing details of the O-C shell merger. Since the O-C shell merger dominates the production of many of the p-nuclei and the mixing details of the O-shell are not well understood in 1-D, the nucleosynthesis is left an open question.

To address the insufficiencies in MLT, we present in this paper a 3D-hydrodynamic inspired approach to 1-D modelling to determine the impact of the mixing on the nucleosynthesis of the γ -process in the O-shell as C-shell material is entrained. By incorporating the insights from 3-D O-shell burning and O-C shell merger simulations, the impact on nucleosynthesis related to the mixing details in 1-D can be demonstrated. In addition to this, the impact of nuclear physics in this situation will also be explored. In Section 2.2 we present the methods of how the Ritter et al. (2018b) model is post-processed, how the 3-D hydrodynamic results are incorporated, and how the nuclear physics impact is determined. In Section 2.4.1 we explore the nucleosynthesis pathways of γ -process in this convective-reactive environment. Next, in Sections 2.4.2-2.4.4 we explore how different mixing details can impact the production of the p-nuclei. Section 2.4.2 explores the introduction of a convective downturn at the bottom of the O-shell, Section 2.4.3 explores how the ingestion rate impacts the production, and Section 2.4.4 explores the impact from both a GOSH-like event and partial merger. Then in Section 2.4.5 the impact from the nuclear physics and its relationship to the mixing details is explored. We will not be considering how modification of the initial seed composition in the C-shell or metallicity, how other models with O-C shell mergers are affected by changes to the mixing, providing nuclear physics uncertainties, investigating the effects of rotation, nor continuing stellar evolution and subsequent CCSN of the model. Additionally, we will only consider how the O-shell behaves under these conditions and not include the C-shell in the post-processing as the material will only be mixed up higher and no longer undergo the γ -process because it will be too cold. This O-shell post-processing will be static with a constant ingestion rate as stellar evolution with dynamic effects like energy feedback will not be calculated.

2.2 Methodology

In this paper we post-process the massive stellar model $M_{\text{ZAMS}} = 15M_{\odot}$, $Z = 0.02$ in the NuGrid data set (Ritter et al., 2018b). This model has a merger of its convective O and C-

burning shells late in its evolution as shown in Figure 2.1. During this merger, the C-burning ashes and *s*-process material are ingested into the much hotter O-burning shell.

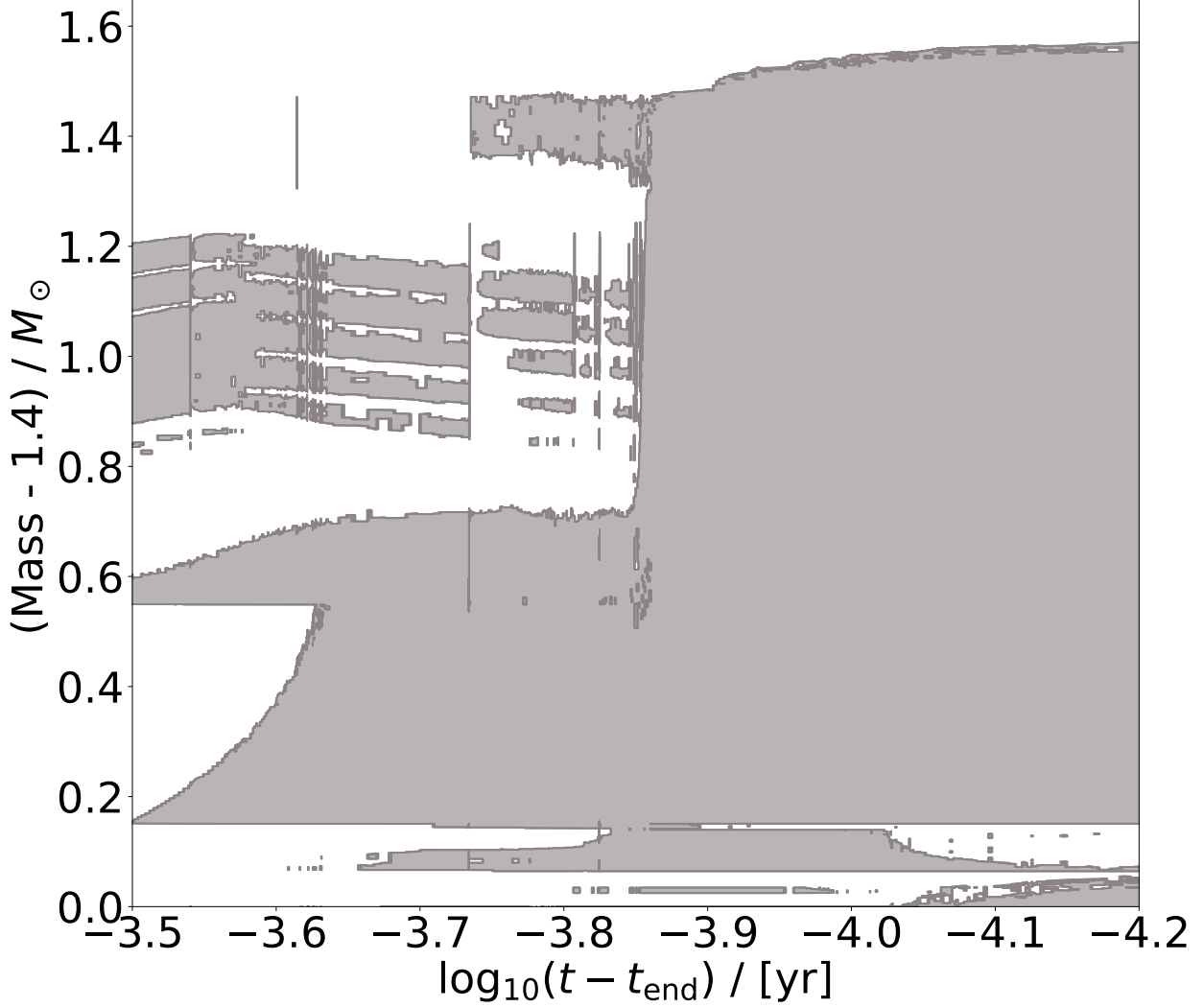


Figure 2.1: Kippenhahn diagram showing the merger of the convective O and C-burning shells. The O-burning shell extends from $1.55M_{\odot}$ to $1.95M_{\odot}$. The first convective C-burning shell sits directly on top from $1.96M_{\odot}$ to $2.11M_{\odot}$ and additional convective C-burning shells that are subsumed are above. The merger onsets at $\log_{10}(t - t_{\text{end}})/\text{yr} \approx -3.85$ and reaches full extent at ≈ -4 .

The detailed nucleosynthesis is calculated with the 1-D multi-zone post-processing code MPPNP using a nuclear network of 1470 isotopes to post-process only the O-shell. MPPNP does not include isomeric states in its network, so the nucleosynthesis of the p-nuclei ^{180m}Ta is not calculated although we calculate the production of the ground state ^{180}Ta . In addition to calculating the nucleosynthesis for each timestep, the species in the O-shell is also decayed

at a temperature of $T = 100$ MK without contributions from explosive nucleosynthesis. The results of this work are presented in terms of an overproduction compared to the solar measurement OP given by the equation

$$\text{OP} = \log_{10} \left(\frac{X_i}{X_{i,\odot}} \right)$$

where X_i is the final decayed mass fraction of a species in the O-shell and $X_{i,\odot}$ is the solar measurement of the species from Grevesse and Noels (1994).

A static stellar structure is taken from the onset of the merger at $\log_{10}(t - t_{\text{end}})/\text{yr} = -3.856$ and an initial isotopic composition from right before onset of merger $\log_{10}(t - t_{\text{end}})/\text{yr} = -3.845$. As such, we calculate C-shell ingestion for 110 seconds with a constant ingestion rate of $4 \times 10^{-3} M_{\odot}\text{s}^{-1}$ for all models except those in Section 2.4.3. This rate is the mass of the O-shell divided by the ingestion time. To determine the behavior during the merger, the diffusion coefficient profile is forced into a merged state as seen in Figure 2.2.

2.2.1 1-D implementation of 3-D macrophysics

Since the predictive power of MLT on the mixing is insufficient, we incorporate insights from 3D-hydrodynamic simulations into our 1-D models. In their 3-D convective O-burning simulation Jones et al. (2017) found that a convective profile downturn is present in the 3-D radially averaged convective velocity profile that is not found in MLT. That means that MLT predictions cannot describe behaviour in this region at all. MLT also underpredicts the strength of the convective velocities in this region. Jones et al. (2017) found that convective velocities are stronger by a factor of ~ 30 when compared to the MLT predictions. Andrassy et al. (2020) in their 3-D C-shell entrainment simulations that their velocities could be a factor of ~ 5 stronger depending on the strength of carbon and oxygen burning, and Rizzuti et al. (2024a) a boost of ~ 10 due to the feedback of new reactions from the ingested material in their 3-D O-C shell mergers. The downturn in the profile is incorporated in this work using the recommendation from Jones et al. (2017):

$$D_{\text{3D-insp.}} = \frac{1}{3} v_{\text{MLT}} \times \min(\ell, r - r_0) \quad (2.1)$$

where ℓ is the mixing length and r_0 is the Schwarzschild boundary at the bottom of the O-shell and an increasingly strong boost factor is applied of $3\times$, $10\times$, and $50\times$ to the convective

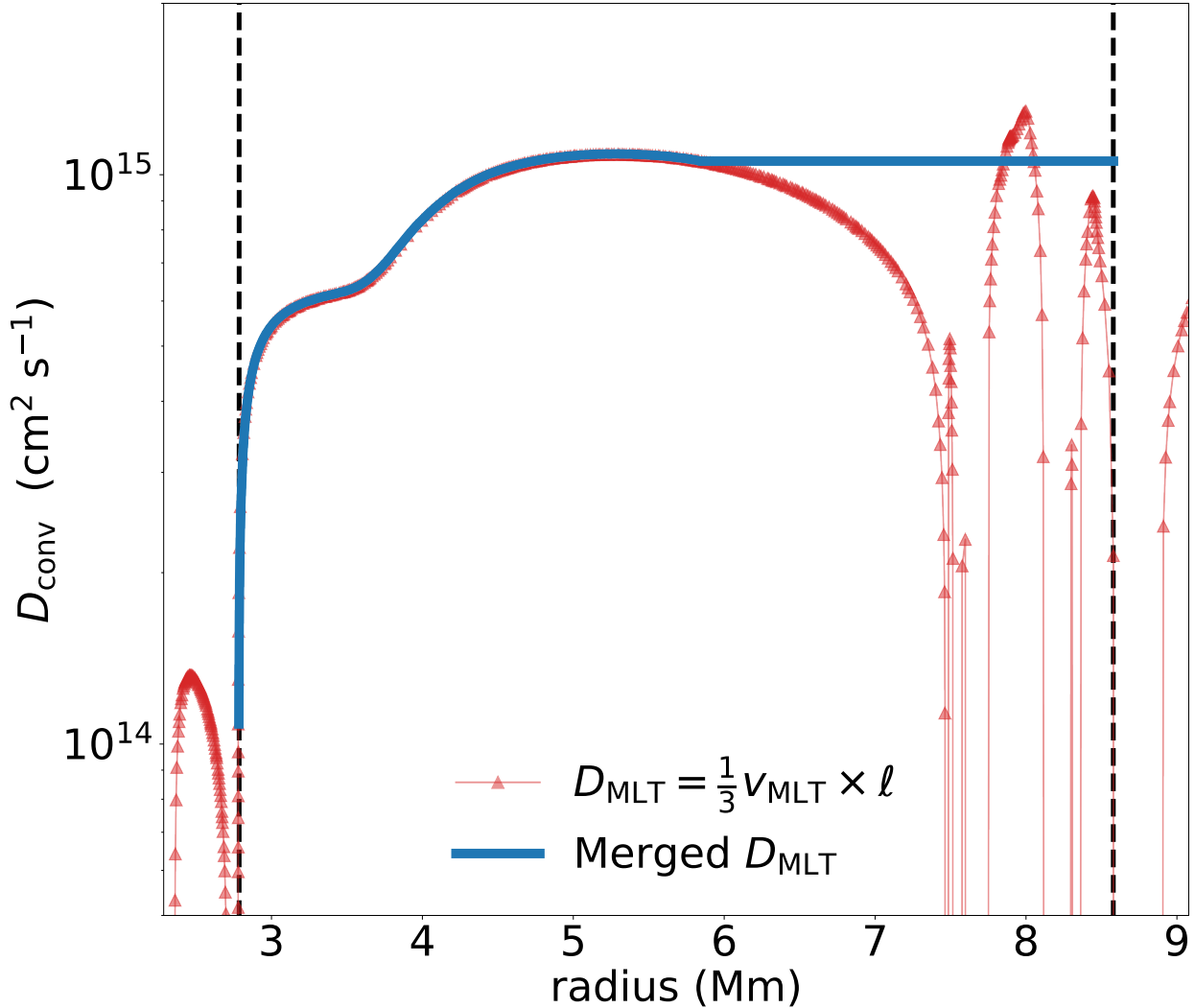


Figure 2.2: The diffusion coefficient profile predicted by MLT at model number 9160 for the $M_{\text{ZAMS}} = 15M_{\odot}$, $Z = 0.02$ model and the forced merger profile for the O-shell. The red line with triangles is the MLT prediction and the blue line is the forced merger. The black lines are the boundaries of the convective O-burning shell.

velocities as shown in Figure 2.3 to match what is seen in the 3-D simulations.

The $50\times$ boost factor is higher than what is seen in these simulations, but it is possible that they underestimate the boost in convective velocities from the feedback of ingested material reacting in the O-shell since they have limited nuclear networks. Although Jones et al. (2017) considers the downturn at the top of the O-shell, it is adopted at the bottom of this shell as it is understood to be merged with the C-shell on top. This is justified by the simulations done by Meakin and Arnett (2007) who show a downturn at both the bottom and top of their 2-D and 3-D O-shell burning simulations. Another insight from 3-D models is that the entrainment rate of the C-shell could vary (Andrassy et al., 2020). To investigate how this impacts the p-nuclei, a rate of $4 \times 10^{-5} M_{\odot} s^{-1}$ and $4 \times 10^{-4} M_{\odot} s^{-1}$ are also calculated along with our default rate of $4 \times 10^{-3} M_{\odot} s^{-1}$ for the MLT and all 3D-inspired mixing scenarios. In addition to this, a scenario is considered for all mixing scenarios where there is no ingestion of C-shell material.

There are other potential effects that can be considered during this merger. As there is energy feedback from the ingested C-shell material, this could cause a split in the convective profile as seen in Herwig et al. (2011). Herwig et al. (2014) found this effect could happen during the ingestion of H into a He-shell in their 3D simulations and labelled this effect Global Oscillation of Shell H-ingestion (GOSH). It could be that the energy feedback from the ingested C-shell material could have a similar effect to a GOSH. Andrassy et al. (2020) found that strong oscillatory modes were present in their 3-D simulations of C-shell entrainment into an O-shell. Another potential effect is that the convective profiles of the O-shell and C-shell do not fully merge. To determine the impact on nucleosynthesis in both a GOSH-like and partial merger event, both scenarios are tested at two different strengths each. Using

$$D_{\text{dip}} = D_{\text{MLT}} - (D_{\text{MLT}} - c) \times \exp \left[-\frac{(r - a)^2}{w^2} \right] \quad (2.2)$$

a dip is put into the diffusion coefficient profile D_{conv} where c is the minimum value of the dip, w the width, and a the center. For all four scenarios have a width $w = 0.25$ Mm, the weaker of the scenarios the dip descends to $c = 10^{14} \text{ cm}^2 \text{s}^{-1}$ and the stronger $c = 10^{13} \text{ cm}^2 \text{s}^{-1}$. The GOSH-like scenarios are centered at $a = 4.95$ Mm where $D_{\alpha} = 1$ for ${}^{20}\text{Ne}(\gamma, \alpha){}^{16}\text{O}$ which could be one of the sources for this energy feedback at peak ${}^{20}\text{Ne}$ burning. The partial merger scenarios are centered at $r = 7.5$ Mm where the unmerged D_{MLT} has a dip as seen in Figure 2.2. The profiles for the GOSH-like and partial merger scenarios are shown in Figure 2.4.

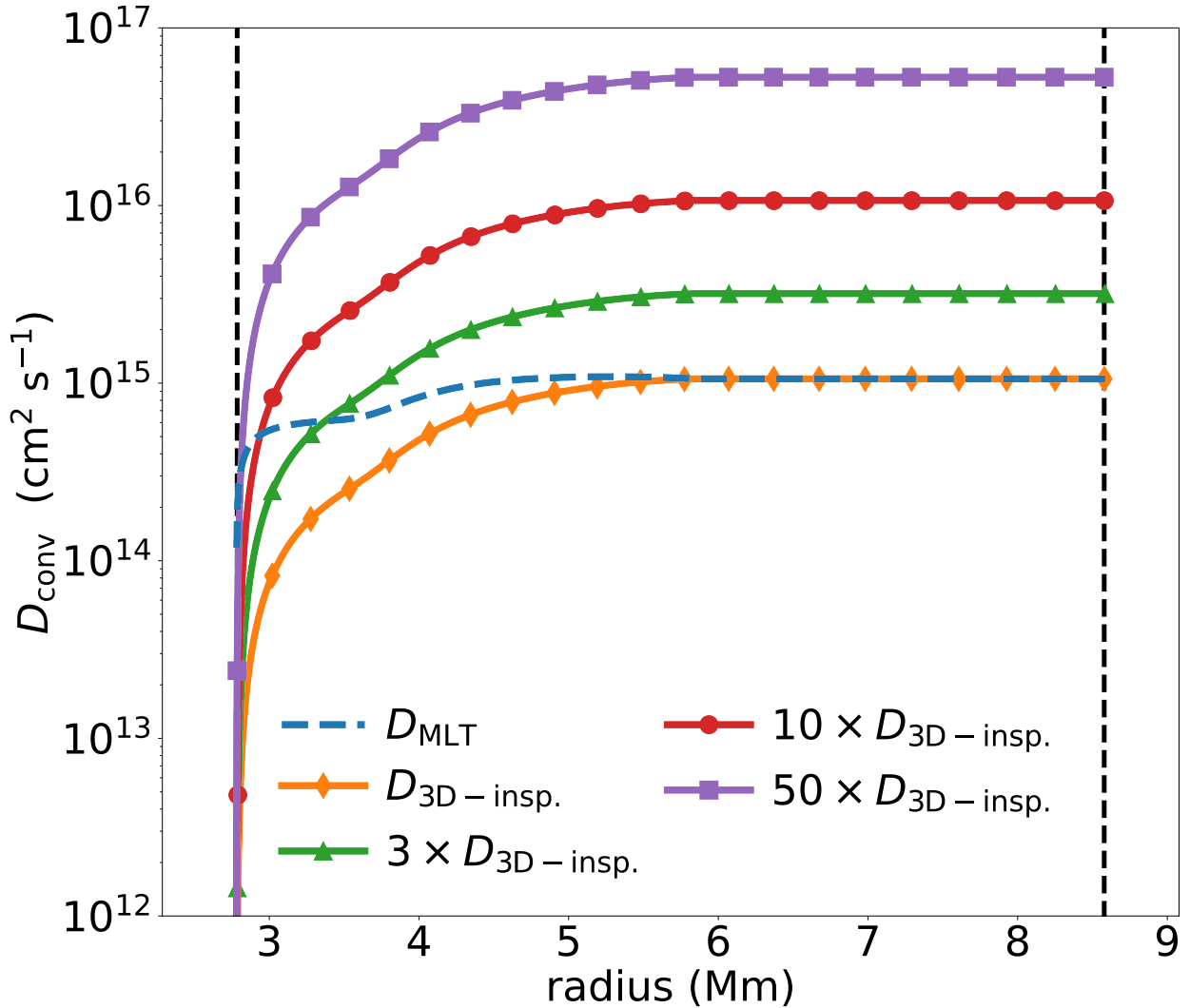


Figure 2.3: The diffusion coefficient profiles for the 3D-inspired mixing scenarios. The blue dashed line is the merged D_{MLT} profile, the orange line with diamonds, green line with triangles, red line with red circles, and purple line with squares are those calculated using $D_{\text{3D-insp.}}$ with boost factors of 1, 3, 10, and 50 respectively.

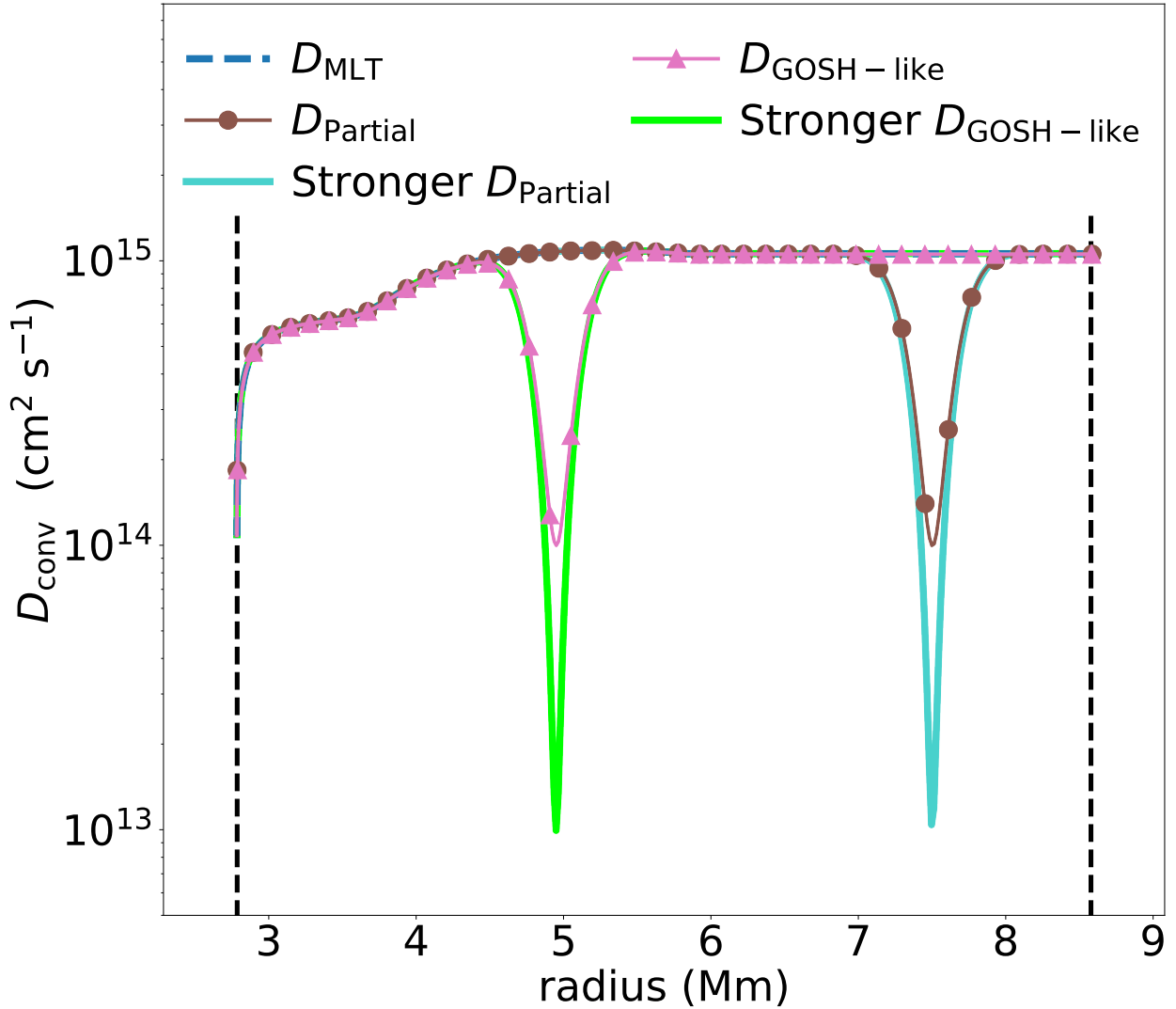


Figure 2.4: The MLT, GOSH-like, and partial merger diffusion coefficient profiles. The blue dashed line is D_{MLT} , the pink line with triangles and lime line are potential GOSH-like splits in the profile centered at $r = 4.95$ Mm, the purple line has a dip that is $10\times$ deeper. The brown line with circles and the turquoise line are partial mergers $r = 7.5$ Mm, the gray line has a dip that is $10\times$ deeper. The black dashed lines are the edges of the O-shell.

2.2.2 Determining nuclear physics impact

There are many unmeasured reaction rates for the unstable proton heavy isotopes from Se – Po which means that there is a possible variation in the input nuclear physics of the γ -process. To determine the impact of varying the nuclear physics in this region, the photo-disintegration rates (γ, α) , (γ, p) , (γ, n) for all unstable proton heavy isotopes from Se – Po are varied in our network along with their corresponding capture rates by a random factor between 0.1 to 10 that is uniformly selected in a Monte Carlo (MC) way for 1000 scenarios. This extends the approach performed by Denissenkov et al. (2018) and Denissenkov et al. (2021) for (n, γ) rates in an i-process context. This was done for the MLT mixing scenario and the four 3D-inspired mixing scenarios but not the GOSH-like and partial merger scenarios. This approach also allows for the identification of reaction rates that are relevant for the production of an isotope using correlations. The Pearson coefficient describes correlations between $X/X_{\text{no variation}}$ and the variation factors where X is the final decayed mass fraction of a Monte Carlo case and $X_{\text{no variation}}$ is the final decayed mass fraction for the default case where all variation factors are equal to 1. All correlations $|r_P| \geq 0.15$ are reported in this study. In addition to the Pearson coefficient, a logarithmic slope ζ is also reported to determine the importance of a reaction on the final mass fraction of an isotope. The importance of considering ζ as well as additional caveats for the correlated rates are discussed in Section 2.3.

2.3 Correlations of nuclear reaction rates

The Pearson correlation coefficient, r_P , is insufficient to quantify the importance of a correlated rate as demonstrated by Figure 2.5. A strong correlation does not correspond directly to a significant change to the final mass fraction of a species. In addition to the correlation coefficient, a slope ζ is provided that better describes this behaviour. ζ is the slope of a linear regression between $\log_{10}(X/X_{\text{no variation}})$ and $\log_{10}(\text{variation factor})$ where X is the final decayed mass fraction for Monte Carlo rates and $X_{\text{no variation}}$ is the final decayed mass fraction for the default case where all variation factors are equal to 1.

It is clear from Figure 2.5 that similarly correlations do not directly mean that the reaction rate is relevant for the production of a species, but the slope ζ also does not directly point to this. The bottom right plot showing the impact on the final mass fraction of ^{196}Hg from varying the input rate for $^{196}\text{Pb}(\gamma, n)$ has both a strong slope and correlation, but the bottom left plot has a strong correlation and a weak slope. Reaction rates that are both highly correlated and have a strong slope will have direct impact on the production of

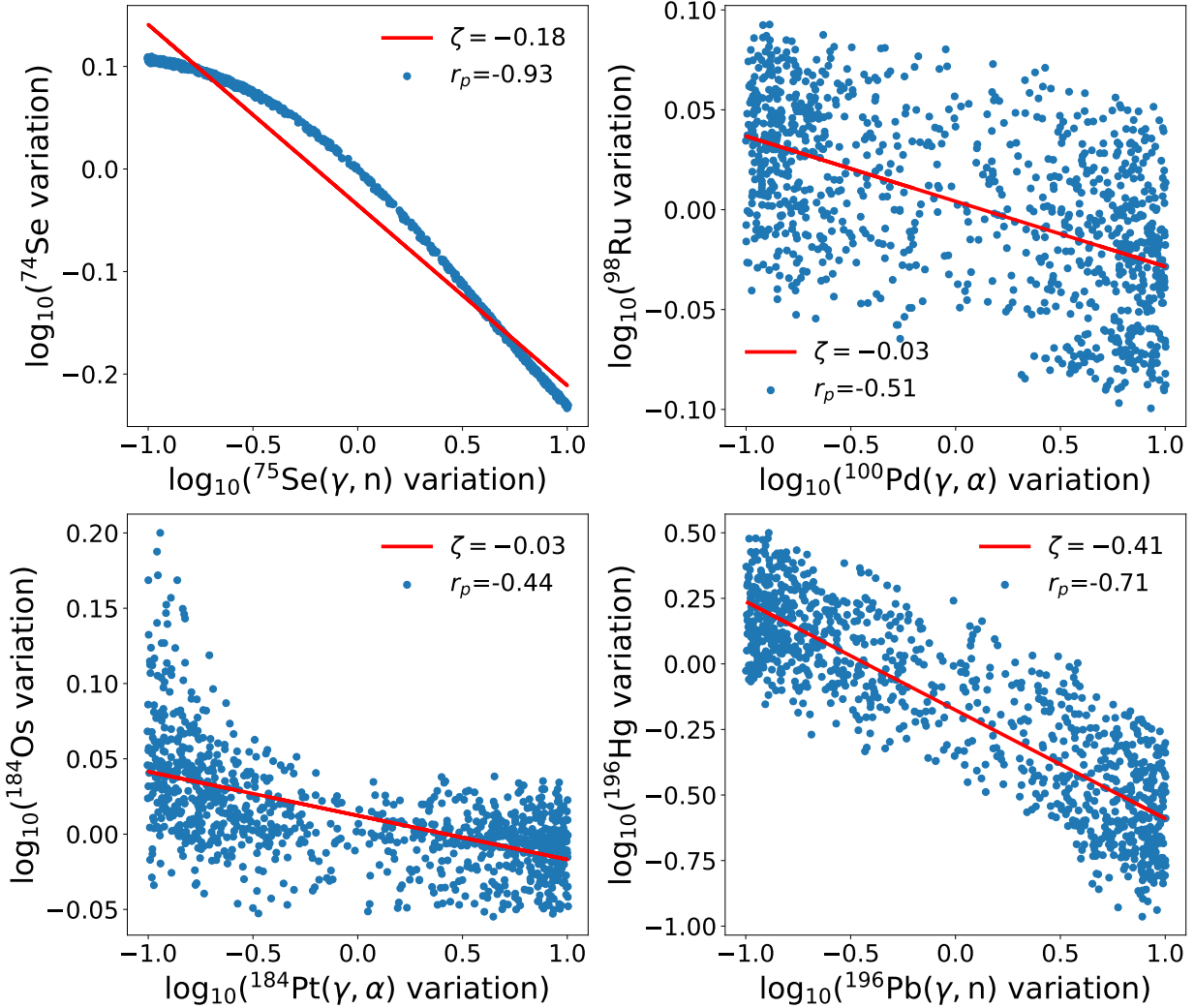


Figure 2.5: Examples of strongly correlated mass fractions with reaction rates for four species for the MLT mixing scenario. The blue dots are the values and the red line is the best linear fit to OP_{var} and $\log_{10}(\text{variation factor})$. The top left plot and bottom right plot show strong correlations for ^{74}Se and ^{196}Hg that directly impact the mass fraction. The top right plot shows a correlation for ^{98}Ru where there is considerable spread in the mass fraction. The bottom left plot shows a correlation for ^{184}Os where the mass fraction is strongly affected only for multiplication factors less than 1.

species.

Another caveat is that this method of varying the reaction rates in a Monte Carlo way does not distinguish between the photo-disintegration and corresponding capture rate. All correlated rates are reported according to their photo-disintegration rates, but as shown by the upper left plot of Figure 2.5 for ^{74}Se and $^{75}\text{Se}(\gamma, n)^{74}\text{Se}$ this results sometimes in saying that a reaction that would be considered a production term is strongly anti-correlated with production. This is because when we apply the variation factor, we do so for both $^{75}\text{Se}(\gamma, n)$ and $^{74}\text{Se}(n, \gamma)$. As Figure 2.6 shows, both of these reactions have relevant nucleosynthetic fluxes contributing to the final mass fraction of ^{74}Se .

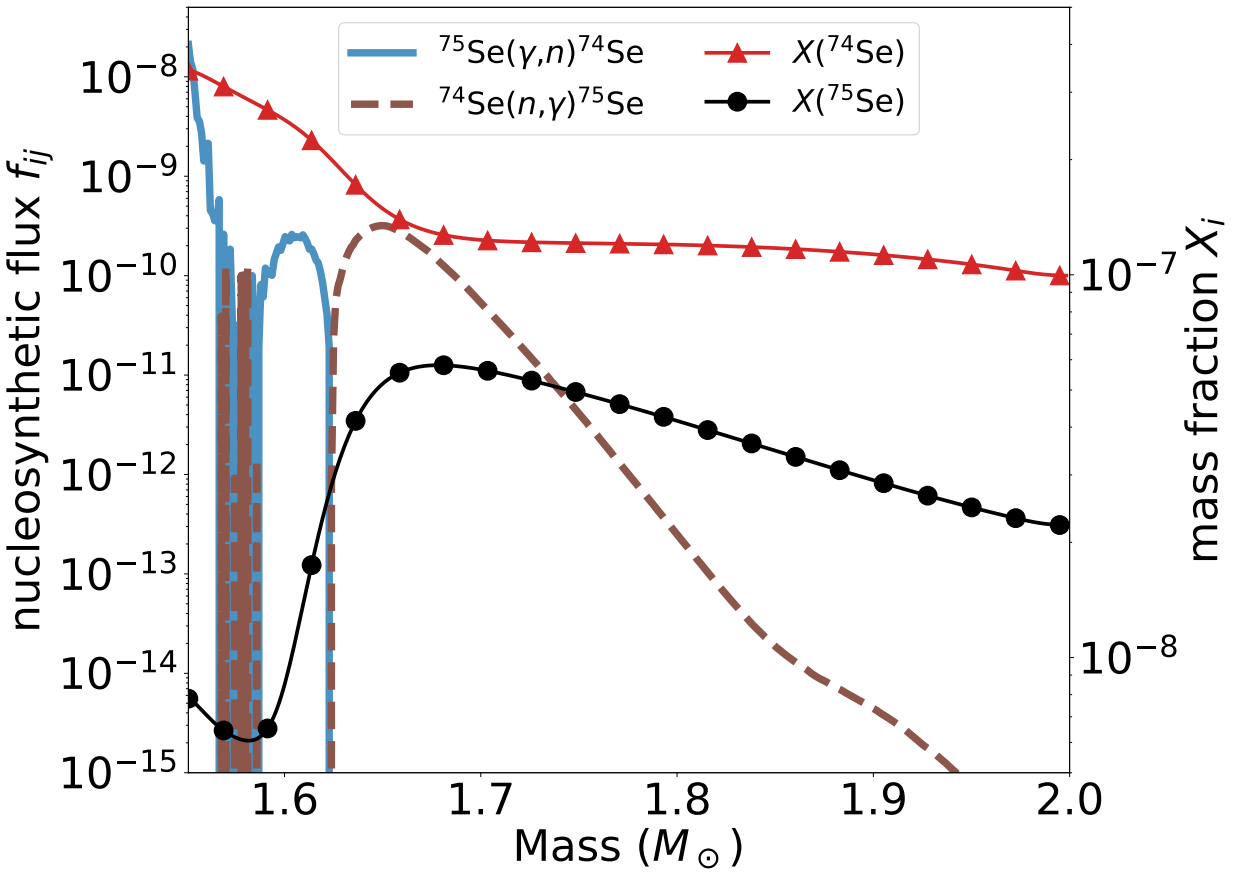


Figure 2.6: Nucleosynthetic flux and mass fraction plot for the MLT mixing case at $t = 110$ sec. The blue solid line and brown dashed line are $^{75}\text{Se}(\gamma, n)^{74}\text{Se}$ and $^{74}\text{Se}(n, \gamma)^{75}\text{Se}$ respectively. The red solid line with triangles and black solid line with circles are the mass fractions of ^{74}Se and ^{75}Se respectively.

This is not the case for all reactions as temperatures can be high enough that the capture rates are potentially not relevant, but as shown in Section 2.4.1 this is an environment where

species are co-producing each other and it could be the case.

2.4 Results

In this section we will first explore how a convective-reactive flow impacts the production of the p-nuclei for the mixing scenario using the diffusion profile predicted by mixing length theory. Then we show how the nucleosynthesis in this shell changes during mixing scenarios of a convective downturn at the bottom of the O-shell, varied ingestion rate, and dips in the convective profile due to GOSH-like feedback and partial merging between the O- and C-shells. Finally, we will present how varying the input nuclear physics impacts the production of the p-nuclei and how those results are related to the MLT and convective downturn mixing scenarios.

2.4.1 Convective-reactive production of the p-nuclei

Convective-reactive flow in 1-D models are characterized by a simultaneous advective and nucleosynthetic flow with similar timescales. This is one of the conditions that distinguishes this environment from the explosive O-shell nucleosynthesis other than the hotter temperatures of 2 – 4 GK for the Ne and O-shells of Roberti et al. (2024). Here we explore the details of how convective-reactive flow behaves in the MLT mixing scenario. Figure 2.7 shows how the mass fractions of various p-nuclei are produced across the shell.

The γ -process is a temperature dependent phenomena where heavier species are produced at cooler temperatures of 1.5 – 2 GK and destroyed at hotter temperatures, and the lighter species are produced at hotter temperatures of up to 3.5 GK but not produced at cooler temperatures (Rauscher et al., 2013), but advective flows in this O-shell allow for any given isotope regardless of its mass to be produced at their ideal temperature while still contributing to the nucleosynthesis of lighter species. Whether an individual isotope will react via (γ, n) and (n, γ) reactions to continue producing their element or contribute to the production of lighter p-nuclei by (γ, p) and (γ, α) reactions is temperature, and therefore mixing speed, dependent. One result of this is that we can identify locations of peak burning for heavier isotopes where the mass fraction of a species suddenly drops as seen for ^{156}Dy , ^{196}Hg , and to a lesser extent ^{144}Sm . As explained in the convective H-He shell mergers of Herwig et al. (2011), this is the location where the mixing speed becomes equal to the timescale for reactions. This is clearly contrary to what is normally seen in a convective environment where the species are well-mixed with no local features, and to reactive environments where species cannot be replenished because there is limited or no mixing hence why understand-

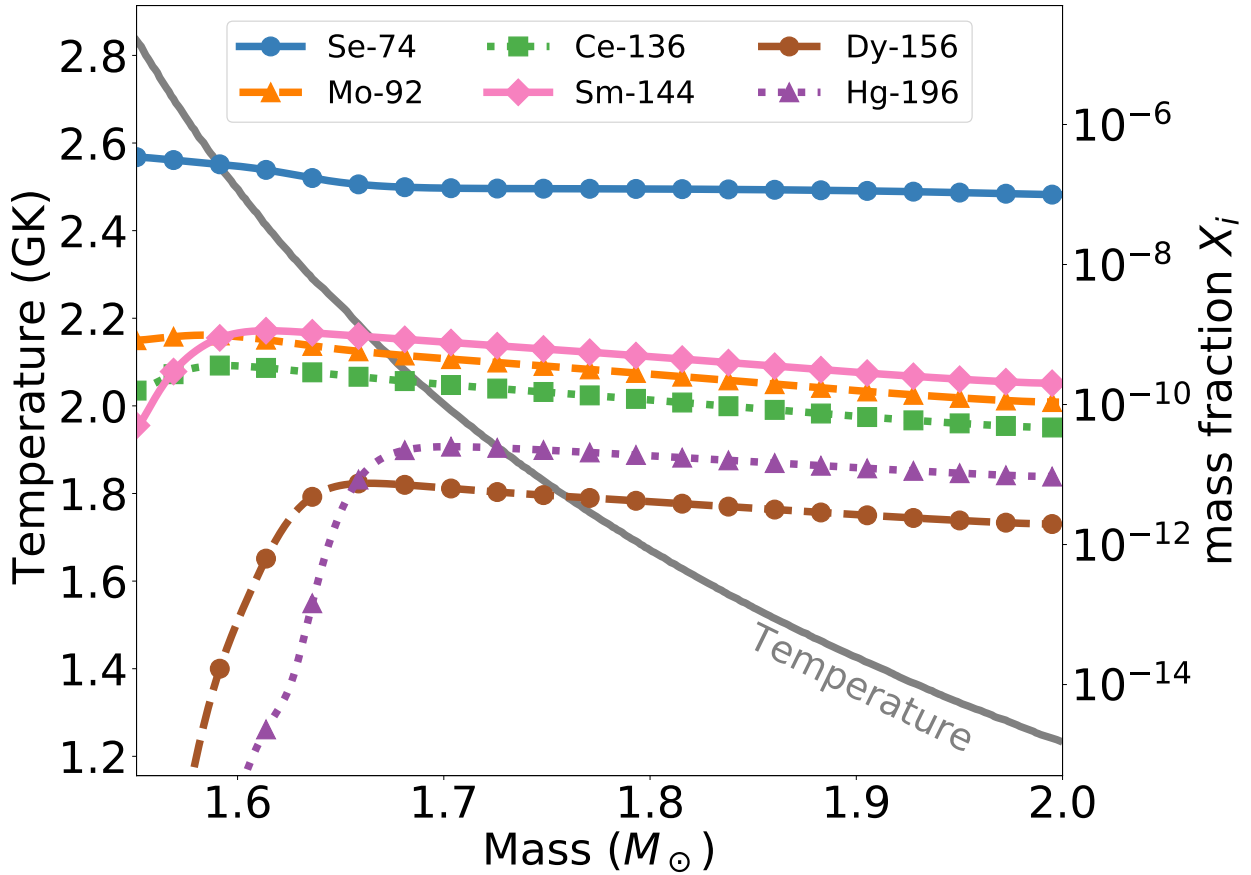


Figure 2.7: Temperature profile and mass fractions after $t = 110$ sec of ingestion for the MLT mixing scenario. The grey solid line is the temperature, the blue solid line with circles is ^{74}Se , the orange dashed line with triangles is ^{92}Mo , the green dotted line with squares is ^{136}Ce , the pink solid line with diamonds is ^{144}Sm , the brown dashed line with circles is ^{156}Dy , and the purple dotted line with triangles is ^{196}Hg .

ing this as a convective-reactive environment is necessary. Whether a species is advects or reacts can lead to unique nucleosynthetic pathways because heavier species are able to reach hotter temperatures that they would not reach and the products of their reactions can either continue to react in that location or move to another and react with the material there. Figures 2.8 and 2.9 show example fluxes at the same time and mass number but different mass coordinates.

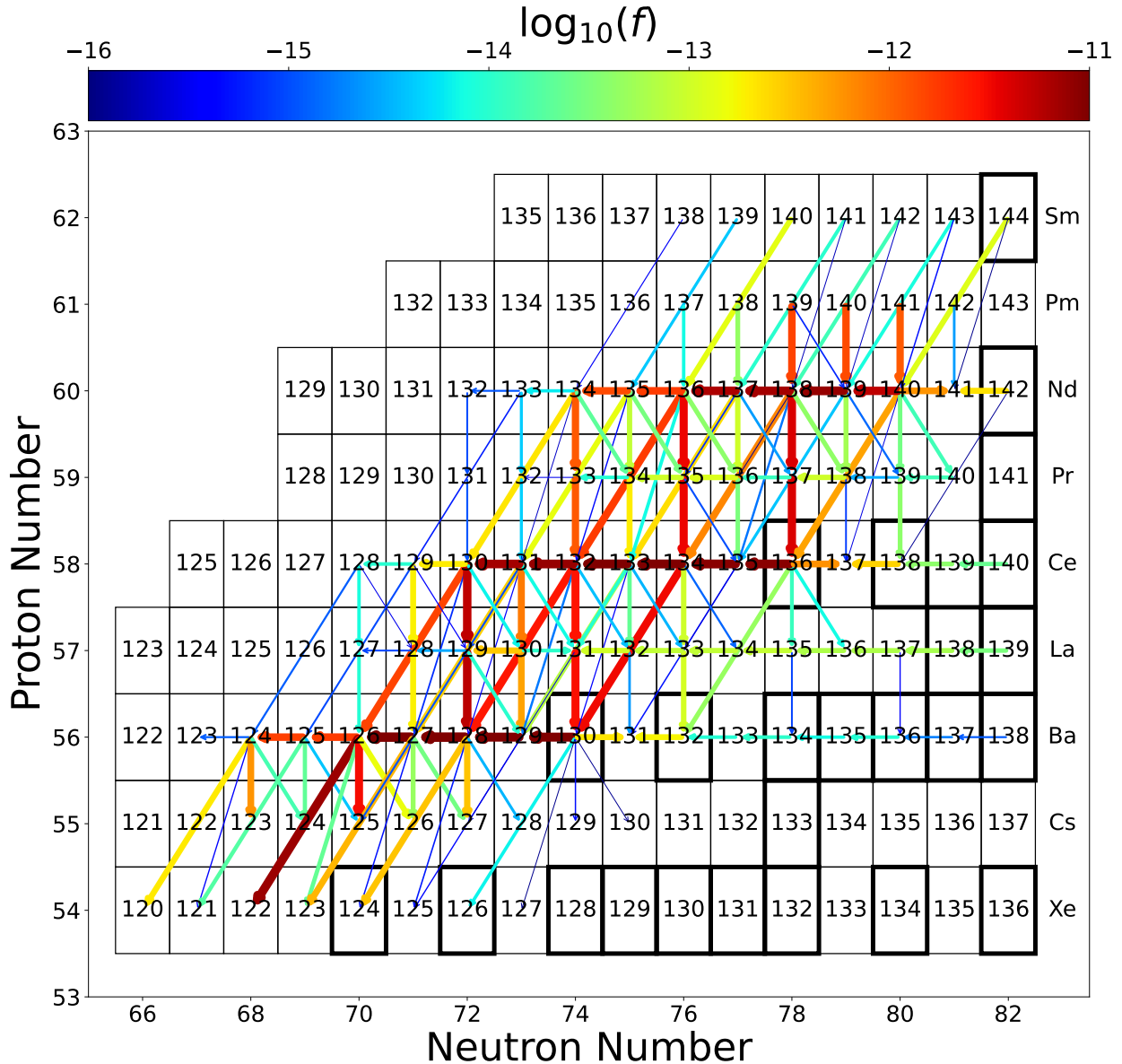


Figure 2.8: Nucleosynthetic fluxes f_{ij} at $m = 1.55103M_{\odot}$ for the MLT scenario for $t = 110$ sec of ingestion at 2.833 GK.

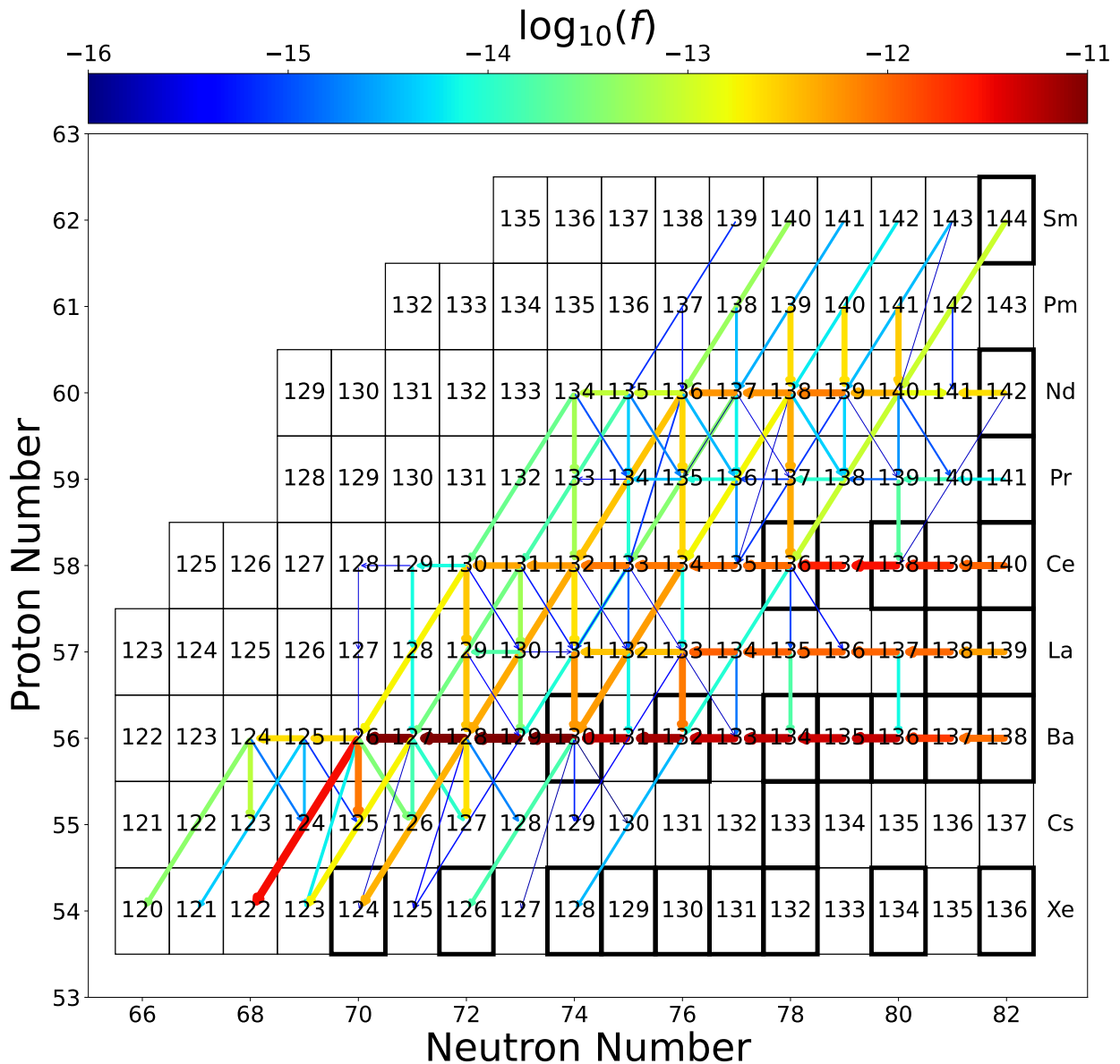


Figure 2.9: Nucleosynthetic fluxes f_{ij} at $m = 1.58017M_{\odot}$ for the MLT scenario for $t = 110$ sec of ingestion at 2.621 GK.

Fluxes in this shell are not conserved at local mass coordinates because a percentage of a species could be advected to another coordinate. Figure 2.8 shows ^{136}Ce is net destroyed more efficiently by $^{136}\text{Ce}(\gamma, n)^{135}\text{Ce}$ than its production by $^{137}\text{Pr}(\gamma, p)^{135}\text{Ce}$, but the mass fraction does not significantly drop as shown in Figure 2.7 at the bottom of the shell. This is because it is being produced by $^{137}\text{Ce}(\gamma, n)^{136}\text{Ce}$ at a slightly higher position of $m = 1.58017M_{\odot}$ as shown in Figure 2.9 and advected both left and right leading to the peak seen in Figure 2.7. Because ^{136}Ce is being continually replenished by an advective flow, it can continue to produce the unstable Ce isotopes which contribute significant nucleosynthetic fluxes to the production the unstable Ba, La, and Xe isotopes as well as the p-nuclei ^{130}Ba via $^{134}\text{Ce}(\gamma, \alpha)^{130}\text{Ba}$ and $^{132}\text{Ce}(\gamma, p)^{131}\text{La}(\gamma, p)^{130}\text{Ba}$ at $m = 1.55103M_{\odot}$ in addition to the Ba (γ, n) chain at $m = 1.58017M_{\odot}$. Another feature in the nucleosynthesis is that species are able to co-produce each other. Although not as strongly shown as it is at other mass coordinates, Figures 2.8 and 2.9 can show this for ^{136}Ce and ^{137}Ce . ^{137}Ce is both produced by ^{136}Ce and produces it depending on the mass coordinate because of the temperature differences. Because of the complex relationship between multiple different nucleosynthesis regimes, the exact pathways of production cannot be followed as simply as it could in typical convective or reactive environments. This raises questions on the impact of seeds as the convective-reactive environment has different s -, i -, and r -seeds present depending on the local mass coordinate. Figure 2.7 clearly shows that there is an unequal share of material present as the heaviest seeds are not present at the hottest temperatures and will not be destroyed via (γ, α) to the lightest p-nuclei but stop at a certain point, although their products are advected deeper in the shell to the hottest temperatures. This demonstrates the importance of following how γ -process nucleosynthesis behaves in this convective-reactive O-shell.

2.4.2 Mixing scenario 1: Convective downturns

3-D hydrodynamic simulations show that the MLT mixing scenario is not accurate for the O-burning shell. Here we present how the final nucleosynthesis is impacted in the alternative mixing scenario of a convective downturn (Jones et al., 2017) in Figure 2.10 and will refer to the convective downturn cases as 3D-inspired and their boost factors as done in Figure 2.3. Across the MLT and all 3-D inspired convective downturn mixing scenarios, there is an average spread in the production of the p-nuclei 0.96 dex.

The presence of a convective downturn increases production globally. The MLT mixing scenario has an OP of 0.64 dex and the 3D-inspired scenarios have 0.98 dex, 1.23 dex,

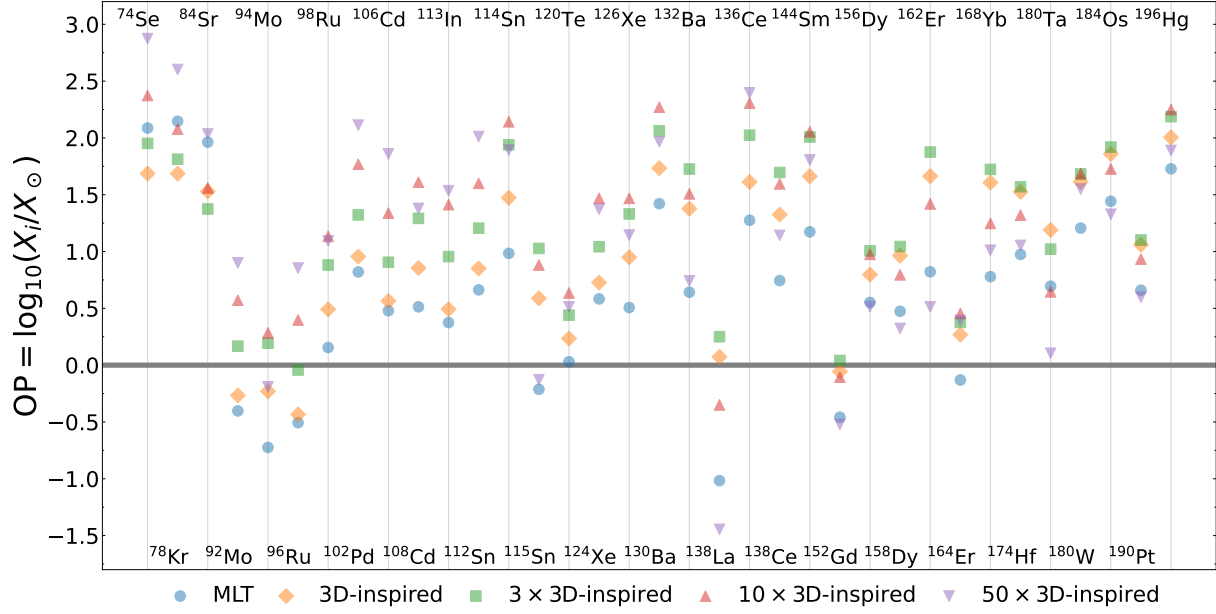


Figure 2.10: The overproduction compared to the solar measurement of the p-nuclei. The blue circle corresponds to the MLT scenario, orange diamond to the 3D-inspired scenario, green square to $3 \times$ 3D-inspired scenario, right side up red triangle to $10 \times$ 3D-inspired, and upside down purple triangle to $50 \times$ 3D-inspired. The thick grey line at $OP = 0$ corresponds to the solar measurement. The average spread in production is 0.96 dex.

1.30 dex, and 1.12 dex for the $1 \times$, $3 \times$, $10 \times$, $50 \times$ 3D-inspired mixing scenarios respectively. Comparing the MLT and $1 \times$ cases, all species from ^{92}Mo to ^{196}Hg have their production increased by the appearance of a downturn except the lightest three p-nuclei which are instead decreased. This is because the mixing speeds at the hottest temperatures are significantly lower, limiting how much of the heavier material is efficiently burned into lighter products. Local production is not uniformly increased across all the p-nuclei from the downturn. For example, comparing the MLT and $1 \times$ cases again, ^{168}Yb is increased by 0.83 dex but ^{156}Dy is only increased by 0.25 dex. As the mixing speeds in the 3D-inspired scenario increase, the local and global production changes in a non-linear and non-monotonic way. Global production decreases for the $50 \times$ 3D-inspired scenario because the species are now being advected fast enough to the bottom of the O-shell that the decreasing velocities no longer impede production. Comparing ^{98}Ru and ^{162}Er , both species increase in production as the mixing speed increases, but at the $50 \times$ scenario ^{162}Er is decreased by 0.91 dex compared to the $10 \times$ scenario whereas ^{98}Ru is produced about the same.

Another feature that can be seen in Figure 2.10 is that the ratio of any two isotopic pairs is dependent on the mixing scenario. In the γ -process, isotopes are related by (γ, n) and

(γ, α) reactions which are temperature dependent, and because the mixing speed determines how much of the material will reach a certain temperature it changes whether an element will be destroyed into another. For the $^{92,94}\text{Mo}$ pair, the MLT, 10 \times , and 50 \times mixing scenarios ^{92}Mo is more abundant, and in the 1 \times and 3 \times scenarios they are nearly equal. For the $^{106,108}\text{Cd}$ pair, they are equal for the MLT mixing scenario, and then for all but the 50 \times scenario ^{108}Cd is more abundant. Similarly for the Sn isotopes, ^{114}Sn is more abundant than ^{112}Sn except for the 50 \times 3D-inspired mixing scenario. Not all pairs behave like this, however, as ^{98}Ru and ^{136}Ce are more abundant than ^{96}Ru and ^{138}Ce . This demonstrates that the presence of a convective downturn is significant for the production of the p-nuclei.

2.4.3 Mixing scenario 2: Varying the ingestion rate

3-D simulations suggest that entrainment rates of C-shell ashes into the O-shell can be much lower (Andrassy et al., 2020). Here we present the impact of lowering the rate of ingesting material from the C-shell for the MLT mixing scenario in Figure 2.11 and the convective downturn scenarios in Figures 2.12–2.15.

The results show how the p-nuclei production is boosted by the ingestion of the C-shell material for all species except ^{74}Se , ^{78}Kr , and ^{84}Sr . These three isotopes decrease with ingestion rate because they are net destroyed during the O-C shell merger as the hottest temperature γ -process temperatures are not reached in this shell as Figure 2.7 shows. All other isotopes have a boost in their production in a similar way for all isotopes with an increase in ingestion rate, and demonstrate diminishing returns as ingestion rate increase. Additionally, the convective downturn cases have significant underproductions of ^{115}Sn , ^{138}La , ^{152}Gd , and ^{180}Ta . For the 10 and 50 boost factor cases all p-nuclei $A \geq 115$ are underproduced and $A \geq 152$ are dramatically underproduced. This shows how the presence of an O-C shell merger is necessary for pre-explosive γ -process to dominate the production of the p-nuclei. Across the MLT and convective downturn cases the average spread in production of cases with C-shell ingestion are 1.22, 1.58, 1.65, 1.78, and 1.84 dex. This global spread in production grows with mixing speed shows the importance of the mixing speeds. Across ingestion rate the pattern of the isotopes and ratios between pairs are generally preserved, although this is not always the case as shown with the Sn isotopes for the 50 \times convective downturn scenario. This demonstrates the importance of the O-C shell merger and the impacts of ingestion rate on the production of the p-nuclei.

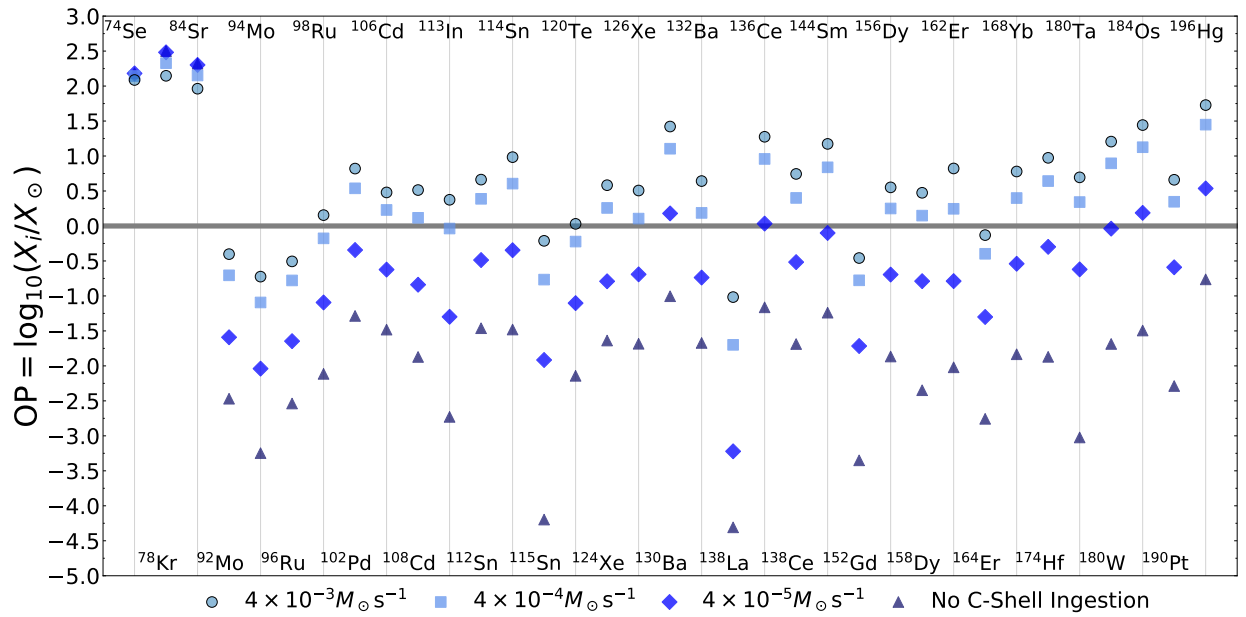


Figure 2.11: Overproduction compared to solar for the MLT mixing scenario for each ingestion rate. The circle with a black outline corresponds to the base ingestion rate $4 \times 10^{-3} M_\odot s^{-1}$, which is the same as the MLT values in Figure 2.10. The square corresponds to a rate of $4 \times 10^{-4} M_\odot s^{-1}$, the diamond corresponds to a rate of $4 \times 10^{-5} M_\odot s^{-1}$, and the triangle corresponds to no ingestion of C-shell material. The thick grey line at $\text{OP} = 0$ corresponds to the solar measurement. The average spread in production excluding the no ingestion scenario is 1.22 dex.

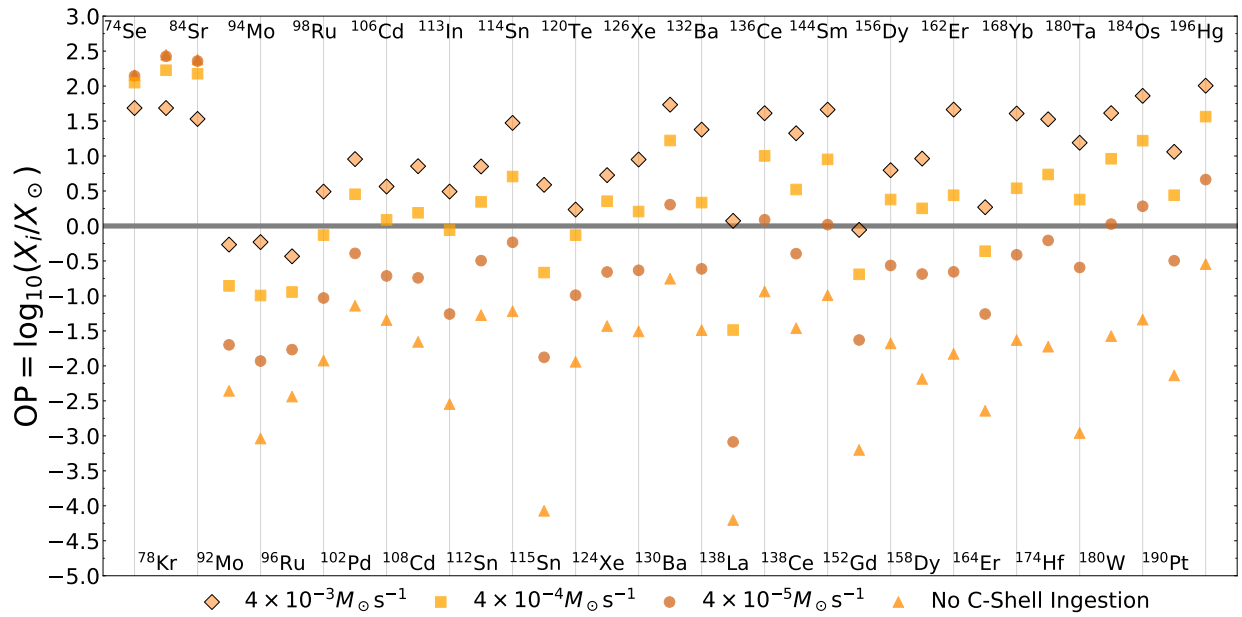


Figure 2.12: Overproduction compared to solar for the 3D-inspired mixing scenario for each ingestion rate. The diamond with a black outline corresponds to the base ingestion rate $4 \times 10^{-3} M_\odot s^{-1}$, which is the same as the 3D-inspired values in Figure 2.10. The square corresponds to a rate of $4 \times 10^{-4} M_\odot s^{-1}$, the circle corresponds to a rate of $4 \times 10^{-5} M_\odot s^{-1}$, and the triangle corresponds to no ingestion of C-shell material. The thick grey line at $\text{OP} = 0$ corresponds to the solar measurement. The average spread in production excluding the no ingestion scenario is 1.58 dex.

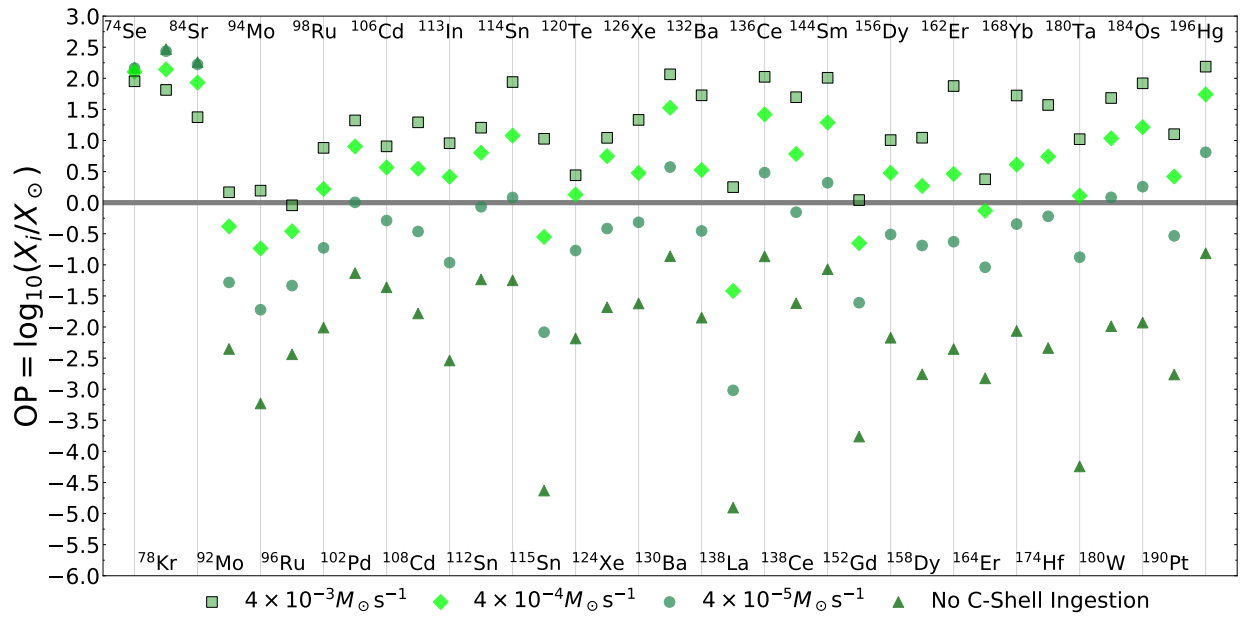


Figure 2.13: Overproduction compared to solar for the 3×3 D-inspired mixing scenario for each ingestion rate. The square with a black outline corresponds to the base ingestion rate $4 \times 10^{-3} M_\odot s^{-1}$, which is the same as the 3×3 D-inspired values in Figure 2.10. The diamond corresponds to a rate of $4 \times 10^{-4} M_\odot s^{-1}$, the circle corresponds to a rate of $4 \times 10^{-5} M_\odot s^{-1}$, and the triangle corresponds to no ingestion of C-shell material. The thick grey line at $\text{OP} = 0$ corresponds to the solar measurement. The average spread in production excluding the no ingestion scenario is 1.65 dex.

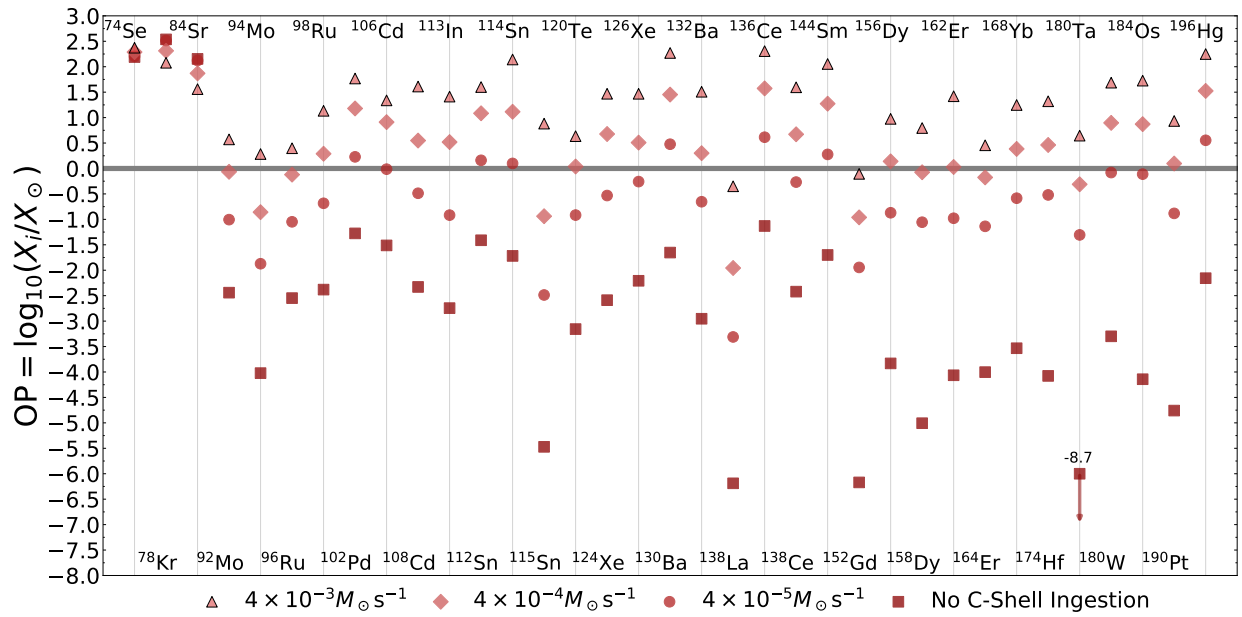


Figure 2.14: Overproduction compared to solar for the $10 \times 3D$ -inspired mixing scenario for each ingestion rate. The triangle with a black outline corresponds to the base ingestion rate $4 \times 10^{-3} M_{\odot} s^{-1}$, which is the same as the $10 \times 3D$ -inspired values in Figure 2.10. The diamond corresponds to a rate of $4 \times 10^{-4} M_{\odot} s^{-1}$, the circle corresponds to a rate of $4 \times 10^{-5} M_{\odot} s^{-1}$, and the square corresponds to no ingestion of C-shell material. If a point would be plotted out of range, it is denoted with an arrow and its value. The thick grey line at $OP = 0$ corresponds to the solar measurement. The average spread in production excluding the no ingestion scenario is 1.78 dex.

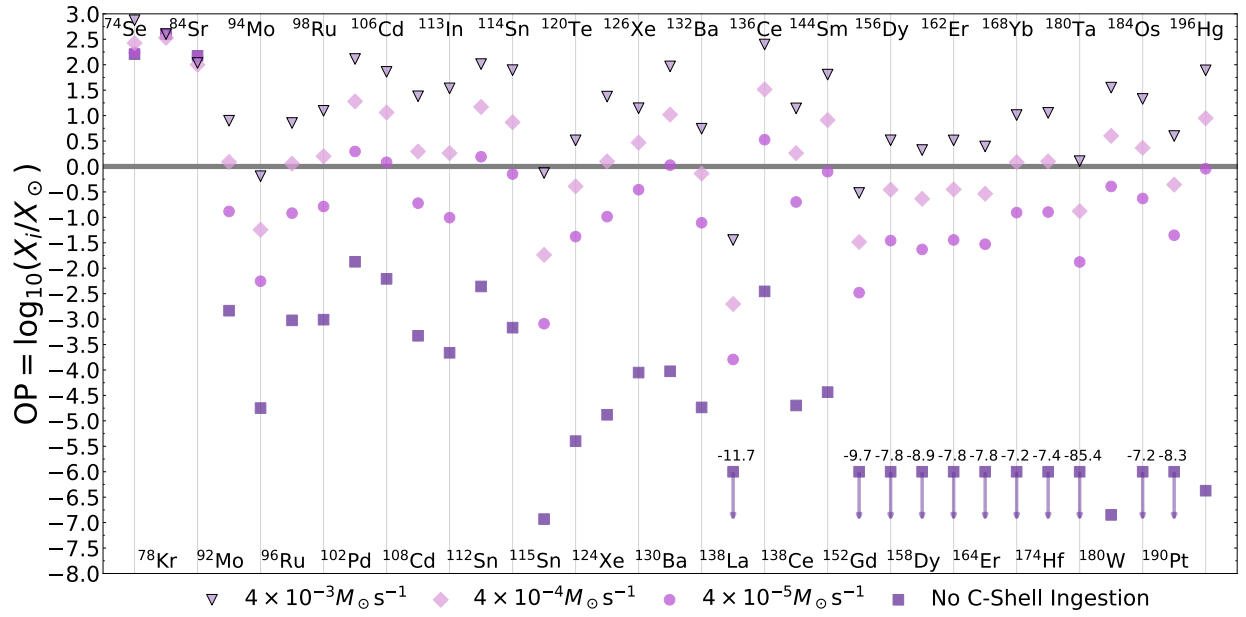


Figure 2.15: Overproduction compared to solar for the $50\times$ 3D-inspired mixing scenario for each ingestion rate. The upside down triangle with a black outline corresponds to the base ingestion rate $4 \times 10^{-3} M_{\odot} \text{s}^{-1}$, which is the same as the $50\times$ 3D-inspired values in Figure 2.10. The diamond corresponds to a rate of $4 \times 10^{-4} M_{\odot} \text{s}^{-1}$, the circle corresponds to a rate of $4 \times 10^{-5} M_{\odot} \text{s}^{-1}$, and the square corresponds to no ingestion of C-shell material. If a point would be plotted out of range, it is denoted with an arrow and its value. The thick grey line at $\text{OP} = 0$ corresponds to the solar measurement. The average spread in production excluding the no ingestion scenario is 1.84 dex.

2.4.4 Mixing scenario 3: Convective dips from GOSH-like feedback and a partial merger

O-C shell mergers experience non-radial, spherically asymmetric instabilities like GOSHs due to energy feedbacks (Andrassy et al., 2020) and could experience dips in the convective profile. Here we present the impact on the final production of p-nuclei from considering a dip in the convective profile from a GOSH-like event and a partial merger in Figure 2.16. The impact of the GOSH-like and the partial merger scenarios impact the production of the p-nuclei in a very similar way for all isotopes with the exceptions of ^{74}Se , ^{78}Kr , ^{84}Sr , and ^{180}Ta . The GOSH-like and deeper GOSH-like mixing scenarios have an average OP of 0.47 dex and 0.18 dex, and the partial merger and deeper partial merger mixing scenarios have an average OP of 0.54 dex and 0.31 dex.

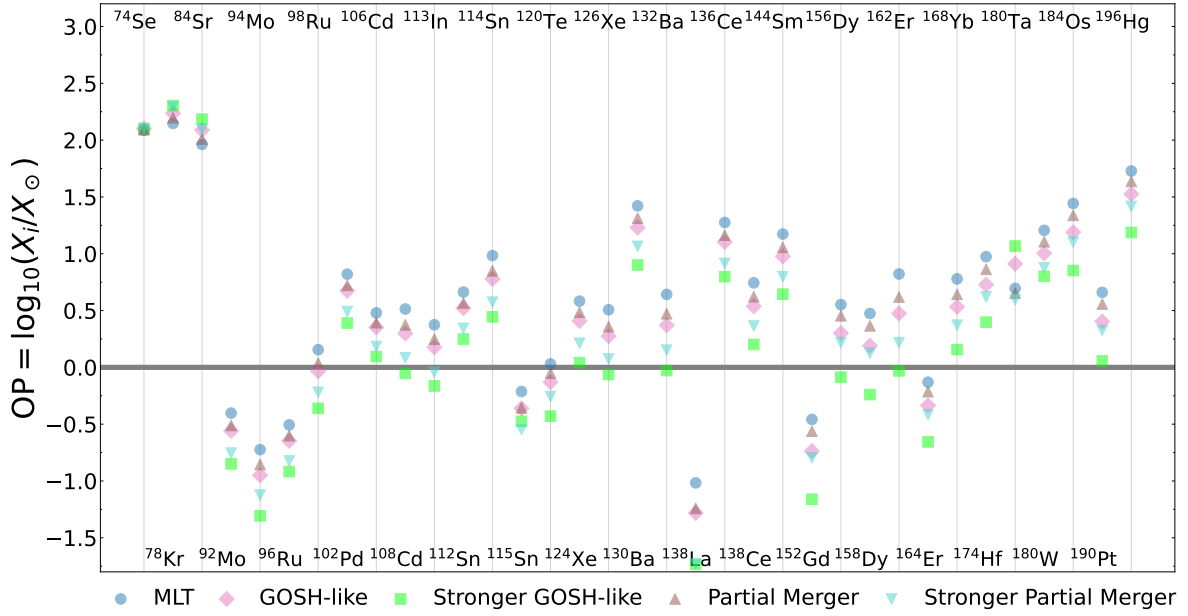


Figure 2.16: The overproduction of all p-nuclei with respect to the solar amount. The blue circle corresponds to the MLT scenario, pink diamond to GOSH-like scenario, lime square to deeper GOSH-like scenario, right side up brown triangle to partial merger scenario, and upside down turquoise triangle to deeper partial merger scenario. The thick grey line at OP = 0 corresponds to the solar measurement. The average spread in production is 0.51 dex.

The three lightest p-nuclei are not produced efficiently in the O-shell as discussed above and are significantly less impacted than by convective downturn as the velocities in the relevant nucleosynthetic region are not as impacted. ^{180}Ta has its production boosted by the introduction of the GOSH-like mixing scenarios compared to the MLT and partial merger

scenarios which have roughly equal production. The other p-nuclei behave nearly uniformly in response to the dip in convective velocities. The dip decreases the production of the p-nuclei compared to the baseline MLT mixing scenario. The partial merger serves as a barrier for the ingested C-shell material to efficiently travel into the region, and the GOSH-like dip interrupts the convective-reactive nature of the environment. This is also the reason why the global production drops for the scenarios with deeper dips. They also show a preference for the location of the dip as production with the partial merger is higher than the GOSH-like scenario. Preventing the movement of species deeper in the O-shell where its hot enough to undergo photo-disintegration directly inhibits its ability to undergo convective-reactive nucleosynthesis and therefore decreases production more than slowly down the flow of seeds. The dip is also why ^{78}Kr and ^{84}Sr show slight increases, as the material that would advect up to colder temperatures are impeded. The pattern of the p-nuclei and ratio between isotopes is also generally preserved across these mixing scenarios. This demonstrates the importance of whether there is a dip in the convective velocities and the location of that dip as it could decrease production.

2.4.5 Nuclear physics impact and mixing dependencies

The timescales of nuclear reactions play a key role in the convective-reactive O-shell and as shown above the relevance of a nuclear reaction depends on the mixing speeds. We present the results of varying the input nuclear physics for the MLT mixing scenario in Figure 2.17 and Table 2.3 and the convective downturn mixing scenarios in Figures 2.18–2.21 and Tables 2.4–2.7.

The MLT scenario shows that most of the p-nuclei are impacted by varying the photo-disintegration rates although the spread is very different depending on the isotope, and the $1\times$ convective downturn scenario already shows a significant change in how varying the nuclear physics impacts the same species. As mixing speeds increase, the spread increases for most isotopes. The average spread in production for the MLT and $1\times$, $3\times$, $10\times$, $50\times$ boosted convective downturn scenarios are 0.56 dex, 0.59 dex, 0.69 dex, 0.76 dex, and 0.79 dex respectively. This demonstrates how the mixing details matter when considering the nuclear physics impact as this is a convective-reactive environment.

The average spread in production increases with mixing speed because the material is able to reach hotter temperatures and the possible nucleosynthetic pathways increase. Species like ^{180}W and ^{196}Hg have a spread that increases with mixing speed. This growth is not linear for all species though as those like ^{74}Se and ^{92}Mo grow with mixing speed except for

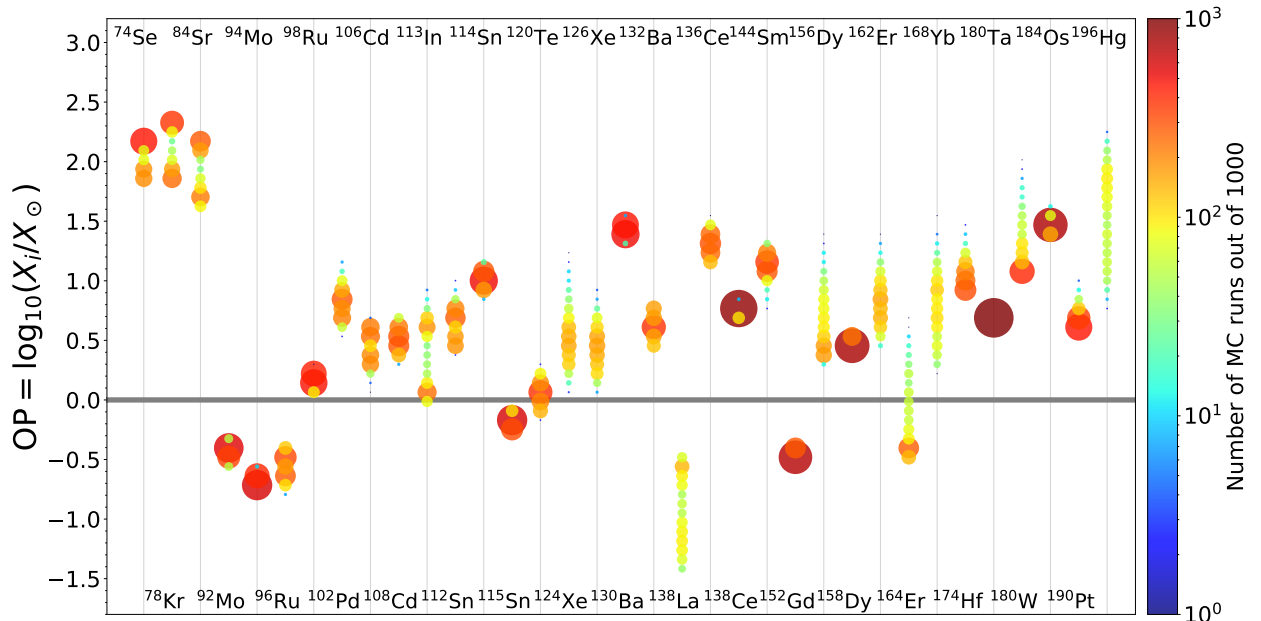


Figure 2.17: Histogram showing the spread due to varying (γ, p) , (γ, n) , (γ, α) and corresponding capture rates for unstable p-heavy isotopes from Se-Po for the MLT mixing scenario. Colour and size correspond to the logarithmic binning of Monte Carlo runs. The thick grey line at $\text{OP} = 0$ corresponds to the solar measurement. The average spread in production is 0.56 dex.

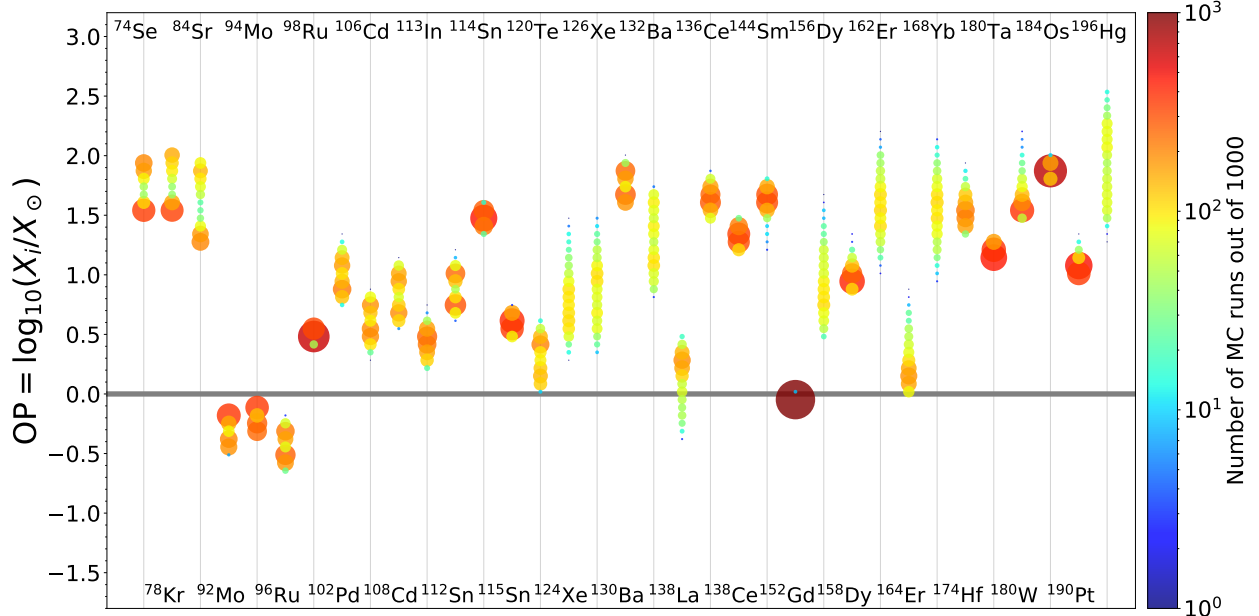


Figure 2.18: Histogram showing the spread due to varying (γ, p) , (γ, n) , (γ, α) and corresponding capture rates for unstable p-heavy isotopes from Se-Po for the 3D-inspired mixing scenario. The thick grey line at $OP = 0$ corresponds to the solar measurement. The average spread in production is 0.59 dex.

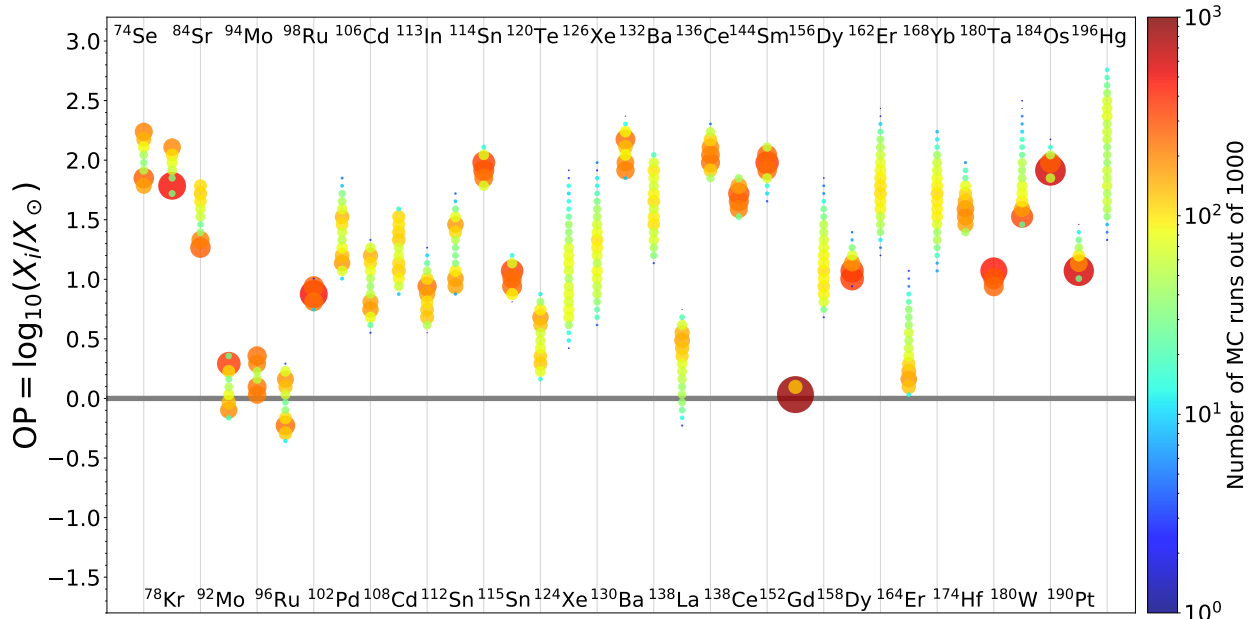


Figure 2.19: Histogram showing the spread due to varying (γ, p) , (γ, n) , (γ, α) and corresponding capture rates for unstable p-heavy isotopes from Se-Po for the 3×3 D-inspired mixing scenario. The thick grey line at $OP = 0$ corresponds to the solar measurement. The average spread in production is 0.69 dex.

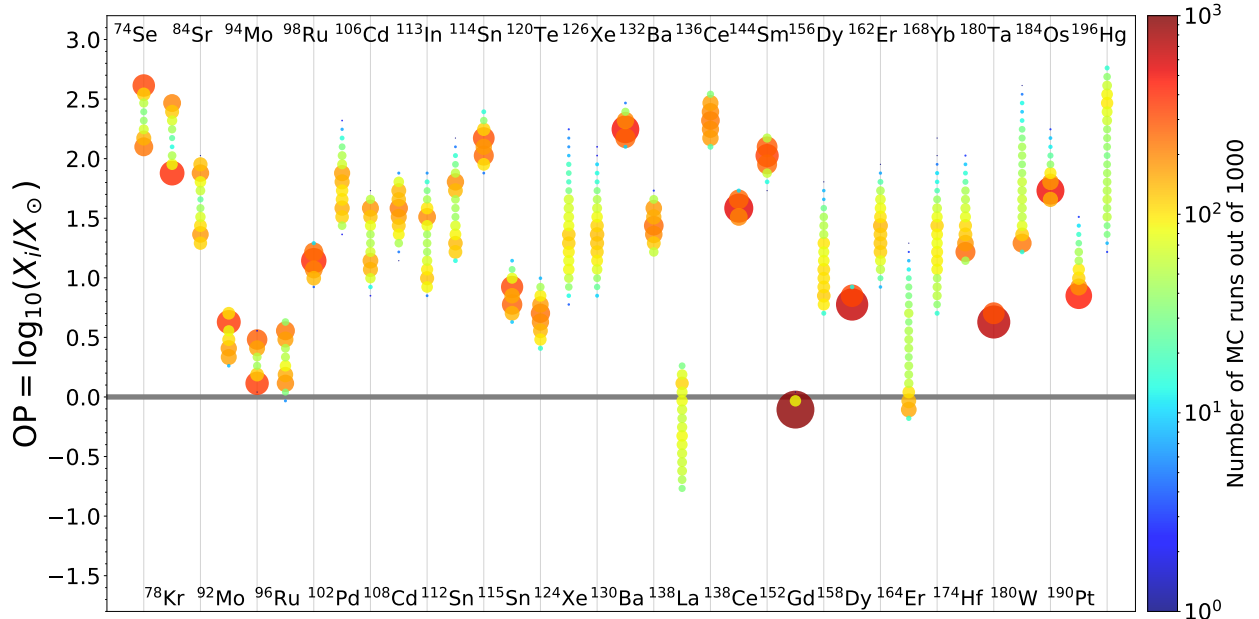


Figure 2.20: Histogram showing the spread due to varying (γ, p) , (γ, n) , (γ, α) and corresponding capture rates for unstable p-heavy isotopes from Se-Po for the 10×3 D-inspired mixing scenario. The thick grey line at $OP = 0$ corresponds to the solar measurement. The average spread in production is 0.76 dex.

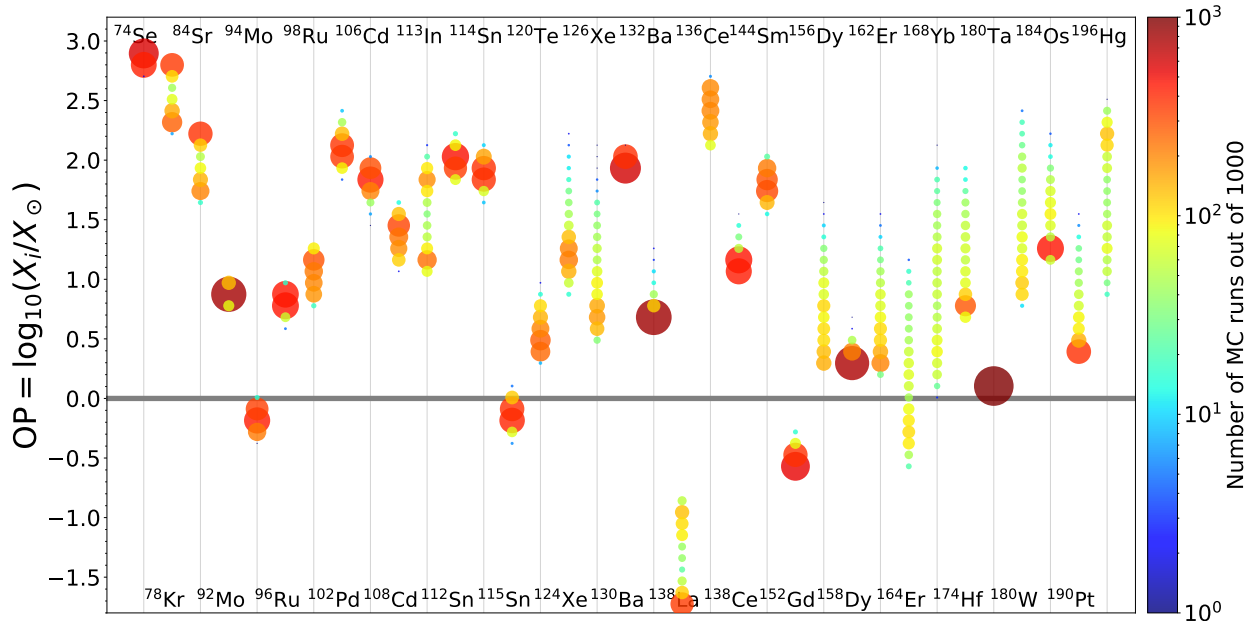


Figure 2.21: Histogram showing the spread due to varying (γ, p) , (γ, n) , (γ, α) and corresponding capture rates for unstable p-heavy isotopes from Se-Po for the 50×3 D-inspired mixing scenario. The thick grey line at $OP = 0$ corresponds to the solar measurement. The average spread in production is 0.79 dex.

the fastest $50\times$ scenario where the spread decreases. There are also impacts on whether the final mass fraction distribution of a species is double peaked and the magnitude of those peaks. ^{96}Ru , ^{113}In , ^{130}Ba , ^{138}La are isotopes where the presence of a double peak in the final mass fraction is dependent on the mixing scenario. ^{74}Se , ^{78}Kr , and ^{84}Sr both have a double peak across the mixing scenarios, but the magnitude of those peaks and whether the higher OP or lower OP peak are favoured is dependent on mixing scenario. This has an implication for using distributions

Considering the reaction rates correlations, whether a particular rate is correlated with the production of a species is completely dependent on the mixing scenario along with the strength of the correlation. Table 2.1 lists those that are unique to a single scenario.

If one wants to propose experiments based on the astrophysical site of an O-C merger, the nuances of the mixing details should be taken into account. For instance, the $50\times 3\text{D}$ -inspired mixing scenario has the largest number of unique reactions as the material is able to advect to the hottest temperatures before reacting, and therefore has a more complex nucleosynthetic pathway. Whether a reaction rate is identified as important and the level of that importance both depend on the whether a convective downturn is present and the speed of mixing.

This is not to say that there aren't shared reactions across the mixing scenarios, as all those that are listed in Table 2.2 are shared across mixing scenario. However, just because these rates are shared does not mean that they are all strongly correlated with the production of the p-nuclei, nor does it mean that they are all impactful in every case. For example, all scenarios have a correlation of $X(^{156}\text{Dy})$ with $^{160}\text{Er}(\gamma, \alpha)$, but in the $50\times 3\text{D}$ -inspired the correlation is much weaker. This underscores the difficulty in using 1-D astrophysical sites to identify important reactions for nuclear physics experiments.

There is a way that nuclear experiments could discriminate mixing scenarios as there are reactions unique to the MLT mixing scenario as listed in Table 2.1 and there are two reaction rates that are correlated in all convective downturns scenarios but not in the MLT case which are $X(^{115}\text{Sn})$ with $^{110}\text{Sn}(\gamma, \alpha)$ and $X(^{138}\text{Ce})$ with $^{138}\text{Nd}(\gamma, p)$.

2.5 Discussion

In this paper, we have shown with detail the importance of accurately modelling the mixing details in the O-burning shell during an O-C shell merger. We have demonstrated the importance of understanding the convective-reactive nature of the nucleosynthesis in the O-shell as material both advects and reacts. We show that γ -process nucleosynthesis is sensitive

Table 2.1: Reactions correlated with the production/destruction of an isotope unique to an individual mixing scenario.

Isotope	Unique Correlated Reaction Rates
MLT Mixing Case	
^{138}Ce	$^{139}\text{Pr}(\gamma, p)$
^{168}Yb	$^{176}\text{W}(\gamma, \alpha)$
^{174}Hf	$^{178}\text{W}(\gamma, n)$
^{184}Os	$^{186}\text{Pt}(\gamma, n)$ $^{188}\text{Pt}(\gamma, n)$
3D-inspired Mixing Case	
^{113}In	$^{114}\text{In}(\gamma, n)$
^{152}Gd	$^{150}\text{Gd}(\gamma, \alpha)$ $^{196}\text{Pb}(\gamma, n)$
^{180}Ta	$^{179}\text{Ta}(\gamma, \alpha)$
3×3D-inspired Mixing Case	
^{180}W	$^{181}\text{Os}(\gamma, n)$
10×3D-inspired Mixing Case	
^{84}Sr	$^{84}\text{Rb}(\gamma, n)$
^{120}Te	$^{119}\text{Te}(\gamma, n)$
^{126}Xe	$^{122}\text{Xe}(\gamma, n)$
^{130}Ba	$^{126}\text{Ba}(\gamma, p)$ $^{128}\text{Ba}(\gamma, \alpha)$ $^{128}\text{Ba}(\gamma, p)$
^{132}Ba	$^{128}\text{Ba}(\gamma, \alpha)$
^{168}Yb	$^{169}\text{Hf}(\gamma, n)$
^{174}Hf	$^{176}\text{W}(\gamma, \alpha)$
^{184}Os	$^{185}\text{Pt}(\gamma, \alpha)$
50×3D-inspired Mixing Case	
^{92}Mo	$^{100}\text{Pd}(\gamma, \alpha)$ $^{100}\text{Pd}(\gamma, p)$ $^{110}\text{Sn}(\gamma, n)$ $^{110}\text{Sn}(\gamma, p)$
^{96}Ru	$^{97}\text{Ru}(\gamma, \alpha)$ $^{110}\text{Sn}(\gamma, \alpha)$ $^{110}\text{Sn}(\gamma, n)$ $^{110}\text{Sn}(\gamma, p)$
^{102}Pd	$^{104}\text{Cd}(\gamma, \alpha)$ $^{104}\text{Cd}(\gamma, p)$
^{106}Cd	$^{104}\text{Cd}(\gamma, p)$ $^{110}\text{Sn}(\gamma, p)$
^{108}Cd	$^{110}\text{Sn}(\gamma, \alpha)$
^{112}Sn	$^{110}\text{Sn}(\gamma, p)$
^{115}Sn	$^{122}\text{Xe}(\gamma, n)$
^{120}Te	$^{120}\text{Xe}(\gamma, \alpha)$
^{126}Xe	$^{127}\text{Ba}(\gamma, n)$
^{130}Ba	$^{132}\text{Ce}(\gamma, \alpha)$ $^{132}\text{Ce}(\gamma, n)$ $^{132}\text{Ce}(\gamma, p)$
	$^{134}\text{Ce}(\gamma, \alpha)$ $^{134}\text{Ce}(\gamma, n)$
^{132}Ba	$^{132}\text{Ce}(\gamma, \alpha)$ $^{132}\text{Ce}(\gamma, n)$ $^{132}\text{Ce}(\gamma, p)$
	$^{133}\text{Ce}(\gamma, n)$ $^{134}\text{Ce}(\gamma, \alpha)$
^{138}Ce	$^{139}\text{Nd}(\gamma, n)$
^{156}Dy	$^{156}\text{Er}(\gamma, \alpha)$ $^{158}\text{Er}(\gamma, \alpha)$ $^{158}\text{Er}(\gamma, n)$
^{162}Er	$^{168}\text{Hf}(\gamma, n)$ $^{162}\text{Yb}(\gamma, \alpha)$ $^{164}\text{Yb}(\gamma, \alpha)$
^{184}Os	$^{184}\text{Pt}(\gamma, n)$

Table 2.2: Reactions correlated with the production/destruction of an isotope shared across all mixing scenarios.

Isotope	Shared Correlated Reaction Rates		
^{74}Se	$^{75}\text{Se}(\gamma, n)$		
^{78}Kr	$^{79}\text{Kr}(\gamma, n)$		
^{84}Sr	$^{85}\text{Sr}(\gamma, n)$		
^{92}Mo	$^{93}\text{Mo}(\gamma, n)$		
^{94}Mo	$^{93}\text{Mo}(\gamma, n)$		
^{96}Ru	$^{97}\text{Ru}(\gamma, n)$		
^{98}Ru	$^{100}\text{Pd}(\gamma, \alpha)$	$^{100}\text{Pd}(\gamma, p)$	
^{102}Pd	$^{100}\text{Pd}(\gamma, \alpha)$	$^{100}\text{Pd}(\gamma, p)$	$^{103}\text{Pd}(\gamma, n)$
^{106}Cd	$^{107}\text{Cd}(\gamma, n)$	$^{110}\text{Sn}(\gamma, \alpha)$	
^{108}Cd	$^{107}\text{Cd}(\gamma, n)$		
^{113}In	$^{113}\text{Sn}(\gamma, n)$		
^{112}Sn	$^{113}\text{Sn}(\gamma, n)$		
^{114}Sn	$^{110}\text{Sn}(\gamma, \alpha)$	$^{113}\text{Sn}(\gamma, n)$	$^{122}\text{Xe}(\gamma, \alpha)$
^{115}Sn	$^{113}\text{Sn}(\gamma, n)$		
^{120}Te	$^{122}\text{Xe}(\gamma, \alpha)$	$^{122}\text{Xe}(\gamma, p)$	
^{124}Xe	$^{122}\text{Xe}(\gamma, \alpha)$	$^{122}\text{Xe}(\gamma, p)$	
^{138}La	$^{137}\text{La}(\gamma, n)$		
^{136}Ce	$^{138}\text{Nd}(\gamma, n)$	$^{138}\text{Nd}(\gamma, p)$	$^{140}\text{Nd}(\gamma, \alpha)$
^{144}Sm	$^{196}\text{Pb}(\gamma, n)$	$^{142}\text{Sm}(\gamma, n)$	$^{142}\text{Sm}(\gamma, p)$
^{152}Gd	$^{152}\text{Dy}(\gamma, \alpha)$		
^{156}Dy	$^{160}\text{Er}(\gamma, \alpha)$		
^{164}Er	$^{164}\text{Yb}(\gamma, \alpha)$	$^{164}\text{Yb}(\gamma, n)$	
^{174}Hf	$^{174}\text{W}(\gamma, \alpha)$		
^{180}Ta	$^{179}\text{Ta}(\gamma, n)$		
^{180}W	$^{180}\text{Os}(\gamma, \alpha)$	$^{180}\text{Os}(\gamma, n)$	$^{196}\text{Pb}(\gamma, n)$
^{184}Os	$^{196}\text{Pb}(\gamma, n)$	$^{184}\text{Pt}(\gamma, \alpha)$	
^{190}Pt	$^{190}\text{Hg}(\gamma, \alpha)$	$^{190}\text{Hg}(\gamma, n)$	$^{196}\text{Pb}(\gamma, n)$
^{196}Hg	$^{196}\text{Pb}(\gamma, n)$	$^{202}\text{Pb}(\gamma, n)$	

Table 2.3: Correlations and ζ slopes between mass fraction and reaction rates for the MLT mixing scenario.

Isotope	Reaction	r_P	ζ	Isotope	Reaction	r_P	ζ
⁷⁴ Se	⁷⁵ Se(γ, n)	-0.93	-0.18	¹⁴⁴ Sm	¹⁴² Sm(γ, n)	-0.19	-0.02
⁷⁸ Kr	⁷⁹ Kr(γ, n)	-0.88	-0.28		¹⁴² Sm(γ, p)	-0.17	-0.02
⁸⁴ Sr	⁸⁵ Sr(γ, n)	-0.88	-0.28		¹⁴³ Sm(γ, n)	-0.25	-0.03
⁹² Mo	⁹³ Mo(γ, n)	-0.94	-0.07		¹⁴⁶ Sm(γ, n)	0.20	0.03
	¹¹⁰ Sn(γ, α)	0.16	0.01		¹⁵⁰ Gd(γ, n)	0.17	0.02
⁹⁴ Mo	⁹³ Mo(γ, n)	0.97	0.06		¹⁵⁰ Gd(γ, α)	-0.15	-0.02
⁹⁶ Ru	⁹⁷ Ru(γ, n)	-0.88	-0.12		¹⁹⁶ Pb(γ, n)	0.47	0.06
	¹⁰⁰ Pd(γ, α)	0.20	0.03		²⁰² Pb(γ, n)	0.21	0.03
⁹⁸ Ru	⁹⁷ Ru(γ, n)	0.36	0.02	¹⁵² Gd	¹⁵² Dy(γ, α)	-0.40	-0.01
	¹⁰⁰ Pd(γ, p)	0.62	0.04		¹⁵⁴ Dy(γ, α)	-0.15	-0.00
	¹⁰⁰ Pd(γ, α)	-0.51	-0.03		¹⁶⁰ Er(γ, α)	0.39	0.00
¹⁰² Pd	¹⁰⁰ Pd(γ, p)	-0.29	-0.05	¹⁵⁶ Dy	¹⁵⁹ Er(γ, n)	-0.18	-0.06
	¹⁰⁰ Pd(γ, α)	-0.30	-0.05		¹⁶⁰ Er(γ, α)	0.74	0.26
	¹⁰³ Pd(γ, n)	-0.66	-0.12		²⁰² Pb(γ, n)	0.18	0.05
¹⁰⁶ Cd	¹⁰⁷ Cd(γ, n)	-0.86	-0.16	¹⁵⁸ Dy	¹⁵⁸ Er(γ, α)	-0.23	-0.01
	¹¹⁰ Sn(γ, α)	0.23	0.05		¹⁶⁰ Er(γ, α)	0.56	0.01
¹⁰⁸ Cd	¹⁰⁷ Cd(γ, n)	0.72	0.10		¹⁹⁶ Pb(γ, n)	0.16	0.00
	¹⁰⁹ Cd(γ, n)	-0.46	-0.06	¹⁶² Er	²⁰² Pb(γ, n)	0.18	0.00
	¹¹⁰ Sn(γ, p)	0.16	0.02		¹⁵⁹ Er(γ, n)	-0.18	-0.06
¹¹³ In	¹¹³ Sn(γ, n)	0.91	0.37		¹⁶⁰ Er(γ, n)	-0.18	-0.06
¹¹² Sn	¹¹⁰ Sn(γ, α)	-0.17	-0.03		¹⁶⁰ Er(γ, α)	-0.26	-0.07
	¹¹³ Sn(γ, n)	-0.83	-0.15		¹⁶¹ Er(γ, n)	0.21	0.06
¹¹⁴ Sn	¹¹⁰ Sn(γ, α)	-0.15	-0.01		¹⁶⁶ Yb(γ, α)	0.53	0.14
	¹¹³ Sn(γ, n)	0.74	0.06		¹⁹⁶ Pb(γ, n)	0.25	0.07
	¹²² Xe(γ, n)	-0.18	-0.01		²⁰² Pb(γ, n)	0.17	0.05
	¹²² Xe(γ, p)	0.20	0.02	¹⁶⁴ Er	¹⁶⁴ Yb(γ, n)	-0.24	-0.09
	¹²² Xe(γ, α)	0.41	0.04		¹⁶⁴ Yb(γ, α)	-0.58	-0.32
¹¹⁵ Sn	¹¹³ Sn(γ, n)	0.80	0.05		¹⁹⁶ Pb(γ, n)	0.17	0.05
	¹²² Xe(γ, p)	0.17	0.01	¹⁶⁸ Yb	¹⁶⁸ Hf(γ, α)	-0.28	-0.14
	¹²² Xe(γ, α)	0.35	0.02		¹⁷² Hf(γ, α)	0.60	0.24
¹²⁰ Te	¹²¹ Te(γ, n)	-0.71	-0.09		¹⁷⁶ W(γ, α)	0.20	0.07
	¹²² Xe(γ, p)	0.45	0.05		¹⁹⁶ Pb(γ, n)	0.21	0.07
	¹²² Xe(γ, α)	-0.32	-0.04	¹⁷⁴ Hf	¹⁷⁴ W(γ, n)	-0.21	-0.03
¹²⁴ Xe	¹²² Xe(γ, n)	-0.17	-0.04		¹⁷⁴ W(γ, α)	-0.40	-0.08
	¹²² Xe(γ, p)	-0.24	-0.06		¹⁷⁸ W(γ, n)	-0.15	-0.03
	¹²² Xe(γ, α)	-0.45	-0.15		¹⁷⁸ W(γ, α)	0.42	0.07
	¹²³ Xe(γ, n)	0.16	0.03	¹⁸⁰ Ta	¹⁷⁹ Ta(γ, n)	-0.91	-0.02
	¹²⁵ Xe(γ, n)	-0.46	-0.16	¹⁸⁰ W	¹⁸⁰ Os(γ, n)	-0.28	-0.07
¹²⁶ Xe	¹²² Xe(γ, α)	-0.34	-0.09		¹⁸⁰ Os(γ, α)	-0.52	-0.21
	¹²⁵ Xe(γ, n)	0.49	0.13		¹⁹⁶ Pb(γ, n)	0.21	0.05
	¹²⁷ Xe(γ, n)	-0.25	-0.07	¹⁸⁴ Os	¹⁸⁵ Os(γ, n)	0.33	0.02
	¹²⁶ Ba(γ, p)	-0.18	-0.04		¹⁸⁴ Pt(γ, α)	-0.44	-0.03
	¹²⁶ Ba(γ, α)	-0.32	-0.09		¹⁸⁶ Pt(γ, n)	0.17	0.01
¹³⁰ Ba	¹²⁶ Ba(γ, α)	-0.17	-0.01		¹⁸⁶ Pt(γ, α)	-0.16	-0.01
	¹²⁸ Ba(γ, n)	-0.19	-0.01		¹⁸⁸ Pt(γ, n)	-0.17	-0.01
	¹²⁹ Ba(γ, n)	0.23	0.01		¹⁹⁶ Pb(γ, n)	0.16	0.01
	¹³¹ Ba(γ, n)	-0.79	-0.05	¹⁹⁰ Pt	¹⁹⁰ Hg(γ, n)	-0.28	-0.03
¹³² Ba	¹³¹ Ba(γ, n)	0.66	0.09		¹⁹⁰ Hg(γ, α)	-0.51	-0.06
	¹³³ Ba(γ, n)	-0.61	-0.08		¹⁹⁶ Pb(γ, n)	0.20	0.02
¹³⁸ La	¹³⁷ La(γ, n)	-0.71	-0.37	¹⁹⁶ Hg	¹⁹⁶ Pb(γ, n)	-0.71	-0.41
¹³⁶ Ce	¹³⁸ Nd(γ, n)	-0.38	-0.05		¹⁹⁷ Pb(γ, n)	-0.16	-0.06
	¹³⁸ Nd(γ, p)	0.65	0.08		²⁰⁰ Pb(γ, n)	0.19	0.10
	¹³⁸ Nd(γ, α)	-0.16	-0.02		²⁰² Pb(γ, n)	0.30	0.14
	¹⁴⁰ Nd(γ, α)	0.34	0.04				
¹³⁸ Ce	¹³⁷ Ce(γ, n)	0.51	0.02				
	¹³⁹ Ce(γ, n)	-0.43	-0.01				
	¹³⁹ Pr(γ, p)	0.29	0.01				
	¹³⁸ Nd(γ, n)	-0.30	-0.01				
	¹³⁸ Nd(γ, α)	-0.22	-0.01				

Table 2.4: Correlations and ζ slopes between mass fraction and reaction rates for the 3D-inspired mixing scenario.

Isotope	Reaction	r_P	ζ	Isotope	Reaction	r_P	ζ
^{74}Se	$^{75}\text{Se}(\gamma, n)$	-0.83	-0.22	^{152}Gd	$^{150}\text{Gd}(\gamma, \alpha)$	-0.18	-0.00
^{78}Kr	$^{79}\text{Kr}(\gamma, n)$	-0.79	-0.24		$^{151}\text{Gd}(\gamma, n)$	-0.20	-0.00
^{84}Sr	$^{85}\text{Sr}(\gamma, n)$	-0.80	-0.34		$^{152}\text{Dy}(\gamma, \alpha)$	-0.31	-0.01
^{92}Mo	$^{93}\text{Mo}(\gamma, n)$	-0.91	-0.14		$^{154}\text{Dy}(\gamma, \alpha)$	-0.17	-0.00
^{94}Mo	$^{93}\text{Mo}(\gamma, n)$	0.93	0.10		$^{160}\text{Er}(\gamma, \alpha)$	0.39	0.01
^{96}Ru	$^{97}\text{Ru}(\gamma, n)$	-0.82	-0.14		$^{196}\text{Pb}(\gamma, n)$	0.16	0.00
	$^{100}\text{Pd}(\gamma, \alpha)$	0.21	0.04	^{156}Dy	$^{157}\text{Dy}(\gamma, n)$	-0.28	-0.12
^{98}Ru	$^{97}\text{Ru}(\gamma, n)$	0.50	0.02		$^{159}\text{Er}(\gamma, n)$	-0.17	-0.05
	$^{100}\text{Pd}(\gamma, p)$	0.58	0.03		$^{160}\text{Er}(\gamma, \alpha)$	0.68	0.26
	$^{100}\text{Pd}(\gamma, \alpha)$	-0.31	-0.01		$^{196}\text{Pb}(\gamma, n)$	0.16	0.05
^{102}Pd	$^{110}\text{Sn}(\gamma, \alpha)$	0.22	0.01	^{158}Dy	$^{157}\text{Dy}(\gamma, n)$	0.24	0.03
	$^{100}\text{Pd}(\gamma, p)$	-0.18	-0.04		$^{159}\text{Dy}(\gamma, n)$	-0.21	-0.03
	$^{100}\text{Pd}(\gamma, \alpha)$	-0.21	-0.04		$^{159}\text{Er}(\gamma, n)$	-0.17	-0.02
	$^{103}\text{Pd}(\gamma, n)$	-0.72	-0.16		$^{160}\text{Er}(\gamma, \alpha)$	0.66	0.07
^{106}Cd	$^{107}\text{Cd}(\gamma, n)$	-0.75	-0.16		$^{196}\text{Pb}(\gamma, n)$	0.16	0.02
	$^{110}\text{Sn}(\gamma, \alpha)$	0.31	0.07		$^{202}\text{Pb}(\gamma, n)$	0.20	0.02
^{108}Cd	$^{107}\text{Cd}(\gamma, n)$	0.20	0.05	^{162}Er	$^{159}\text{Er}(\gamma, n)$	-0.25	-0.10
	$^{109}\text{Cd}(\gamma, n)$	-0.83	-0.20		$^{159}\text{Er}(\gamma, \alpha)$	-0.16	-0.05
^{113}In	$^{114}\text{In}(\gamma, n)$	-0.32	-0.05		$^{160}\text{Er}(\gamma, n)$	-0.23	-0.09
	$^{110}\text{Sn}(\gamma, p)$	-0.16	-0.02		$^{160}\text{Er}(\gamma, \alpha)$	-0.44	-0.15
	$^{110}\text{Sn}(\gamma, \alpha)$	-0.27	-0.04		$^{161}\text{Er}(\gamma, n)$	0.16	0.06
	$^{113}\text{Sn}(\gamma, n)$	0.60	0.10		$^{166}\text{Yb}(\gamma, \alpha)$	0.33	0.11
	$^{169}\text{Lu}(\gamma, n)$	0.15	0.02		$^{196}\text{Pb}(\gamma, n)$	0.27	0.10
^{112}Sn	$^{113}\text{Sn}(\gamma, n)$	-0.80	-0.18		$^{202}\text{Pb}(\gamma, n)$	0.16	0.06
^{114}Sn	$^{110}\text{Sn}(\gamma, \alpha)$	-0.17	-0.01	^{164}Er	$^{164}\text{Yb}(\gamma, n)$	-0.26	-0.07
	$^{113}\text{Sn}(\gamma, n)$	0.65	0.05		$^{164}\text{Yb}(\gamma, \alpha)$	-0.56	-0.18
	$^{122}\text{Xe}(\gamma, p)$	0.21	0.02		$^{196}\text{Pb}(\gamma, n)$	0.21	0.06
	$^{122}\text{Xe}(\gamma, \alpha)$	0.44	0.03		$^{202}\text{Pb}(\gamma, n)$	0.18	0.05
^{115}Sn	$^{110}\text{Sn}(\gamma, \alpha)$	-0.16	-0.01	^{168}Yb	$^{164}\text{Yb}(\gamma, \alpha)$	-0.19	-0.09
	$^{113}\text{Sn}(\gamma, n)$	0.74	0.06		$^{166}\text{Yb}(\gamma, n)$	-0.22	-0.08
	$^{122}\text{Xe}(\gamma, p)$	0.16	0.01		$^{166}\text{Yb}(\gamma, \alpha)$	-0.38	-0.13
	$^{122}\text{Xe}(\gamma, \alpha)$	0.33	0.03		$^{167}\text{Yb}(\gamma, n)$	0.20	0.07
^{120}Te	$^{121}\text{Te}(\gamma, n)$	-0.76	-0.19		$^{172}\text{Hf}(\gamma, \alpha)$	0.43	0.16
	$^{122}\text{Xe}(\gamma, p)$	0.26	0.05		$^{196}\text{Pb}(\gamma, n)$	0.28	0.09
	$^{122}\text{Xe}(\gamma, \alpha)$	-0.23	-0.05		$^{202}\text{Pb}(\gamma, n)$	0.19	0.06
^{124}Xe	$^{122}\text{Xe}(\gamma, p)$	-0.19	-0.05	^{174}Hf	$^{172}\text{Hf}(\gamma, \alpha)$	-0.40	-0.07
	$^{122}\text{Xe}(\gamma, \alpha)$	-0.39	-0.15		$^{174}\text{W}(\gamma, \alpha)$	-0.19	-0.04
	$^{125}\text{Xe}(\gamma, n)$	-0.54	-0.23		$^{178}\text{W}(\gamma, \alpha)$	0.51	0.09
^{126}Xe	$^{122}\text{Xe}(\gamma, \alpha)$	-0.35	-0.14		$^{182}\text{Os}(\gamma, \alpha)$	0.18	0.03
	$^{125}\text{Xe}(\gamma, n)$	0.22	0.09		$^{196}\text{Pb}(\gamma, n)$	0.19	0.03
	$^{127}\text{Xe}(\gamma, n)$	-0.63	-0.27	^{180}Ta	$^{179}\text{Ta}(\gamma, n)$	-0.91	-0.07
^{130}Ba	$^{131}\text{Ba}(\gamma, n)$	-0.82	-0.13		$^{179}\text{Ta}(\gamma, \alpha)$	-0.15	-0.01
^{132}Ba	$^{131}\text{Ba}(\gamma, n)$	0.36	0.14	^{180}W	$^{180}\text{Os}(\gamma, n)$	-0.27	-0.05
	$^{133}\text{Ba}(\gamma, n)$	-0.76	-0.30		$^{180}\text{Os}(\gamma, \alpha)$	-0.51	-0.13
^{138}La	$^{133}\text{La}(\gamma, p)$	-0.20	-0.07		$^{196}\text{Pb}(\gamma, n)$	0.23	0.04
	$^{135}\text{La}(\gamma, n)$	-0.35	-0.12	^{184}Os	$^{182}\text{Os}(\gamma, \alpha)$	-0.38	-0.02
	$^{136}\text{La}(\gamma, n)$	0.26	0.08		$^{184}\text{Pt}(\gamma, \alpha)$	-0.33	-0.02
	$^{137}\text{La}(\gamma, n)$	-0.34	-0.14		$^{186}\text{Pt}(\gamma, \alpha)$	-0.15	-0.01
^{136}Ce	$^{137}\text{Ce}(\gamma, n)$	-0.49	-0.07		$^{188}\text{Pt}(\gamma, \alpha)$	0.23	0.01
	$^{138}\text{Nd}(\gamma, n)$	-0.27	-0.03		$^{196}\text{Pb}(\gamma, n)$	0.19	0.01
	$^{138}\text{Nd}(\gamma, p)$	0.48	0.06	^{190}Pt	$^{190}\text{Hg}(\gamma, n)$	-0.30	-0.02
	$^{140}\text{Nd}(\gamma, \alpha)$	0.38	0.04		$^{190}\text{Hg}(\gamma, \alpha)$	-0.50	-0.05
^{138}Ce	$^{137}\text{Ce}(\gamma, n)$	0.65	0.07		$^{196}\text{Pb}(\gamma, n)$	0.20	0.02
	$^{139}\text{Ce}(\gamma, n)$	-0.52	-0.05		$^{196}\text{Pb}(\gamma, n)$	-0.68	-0.35
	$^{138}\text{Nd}(\gamma, p)$	0.16	0.01	^{196}Hg	$^{197}\text{Pb}(\gamma, n)$	-0.26	-0.10
^{144}Sm	$^{142}\text{Sm}(\gamma, n)$	-0.15	-0.02		$^{200}\text{Pb}(\gamma, n)$	0.17	0.07
	$^{142}\text{Sm}(\gamma, p)$	-0.16	-0.02		$^{202}\text{Pb}(\gamma, n)$	0.24	0.10
	$^{143}\text{Sm}(\gamma, n)$	-0.19	-0.03				
	$^{146}\text{Sm}(\gamma, n)$	0.19	0.03				
	$^{146}\text{Sm}(\gamma, \alpha)$	-0.22	-0.03				
	$^{150}\text{Gd}(\gamma, n)$	0.21	0.03				
	$^{150}\text{Gd}(\gamma, \alpha)$	-0.20	-0.03				
	$^{196}\text{Pb}(\gamma, n)$	0.46	0.06				
	$^{202}\text{Pb}(\gamma, n)$	0.20	0.03				

Table 2.5: Correlations and ζ slopes between mass fraction and reaction rates for the 3×3 D-inspired mixing scenario.

Isotope	Reaction	r_P	ζ	Isotope	Reaction	r_P	ζ
^{74}Se	$^{75}\text{Se}(\gamma, n)$	-0.81	-0.24	^{144}Sm	$^{142}\text{Sm}(\gamma, n)$	-0.23	-0.02
^{78}Kr	$^{79}\text{Kr}(\gamma, n)$	-0.76	-0.20		$^{142}\text{Sm}(\gamma, p)$	-0.23	-0.03
^{84}Sr	$^{85}\text{Sr}(\gamma, n)$	-0.75	-0.26		$^{143}\text{Sm}(\gamma, n)$	-0.30	-0.04
^{92}Mo	$^{93}\text{Mo}(\gamma, n)$	-0.91	-0.23		$^{146}\text{Sm}(\gamma, \alpha)$	-0.17	-0.02
^{94}Mo	$^{93}\text{Mo}(\gamma, n)$	0.92	0.17		$^{150}\text{Gd}(\gamma, n)$	0.17	0.02
^{96}Ru	$^{97}\text{Ru}(\gamma, n)$	-0.84	-0.25		$^{150}\text{Gd}(\gamma, \alpha)$	-0.16	-0.02
^{98}Ru	$^{97}\text{Ru}(\gamma, n)$	0.65	0.05		$^{196}\text{Pb}(\gamma, n)$	0.44	0.05
	$^{100}\text{Pd}(\gamma, p)$	0.47	0.03		$^{202}\text{Pb}(\gamma, n)$	0.17	0.02
	$^{100}\text{Pd}(\gamma, \alpha)$	-0.23	-0.02	^{152}Gd	$^{151}\text{Gd}(\gamma, n)$	-0.17	-0.00
	$^{110}\text{Sn}(\gamma, \alpha)$	0.21	0.01		$^{152}\text{Dy}(\gamma, \alpha)$	-0.39	-0.01
^{102}Pd	$^{100}\text{Pd}(\gamma, p)$	-0.20	-0.06		$^{154}\text{Dy}(\gamma, \alpha)$	-0.19	-0.00
	$^{100}\text{Pd}(\gamma, \alpha)$	-0.22	-0.06		$^{160}\text{Er}(\gamma, \alpha)$	0.33	0.01
	$^{103}\text{Pd}(\gamma, n)$	-0.71	-0.26	^{156}Dy	$^{157}\text{Dy}(\gamma, n)$	-0.21	-0.08
^{106}Cd	$^{107}\text{Cd}(\gamma, n)$	-0.78	-0.27		$^{159}\text{Er}(\gamma, n)$	-0.18	-0.06
	$^{110}\text{Sn}(\gamma, \alpha)$	0.21	0.08		$^{160}\text{Er}(\gamma, \alpha)$	0.69	0.25
^{108}Cd	$^{107}\text{Cd}(\gamma, n)$	0.24	0.08		$^{196}\text{Pb}(\gamma, n)$	0.15	0.05
	$^{109}\text{Cd}(\gamma, n)$	-0.80	-0.24		$^{202}\text{Pb}(\gamma, n)$	0.15	0.05
^{113}In	$^{110}\text{Sn}(\gamma, p)$	-0.22	-0.04	^{158}Dy	$^{157}\text{Dy}(\gamma, n)$	0.20	0.02
	$^{110}\text{Sn}(\gamma, \alpha)$	-0.33	-0.06		$^{159}\text{Er}(\gamma, n)$	-0.19	-0.02
	$^{113}\text{Sn}(\gamma, n)$	0.62	0.15		$^{160}\text{Er}(\gamma, \alpha)$	0.67	0.07
	$^{169}\text{Lu}(\gamma, n)$	0.16	0.03		$^{196}\text{Pb}(\gamma, n)$	0.16	0.02
^{112}Sn	$^{113}\text{Sn}(\gamma, n)$	-0.78	-0.31		$^{202}\text{Pb}(\gamma, n)$	0.20	0.02
^{114}Sn	$^{110}\text{Sn}(\gamma, p)$	-0.17	-0.02	^{162}Er	$^{159}\text{Er}(\gamma, n)$	-0.29	-0.12
	$^{110}\text{Sn}(\gamma, \alpha)$	-0.26	-0.03		$^{159}\text{Er}(\gamma, \alpha)$	-0.17	-0.05
	$^{113}\text{Sn}(\gamma, n)$	0.70	0.08		$^{160}\text{Er}(\gamma, n)$	-0.22	-0.09
	$^{122}\text{Xe}(\gamma, p)$	0.16	0.02		$^{160}\text{Er}(\gamma, \alpha)$	-0.40	-0.13
	$^{122}\text{Xe}(\gamma, \alpha)$	0.27	0.03		$^{161}\text{Er}(\gamma, n)$	0.18	0.08
	$^{169}\text{Lu}(\gamma, n)$	0.15	0.01		$^{166}\text{Yb}(\gamma, \alpha)$	0.32	0.11
^{115}Sn	$^{110}\text{Sn}(\gamma, p)$	-0.17	-0.02		$^{196}\text{Pb}(\gamma, n)$	0.27	0.10
	$^{110}\text{Sn}(\gamma, \alpha)$	-0.25	-0.03		$^{202}\text{Pb}(\gamma, n)$	0.15	0.06
	$^{113}\text{Sn}(\gamma, n)$	0.73	0.08	^{164}Er	$^{164}\text{Yb}(\gamma, n)$	-0.24	-0.08
	$^{122}\text{Xe}(\gamma, \alpha)$	0.24	0.03		$^{164}\text{Yb}(\gamma, \alpha)$	-0.56	-0.24
	$^{169}\text{Lu}(\gamma, n)$	0.15	0.01		$^{165}\text{Yb}(\gamma, n)$	-0.17	-0.06
	$^{121}\text{Te}(\gamma, n)$	-0.78	-0.24		$^{196}\text{Pb}(\gamma, n)$	0.19	0.06
^{120}Te	$^{122}\text{Xe}(\gamma, p)$	0.24	0.06		$^{202}\text{Pb}(\gamma, n)$	0.15	0.06
	$^{122}\text{Xe}(\gamma, \alpha)$	-0.22	-0.06	^{168}Yb	$^{164}\text{Yb}(\gamma, \alpha)$	-0.22	-0.10
^{124}Xe	$^{122}\text{Xe}(\gamma, p)$	-0.20	-0.07		$^{166}\text{Yb}(\gamma, n)$	-0.18	-0.07
	$^{122}\text{Xe}(\gamma, \alpha)$	-0.36	-0.18		$^{166}\text{Yb}(\gamma, \alpha)$	-0.34	-0.12
	$^{125}\text{Xe}(\gamma, n)$	-0.54	-0.33		$^{167}\text{Yb}(\gamma, n)$	0.19	0.07
^{126}Xe	$^{122}\text{Xe}(\gamma, p)$	-0.19	-0.07		$^{172}\text{Hf}(\gamma, \alpha)$	0.43	0.16
	$^{122}\text{Xe}(\gamma, \alpha)$	-0.39	-0.18		$^{196}\text{Pb}(\gamma, n)$	0.29	0.10
	$^{125}\text{Xe}(\gamma, n)$	0.22	0.11		$^{202}\text{Pb}(\gamma, n)$	0.19	0.06
	$^{127}\text{Xe}(\gamma, n)$	-0.57	-0.29	^{174}Hf	$^{172}\text{Hf}(\gamma, \alpha)$	-0.31	-0.06
^{130}Ba	$^{126}\text{Ba}(\gamma, \alpha)$	-0.16	-0.02		$^{174}\text{W}(\gamma, n)$	-0.19	-0.03
	$^{131}\text{Ba}(\gamma, n)$	-0.81	-0.15		$^{174}\text{W}(\gamma, \alpha)$	-0.30	-0.07
^{132}Ba	$^{131}\text{Ba}(\gamma, n)$	0.41	0.15		$^{178}\text{W}(\gamma, \alpha)$	0.46	0.08
	$^{133}\text{Ba}(\gamma, n)$	-0.74	-0.27		$^{182}\text{Os}(\gamma, \alpha)$	0.17	0.03
^{138}La	$^{133}\text{La}(\gamma, p)$	-0.19	-0.08		$^{196}\text{Pb}(\gamma, n)$	0.20	0.04
	$^{135}\text{La}(\gamma, n)$	-0.31	-0.12	^{180}Ta	$^{179}\text{Ta}(\gamma, n)$	-0.89	-0.07
	$^{136}\text{La}(\gamma, n)$	0.25	0.08	^{180}W	$^{180}\text{Os}(\gamma, n)$	-0.26	-0.08
	$^{137}\text{La}(\gamma, n)$	-0.35	-0.16		$^{180}\text{Os}(\gamma, \alpha)$	-0.50	-0.21
^{136}Ce	$^{137}\text{Ce}(\gamma, n)$	-0.47	-0.07		$^{181}\text{Os}(\gamma, n)$	-0.16	-0.04
	$^{138}\text{Nd}(\gamma, n)$	-0.31	-0.04		$^{196}\text{Pb}(\gamma, n)$	0.22	0.06
	$^{138}\text{Nd}(\gamma, p)$	0.52	0.07	^{184}Os	$^{182}\text{Os}(\gamma, \alpha)$	-0.19	-0.02
	$^{140}\text{Nd}(\gamma, \alpha)$	0.32	0.04		$^{185}\text{Os}(\gamma, n)$	0.17	0.01
^{138}Ce	$^{137}\text{Ce}(\gamma, n)$	0.66	0.08		$^{184}\text{Pt}(\gamma, \alpha)$	-0.45	-0.04
	$^{139}\text{Ce}(\gamma, n)$	-0.37	-0.04		$^{186}\text{Pt}(\gamma, \alpha)$	-0.16	-0.01
	$^{138}\text{Nd}(\gamma, n)$	-0.16	-0.02		$^{188}\text{Pt}(\gamma, \alpha)$	0.16	0.01
	$^{138}\text{Nd}(\gamma, p)$	0.28	0.03		$^{196}\text{Pb}(\gamma, n)$	0.20	0.01
	$^{140}\text{Nd}(\gamma, \alpha)$	0.18	0.02	^{190}Pt	$^{190}\text{Hg}(\gamma, n)$	-0.30	-0.04
					$^{190}\text{Hg}(\gamma, \alpha)$	-0.51	-0.07
				^{196}Hg	$^{196}\text{Pb}(\gamma, n)$	0.19	0.02
					$^{196}\text{Pb}(\gamma, n)$	-0.68	-0.42
					$^{197}\text{Pb}(\gamma, n)$	-0.28	-0.13
					$^{202}\text{Pb}(\gamma, n)$	0.20	0.10

Table 2.6: Correlations and ζ slopes between mass fraction and reaction rates for the $10 \times 3D$ -inspired mixing scenario.

Isotope	Reaction	r_P	ζ	Isotope	Reaction	r_P	ζ
^{74}Se	$^{75}\text{Se}(\gamma, n)$	-0.87	-0.30	^{138}Ce	$^{137}\text{Ce}(\gamma, n)$	0.58	0.05
^{78}Kr	$^{79}\text{Kr}(\gamma, n)$	-0.81	-0.35		$^{139}\text{Ce}(\gamma, n)$	-0.19	-0.01
^{84}Sr	$^{84}\text{Rb}(\gamma, n)$	0.16	0.06		$^{138}\text{Nd}(\gamma, n)$	-0.31	-0.02
	$^{85}\text{Sr}(\gamma, n)$	-0.81	-0.33		$^{138}\text{Nd}(\gamma, p)$	0.37	0.03
^{92}Mo	$^{93}\text{Mo}(\gamma, n)$	-0.93	-0.17		$^{138}\text{Nd}(\gamma, \alpha)$	-0.17	-0.01
^{94}Mo	$^{93}\text{Mo}(\gamma, n)$	0.94	0.21		$^{140}\text{Nd}(\gamma, \alpha)$	0.20	0.01
^{96}Ru	$^{97}\text{Ru}(\gamma, n)$	-0.88	-0.25	^{144}Sm	$^{142}\text{Sm}(\gamma, n)$	-0.31	-0.04
^{98}Ru	$^{97}\text{Ru}(\gamma, n)$	0.68	0.07		$^{142}\text{Sm}(\gamma, p)$	-0.29	-0.03
	$^{100}\text{Pd}(\gamma, p)$	0.45	0.05		$^{143}\text{Sm}(\gamma, n)$	-0.41	-0.05
	$^{100}\text{Pd}(\gamma, \alpha)$	-0.29	-0.03		$^{196}\text{Pb}(\gamma, n)$	0.35	0.04
	$^{110}\text{Sn}(\gamma, \alpha)$	0.18	0.02	^{152}Gd	$^{152}\text{Dy}(\gamma, \alpha)$	-0.50	-0.02
^{102}Pd	$^{100}\text{Pd}(\gamma, p)$	-0.29	-0.08		$^{154}\text{Dy}(\gamma, \alpha)$	-0.16	-0.00
	$^{100}\text{Pd}(\gamma, \alpha)$	-0.30	-0.08		$^{158}\text{Er}(\gamma, n)$	0.15	0.00
	$^{103}\text{Pd}(\gamma, n)$	-0.65	-0.21		$^{160}\text{Er}(\gamma, \alpha)$	0.19	0.00
^{106}Cd	$^{107}\text{Cd}(\gamma, n)$	-0.83	-0.30	^{156}Dy	$^{159}\text{Er}(\gamma, n)$	-0.19	-0.06
	$^{110}\text{Sn}(\gamma, \alpha)$	0.19	0.07		$^{160}\text{Er}(\gamma, \alpha)$	0.70	0.26
^{108}Cd	$^{107}\text{Cd}(\gamma, n)$	0.63	0.15		$^{202}\text{Pb}(\gamma, n)$	0.16	0.05
	$^{109}\text{Cd}(\gamma, n)$	-0.50	-0.10	^{158}Dy	$^{159}\text{Dy}(\gamma, n)$	0.19	0.01
^{113}In	$^{110}\text{Sn}(\gamma, p)$	-0.17	-0.05		$^{158}\text{Er}(\gamma, n)$	-0.16	-0.01
	$^{110}\text{Sn}(\gamma, \alpha)$	-0.24	-0.08		$^{158}\text{Er}(\gamma, \alpha)$	-0.28	-0.01
	$^{113}\text{Sn}(\gamma, n)$	0.82	0.34		$^{159}\text{Er}(\gamma, n)$	-0.18	-0.01
^{112}Sn	$^{110}\text{Sn}(\gamma, \alpha)$	-0.17	-0.05		$^{160}\text{Er}(\gamma, \alpha)$	0.56	0.02
	$^{113}\text{Sn}(\gamma, n)$	-0.78	-0.33		$^{196}\text{Pb}(\gamma, n)$	0.17	0.01
^{114}Sn	$^{110}\text{Sn}(\gamma, p)$	-0.18	-0.02		$^{202}\text{Pb}(\gamma, n)$	0.17	0.01
	$^{110}\text{Sn}(\gamma, \alpha)$	-0.27	-0.04	^{162}Er	$^{159}\text{Er}(\gamma, n)$	-0.28	-0.10
	$^{113}\text{Sn}(\gamma, n)$	0.76	0.12		$^{159}\text{Er}(\gamma, \alpha)$	-0.16	-0.05
	$^{122}\text{Xe}(\gamma, \alpha)$	0.15	0.03		$^{160}\text{Er}(\gamma, n)$	-0.19	-0.07
	$^{169}\text{Lu}(\gamma, n)$	0.16	0.02		$^{160}\text{Er}(\gamma, \alpha)$	-0.29	-0.09
^{115}Sn	$^{110}\text{Sn}(\gamma, p)$	-0.18	-0.02		$^{161}\text{Er}(\gamma, n)$	0.18	0.06
	$^{110}\text{Sn}(\gamma, \alpha)$	-0.27	-0.04		$^{166}\text{Yb}(\gamma, \alpha)$	0.40	0.12
	$^{113}\text{Sn}(\gamma, n)$	0.77	0.12		$^{196}\text{Pb}(\gamma, n)$	0.26	0.09
	$^{169}\text{Lu}(\gamma, n)$	0.16	0.02		$^{202}\text{Pb}(\gamma, n)$	0.15	0.05
^{120}Te	$^{119}\text{Te}(\gamma, n)$	-0.20	-0.04	^{164}Er	$^{164}\text{Yb}(\gamma, n)$	-0.23	-0.10
	$^{121}\text{Te}(\gamma, n)$	-0.66	-0.13		$^{164}\text{Yb}(\gamma, \alpha)$	-0.59	-0.43
	$^{122}\text{Xe}(\gamma, p)$	0.42	0.07		$^{165}\text{Yb}(\gamma, n)$	-0.17	-0.09
	$^{122}\text{Xe}(\gamma, \alpha)$	-0.35	-0.06		$^{196}\text{Pb}(\gamma, n)$	0.16	0.07
^{124}Xe	$^{122}\text{Xe}(\gamma, n)$	-0.22	-0.08	^{168}Yb	$^{168}\text{Hf}(\gamma, n)$	-0.16	-0.05
	$^{122}\text{Xe}(\gamma, p)$	-0.27	-0.10		$^{168}\text{Hf}(\gamma, \alpha)$	-0.40	-0.21
	$^{122}\text{Xe}(\gamma, \alpha)$	-0.44	-0.23		$^{169}\text{Hf}(\gamma, n)$	-0.17	-0.05
	$^{125}\text{Xe}(\gamma, n)$	-0.40	-0.22		$^{172}\text{Hf}(\gamma, \alpha)$	0.41	0.19
^{126}Xe	$^{122}\text{Xe}(\gamma, n)$	-0.21	-0.06		$^{196}\text{Pb}(\gamma, n)$	0.22	0.08
	$^{122}\text{Xe}(\gamma, p)$	-0.26	-0.08	^{174}Hf	$^{174}\text{W}(\gamma, n)$	-0.23	-0.06
	$^{122}\text{Xe}(\gamma, \alpha)$	-0.46	-0.19		$^{174}\text{W}(\gamma, \alpha)$	-0.52	-0.19
	$^{125}\text{Xe}(\gamma, n)$	0.38	0.16		$^{176}\text{W}(\gamma, \alpha)$	-0.15	-0.05
	$^{127}\text{Xe}(\gamma, n)$	-0.26	-0.11	^{180}Ta	$^{179}\text{Ta}(\gamma, n)$	-0.88	-0.03
^{130}Ba	$^{126}\text{Ba}(\gamma, p)$	-0.18	-0.02	^{180}W	$^{180}\text{Os}(\gamma, n)$	-0.30	-0.12
	$^{126}\text{Ba}(\gamma, \alpha)$	-0.31	-0.03		$^{180}\text{Os}(\gamma, \alpha)$	-0.54	-0.39
	$^{128}\text{Ba}(\gamma, n)$	-0.26	-0.03		$^{196}\text{Pb}(\gamma, n)$	0.21	0.08
	$^{128}\text{Ba}(\gamma, p)$	-0.16	-0.01	^{184}Os	$^{184}\text{Pt}(\gamma, \alpha)$	-0.49	-0.10
	$^{128}\text{Ba}(\gamma, \alpha)$	-0.27	-0.02		$^{185}\text{Pt}(\gamma, \alpha)$	-0.16	-0.02
	$^{129}\text{Ba}(\gamma, n)$	0.21	0.02		$^{196}\text{Pb}(\gamma, n)$	0.16	0.02
	$^{131}\text{Ba}(\gamma, n)$	-0.51	-0.05	^{190}Pt	$^{190}\text{Hg}(\gamma, n)$	-0.27	-0.06
^{132}Ba	$^{128}\text{Ba}(\gamma, \alpha)$	-0.18	-0.02		$^{190}\text{Hg}(\gamma, \alpha)$	-0.52	-0.15
	$^{131}\text{Ba}(\gamma, n)$	0.63	0.12		$^{196}\text{Pb}(\gamma, n)$	0.18	0.04
	$^{133}\text{Ba}(\gamma, n)$	-0.56	-0.10	^{196}Hg	$^{196}\text{Pb}(\gamma, n)$	-0.75	-0.53
^{138}La	$^{137}\text{La}(\gamma, n)$	-0.65	-0.35		$^{202}\text{Pb}(\gamma, n)$	0.20	0.12
^{136}Ce	$^{138}\text{Nd}(\gamma, n)$	-0.39	-0.06				
	$^{138}\text{Nd}(\gamma, p)$	0.65	0.10				
	$^{138}\text{Nd}(\gamma, \alpha)$	-0.16	-0.03				
	$^{140}\text{Nd}(\gamma, \alpha)$	0.31	0.05				

Table 2.7: Correlations and ζ slopes between mass fraction and reaction rates for the $50 \times 3D$ -inspired mixing scenario.

Isotope	Reaction	r_P	ζ	Isotope	Reaction	r_P	ζ	
⁷⁴ Se	⁷⁵ Se(γ, n)	-0.95	-0.10	¹³⁰ Ba	¹²⁶ Ba(γ, α)	-0.19	-0.01	
⁷⁸ Kr	⁷⁹ Kr(γ, n)	-0.91	-0.28		¹³² Ce(γ, n)	-0.23	-0.01	
⁸⁴ Sr	⁸⁵ Sr(γ, n)	-0.92	-0.26		¹³² Ce(γ, p)	0.32	0.01	
⁹² Mo	⁹³ Mo(γ, n)	-0.57	-0.03		¹³² Ce(γ, α)	-0.20	-0.01	
	¹⁰⁰ Pd(γ, p)	0.19	0.01		¹³⁴ Ce(γ, n)	-0.20	-0.01	
	¹⁰⁰ Pd(γ, α)	0.20	0.01		¹³⁴ Ce(γ, α)	0.41	0.02	
	¹¹⁰ Sn(γ, n)	0.16	0.01		¹³² Ce(γ, n)	-0.28	-0.04	
	¹¹⁰ Sn(γ, p)	0.23	0.01		¹³² Ce(γ, p)	-0.25	-0.03	
	¹¹⁰ Sn(γ, α)	0.37	0.02		¹³² Ce(γ, α)	-0.31	-0.04	
	⁹³ Mo(γ, n)	0.89	0.08		¹³³ Ce(γ, n)	-0.19	-0.03	
	⁹⁷ Ru(γ, n)	-0.62	-0.05		¹³⁴ Ce(γ, α)	-0.18	-0.02	
	⁹⁷ Ru(γ, α)	-0.18	-0.01		¹³⁷ La(γ, n)	-0.75	-0.45	
	¹⁰⁰ Pd(γ, α)	0.33	0.03		¹³⁶ Ce	¹³⁸ Nd(γ, n)	-0.42	-0.09
⁹⁴ Mo	¹¹⁰ Sn(γ, n)	0.16	0.01		¹³⁸ Nd(γ, p)	0.66	0.14	
	¹¹⁰ Sn(γ, p)	0.16	0.01		¹⁴⁰ Nd(γ, α)	0.25	0.06	
	¹¹⁰ Sn(γ, α)	0.23	0.02		¹³⁸ Nd(γ, n)	-0.33	-0.04	
	¹⁰⁰ Pd(γ, p)	0.70	0.13		¹³⁸ Nd(γ, p)	-0.31	-0.04	
	¹⁰⁰ Pd(γ, α)	-0.53	-0.10		¹³⁸ Nd(γ, α)	-0.24	-0.02	
	¹⁰⁰ Pd(γ, p)	-0.39	-0.06		¹³⁹ Nd(γ, n)	-0.31	-0.04	
	¹⁰⁰ Pd(γ, α)	-0.38	-0.05		¹⁴² Sm(γ, n)	-0.36	-0.06	
	¹⁰³ Pd(γ, n)	-0.23	-0.04		¹⁴² Sm(γ, p)	-0.29	-0.04	
	¹⁰⁴ Cd(γ, p)	0.17	0.03		¹⁴³ Sm(γ, n)	-0.50	-0.09	
	¹⁰⁴ Cd(γ, α)	-0.27	-0.04		¹⁹⁶ Pb(γ, n)	0.19	0.03	
¹⁰⁶ Cd	¹⁰⁴ Cd(γ, p)	-0.23	-0.03		¹⁵² Gd	¹⁵² Dy(γ, α)	-0.50	-0.05
	¹⁰⁷ Cd(γ, n)	-0.62	-0.07		¹⁵⁸ Er(γ, n)	0.18	0.01	
	¹¹⁰ Sn(γ, p)	0.20	0.02		¹⁵⁶ Dy	¹⁵⁶ Er(γ, α)	-0.44	-0.27
	¹¹⁰ Sn(γ, α)	0.40	0.05		¹⁵⁸ Er(γ, n)	0.19	0.09	
	¹⁰⁷ Cd(γ, n)	0.61	0.11		¹⁵⁸ Er(γ, α)	-0.18	-0.07	
	¹¹⁰ Sn(γ, p)	0.49	0.08		¹⁶⁰ Er(γ, α)	0.25	0.15	
	¹¹⁰ Sn(γ, α)	-0.33	-0.06		¹⁵⁸ Er(γ, n)	-0.28	-0.02	
	¹¹³ In	¹¹³ Sn(γ, n)	0.94	0.44	¹⁵⁸ Er(γ, α)	-0.53	-0.05	
	¹¹² Sn	¹¹⁰ Sn(γ, p)	-0.25	-0.03	¹⁶² Er	¹⁶² Yb(γ, α)	-0.49	-0.30
	¹¹³ Sn(γ, α)	-0.34	-0.04	¹⁶⁴ Er	¹⁶⁴ Yb(γ, n)	-0.17	0.07	
¹¹⁴ Sn	¹¹³ Sn(γ, n)	-0.65	-0.08	¹⁶⁸ Hf	¹⁶⁸ Hf(γ, n)	0.17	0.07	
	¹¹⁰ Sn(γ, α)	-0.21	-0.02	¹⁶⁴ Er	¹⁶⁴ Yb(γ, n)	-0.31	-0.17	
	¹¹³ Sn(γ, n)	0.78	0.08	¹⁶⁴ Er	¹⁶⁴ Yb(γ, α)	-0.56	-0.51	
	¹²² Xe(γ, n)	-0.28	-0.03	²⁰² Pb	¹⁶⁸ Hf(γ, n)	-0.28	-0.12	
	¹²² Xe(γ, p)	0.16	0.02	¹⁶⁸ Yb	¹⁶⁸ Hf(γ, α)	-0.55	-0.57	
	¹²² Xe(γ, α)	0.23	0.03	¹⁷⁴ Hf	¹⁷⁴ W(γ, n)	-0.30	-0.13	
	¹⁶⁹ Lu(γ, n)	0.15	0.01	¹⁷⁴ W	¹⁷⁴ W(γ, α)	-0.53	-0.37	
	¹¹⁰ Sn(γ, α)	-0.21	-0.02	¹⁸⁰ Ta	¹⁷⁹ Ta(γ, n)	-0.87	-0.00	
	¹¹³ Sn(γ, n)	0.80	0.08	¹⁸⁰ W	¹⁸⁰ Os(γ, n)	-0.38	-0.21	
	¹²² Xe(γ, n)	-0.27	-0.03	¹⁸⁰ Os	¹⁸⁰ Os(γ, α)	-0.52	-0.46	
¹²⁰ Te	¹²² Xe(γ, p)	0.15	0.02	¹⁹⁶ Pb	¹⁹⁶ Pb(γ, n)	0.19	0.11	
	¹²² Xe(γ, α)	0.22	0.03	¹⁸⁴ Os	¹⁸⁴ Pt(γ, n)	-0.16	-0.05	
	¹⁶⁹ Lu(γ, n)	0.15	0.01	¹⁸⁴ Pt	¹⁸⁴ Pt(γ, α)	-0.55	-0.29	
	¹²⁰ Xe(γ, α)	-0.22	-0.05	¹⁹⁶ Pb	¹⁹⁶ Pb(γ, n)	0.16	0.04	
	¹²² Xe(γ, p)	0.58	0.11	¹⁹⁰ Pt	¹⁹⁰ Hg(γ, n)	-0.30	-0.13	
	¹²² Xe(γ, α)	-0.49	-0.10	¹⁹⁰ Hg	¹⁹⁰ Hg(γ, α)	-0.49	-0.30	
	¹²² Xe(γ, n)	-0.28	-0.10	¹⁹⁶ Hg	¹⁹⁶ Pb(γ, n)	0.20	0.08	
	¹²² Xe(γ, p)	-0.31	-0.11	¹⁹⁶ Pb	¹⁹⁶ Pb(γ, n)	-0.76	-0.60	
	¹²² Xe(γ, α)	-0.43	-0.21	²⁰² Pb	²⁰² Pb(γ, n)	0.18	0.11	
	¹²³ Xe(γ, n)	0.18	0.06					
¹²⁶ Xe	¹²⁶ Ba(γ, p)	-0.35	-0.17					
	¹²⁶ Ba(γ, α)	-0.48	-0.32					
	¹²⁷ Ba(γ, n)	-0.22	-0.12					

to the presence of a convective downturn and mixing speeds of that downturn in a way that is both non-linear and non-monotonic both globally and for specific isotopes, and that the ratio of isotopic pairs is found to be dependent on the mixing details. We also demonstrate why a O-C shell merger is necessary produce these isotopes in a pre-explosive context and how the ingestion rate boosts production. Similarly, we show how the presence of a dip in the diffusion profile with either a GOSH-like dip or partial merger decrease the production of p-nuclei and how the deeper location of the GOSH-like dip is more effective at lowering production. Finally, we show how varying the input nuclear physics causes a spread in the production of the p-nuclei, but that the specific details of how much a particular isotope is affected by that depends on mixing scenario. In addition, the reaction rates that are relevant for the production of the p-nuclei are found depend on the mixing scenario. Figure 2.22 shows the maximum and minimum impact to the production on the p-nuclei due to the various mixing scenarios and across all these cases the average spread is 2.45 dex.

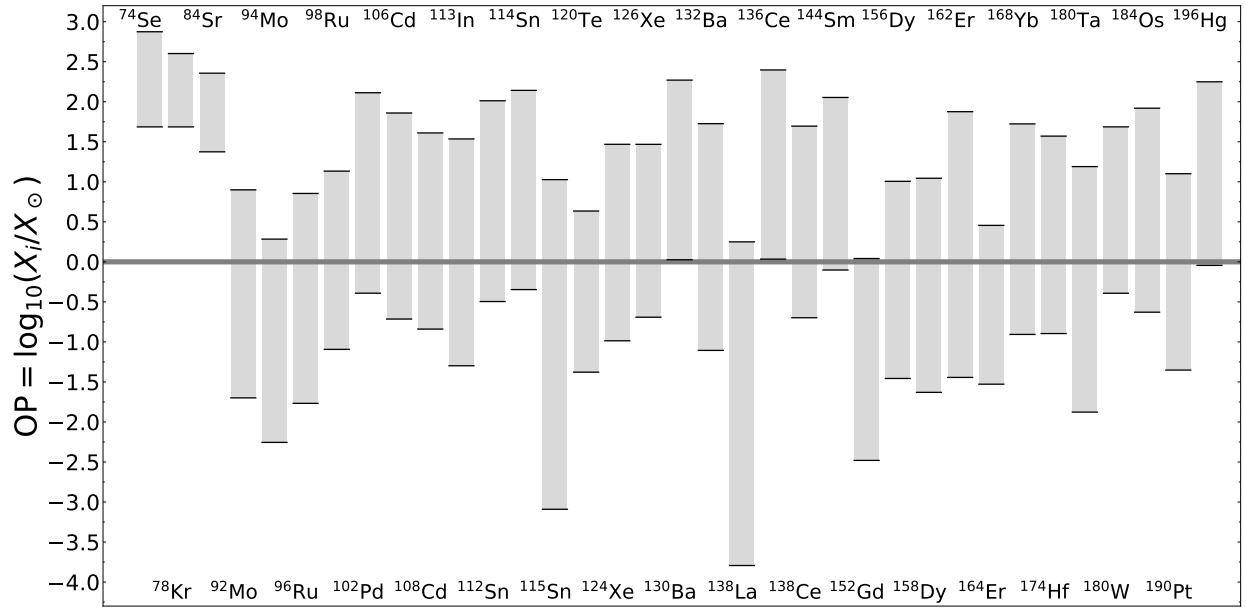


Figure 2.22: Maximum and minimum overproduction compared to solar for all convective downturn scenarios, GOSH-like scenarios, partial merger scenarios, and ingestion rates excluding the scenario of no C-shell ingestion. The thick grey line at $\text{OP} = 0$ corresponds to the solar measurement. The average spread in production is 2.45 dex.

These results have a similar variation in final production for the p-nuclei as found by Rauscher et al. (2016) when determining the uncertainties from nuclear physics inputs. The $15M_{\odot}$ KEPLER model they analyze had an average uncertainty of 0.61 for the 90% probability from varying of the nuclear physics. This is lower than this study which finds an

average maximum spread of $3.6 - 6.2$ depending on the mixing case, but it is comparing 90% probability to maximum. They also find key rates correlated with the production of p-nuclei, of which some are shared in this study and others are not.

This work raises the importance of considering the limitations of mixing length theory for the nucleosynthesis of this 3-D hydrodynamic effect. As shown by Rizzuti et al. (2024a) the nucleosynthesis in 3-D simulations does not match 1-D. There remains more work to be done in analyzing the unique nucleosynthesis during O-C shell mergers and its greater relevance to observations and galactic chemical evolution (GCE) both for the p-nuclei and beyond. Ritter et al. (2018a) found in analyzing this model that there was an enhancement in the production of ^{31}P , ^{35}Cl , ^{39}K , and ^{45}Sc during the O-C shell merger which could account for their underproduction in GCE models. This has been confirmed to be a robust result across metallicity and stellar evolution model as shown by Roberti et al. (2025). Recent observations have found P-enhanced stars (Masseron et al., 2020; Brauner et al., 2023, 2024) which could be explained by O-C shell merger, although this analysis has not been done. There is also the general increase of O-burning ashes and decrease of C-shell ashes during the merger (Roberti et al., 2025), and if O-C shell mergers occurs in a significant fraction of massive stars then there will be a noticeable GCE impact.

There are also implications this work has on those interpreting the source of presolar grains. Fok et al. (2024) argues that the nucleosynthesis in O-C shell mergers needs to be more closely analyzed because they matter when interpreting the $^{29}\text{Si}/^{28}\text{Si}$ ratio. As the mixing uncertainties show, there are more significant modelling concerns that need to be addressed when considering how O-C shell mergers may contribute presolar grains. As shown in this work, the ratio of p-isotope pairs is sensitive to whether there is a convective downturn and the speed of the convective velocities in the O-shell. Comparing measurements of meteorite grains data (Hynes and Gyngard, 2009; Stephan et al., 2024a,b) with the results from this paper, we find no single mixing scenario can explain isotopic grains data. Figure 2.23 shows that Mo grains can be explained by the 3D-inspired scenario with an ingestion rate of $4 \times 10^{-3} M_{\odot}\text{s}^{-1}$ and $4 \times 10^{-4} M_{\odot}\text{s}^{-1}$ as well as 3×3 D-inspired scenario with an ingestion rate of $4 \times 10^{-3} M_{\odot}\text{s}^{-1}$ with the MLT, GOSH-like, and partial merger cases close to the measurements. However, as Figure 2.24 shows, the faster $10\times$ and $50\times$ 3D-inspired cases better match the Ru grains despite the minimal data. Additionally, although not shown, the $\delta(^{130}\text{Ba}/^{136}\text{Ba})$ and $\delta(^{132}\text{Ba}/^{136}\text{Ba})$ does not match any mixing scenario. Although there are limitations to comparing the pre-explosive results from the O-shell alone, it does highlight how grains data can constrain the results of 3-D hydrodynamic simulations.

This work also raises the importance of considering the mixing details in the astrophysical

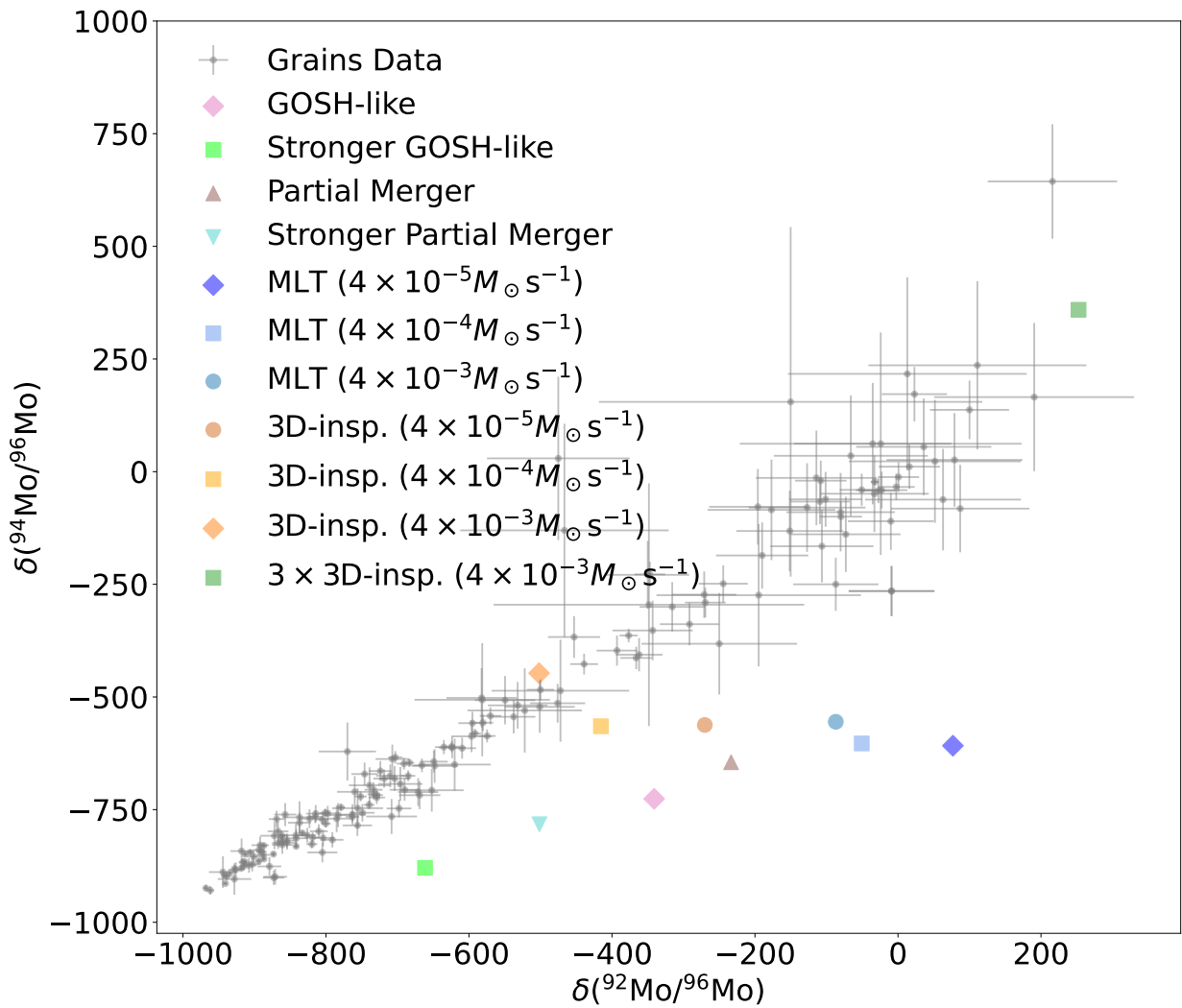


Figure 2.23: Comparing the results of the grains data to the various mixing scenarios considered in this paper for $\delta(^{92}\text{Mo}/^{96}\text{Mo})$ and $\delta(^{94}\text{Mo}/^{96}\text{Mo})$. Grey points correspond to grains data with 1σ error bars and coloured points for the mixing scenarios.

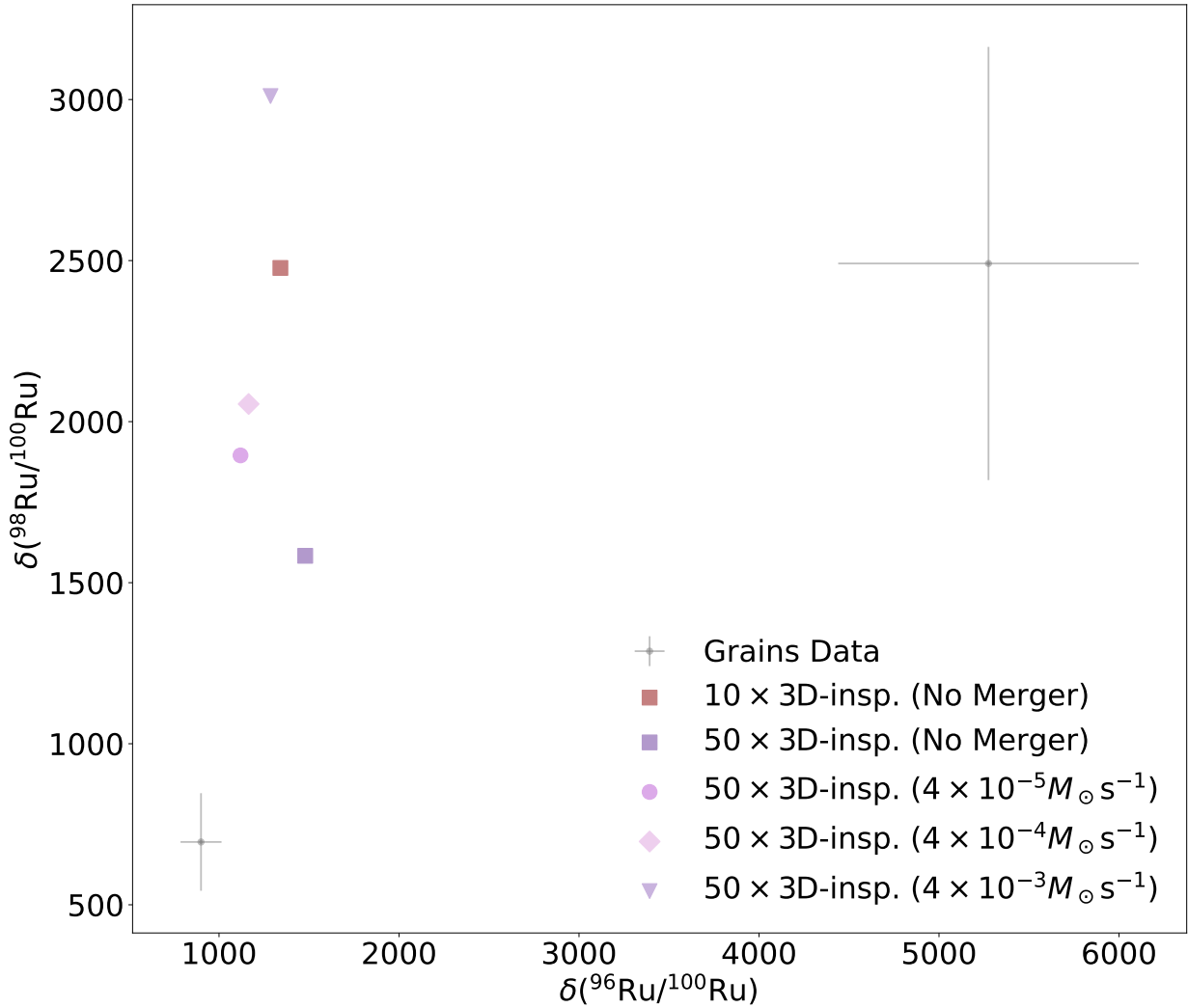


Figure 2.24: Comparing the results of the grains data to the various mixing scenarios considered in this paper for $\delta(^{98}\text{Ru}/^{100}\text{Ru})$ and $\delta(^{96}\text{Ru}/^{100}\text{Ru})$. Grey points correspond to grains data with 1σ error bars and coloured points for the mixing scenarios.

site when providing nuclear reaction rates for experiment proposals. Whether one identifies a reaction as important to the production of one of the p-nuclei, the strength of that importance, and whether it is a branching pathways leading to a bifurcation in the final distribution are all dependent on the mixing. This points to the need for greater attention to 1-D stellar modelling as a basis for nuclear physics experimental proposals.

There are limitations to the results in this work and further extentionts that could be done. We have focused on the impact of mixing and nuclear physics, but there remains open questions about the impact of ingested stable seeds from the C-shell. As shown in Travaglio et al. (2015) and Battino et al. (2020), the *s*-, *i*-, and *r*-seeds has an important role in the production of the p-nuclei. This work shows that the ingestion of the C-shell seeds matter, and that the important reaction pathways depend on mixing speed, but there could be work to identify the specific seeds for each isotope, how that is dependent on mixing case, and if modifications of those seeds via the weak *s*-process earlier in the C-burning shell (Pignatari et al., 2010). It is also unclear whether the mixing dependency will be seen as strongly in the O-shell mergers of other models that have different temperature profiles and O-shell sizes. Selection of the NuGrid $15M_{\odot}$, $Z = 0.02$ model could be overemphasizing the impact of these results as of the four NuGrid models with O-C shell mergers it has the largest overproduction factor (Ritter et al., 2018a), although the other models are $Z = 0.01$ and seeds do play a role. Another open question is how the nucleosynthesis will behave with a dynamic stellar structure as this work holds it static. There are also some limitations in this work as the MPPNP nuclear network does not include isomeric states which means that ^{180m}Ta cannot be produced and it could be that the production mechanisms for ^{113}In and ^{115}Sn are potentially limited (Dillmann et al., 2008). Finally, these results are calculated for pre-CCSN conditions and should be run through explosive nucleosynthesis to determine the full impact of O-C shell merger nucleosynthesis as 10 – 40% of the p-nuclei isotopes occur during explosive nucleosynthesis even with an O-C shell merger (Roberti et al., 2023).

2.6 Conclusion

This study has demonstrated how O-C shell mergers in massive stars are an astrophysical site for the production of the p-nuclei via the γ -process. By analyzing 1-D post-processing nucleosynthesis calculations that incorporate the results of 3-D hydrodynamic simulations, we find that there is significant uncertainty in the production of p-nuclei when considering different mixing scenarios. We have demonstrated that understanding the mixing details of the O-burning shell are critical that the presence of a convective downturn present a non-

linear and non-monotonic effect, how production scales with the rate of ingestion, how dips in the convective profile decrease production, and that the impact that nuclear physics can has is sensitive to mixing details. This is not to suggest that all of these mixing scenarios are equally likely or could happen, but how the lack of correspondence from 3-D hydrodynamics impacts nucleosynthesis. Since the O-C shell merger is critical to the nucleosynthesis of a massive star prior to the CCSN regardless of explosive energy (Roberti et al., 2024), we emphasize the importance of these model uncertainties of the mixing scenario of O-shell burning and O-C shell mergers.

Chapter 3

Investigations Beyond the *p*-Nuclei

3.1 Light Odd-Z Isotope Production

The *p*-nuclei are not the sole unique nucleosynthetic feature of O-C shell mergers. The light odd-Z elements P, Cl, K, and Sc have all been noted as products as well Ritter et al. (2018a); Roberti et al. (2025). These elements are underproduced in galactic chemical evolution calculations (citation?) and there exist observations of P-enhanced stars that may be explained by this Masseron et al. (2020); Brauner et al. (2023, 2024).

Here, we will explore how the stable isotopes for these elements are produced in merger.

- I think I want that table that breaks down the nuclear physics impacts
- Maybe some nice figures also mimicing the paper figures

3.1.1 The Relevance of K

The production of K in particular is of interest due to its relevance in the formation of exoplanets and whether they have an Earth-like atmosphere habitable for life Frank et al. (2014); O'Neill et al. (2020).

We can investigate the K isotopes ^{39}K , ^{40}K , and ^{41}K more in detail.

3.2 Advective-Reactive *r*-process

Advective-reactive nucleosynthesis refers to the generic case where any mixing interaction timescale is similar to the reaction timescale. Here I present preliminary work done with Dr. Herwig analyzing a new scenario beyond the post-processed O-shell.

- do I have to mention that this work was done with Falk more directly

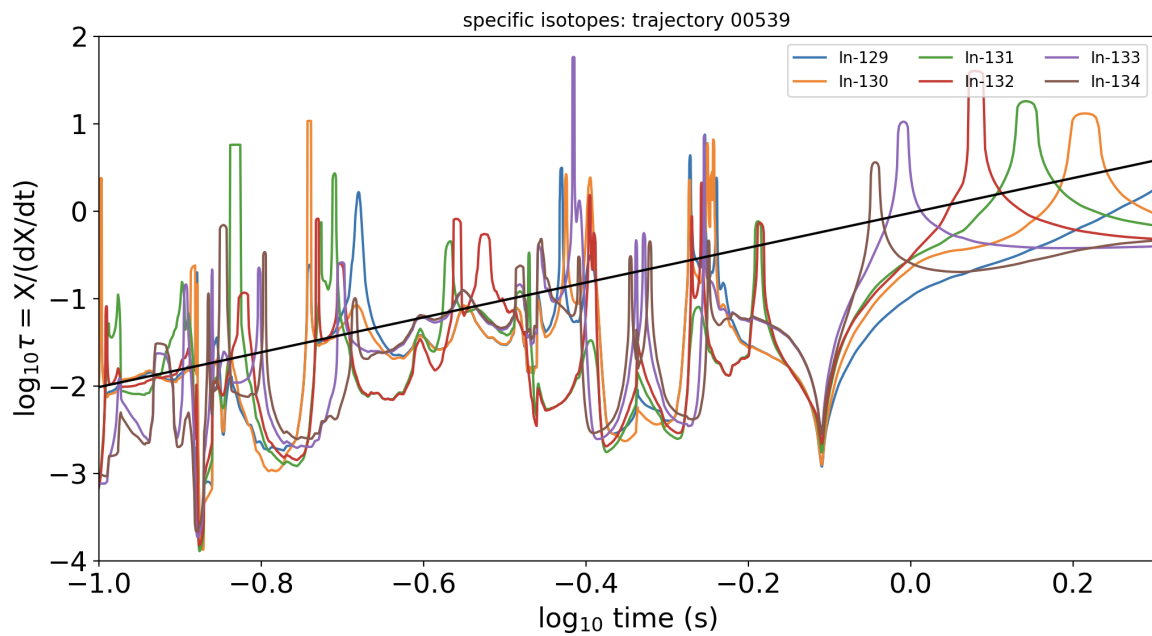


Figure 3.1: In isotope timescale.

- Rodrigo black hole paper?
- Work was done to estimate both the mixing and nuclear timescale
- Basically found the fraction of trajectories where exchanging mass occurs on the a-r timescale.
- How many freaking r-process papers do I really need to cite here

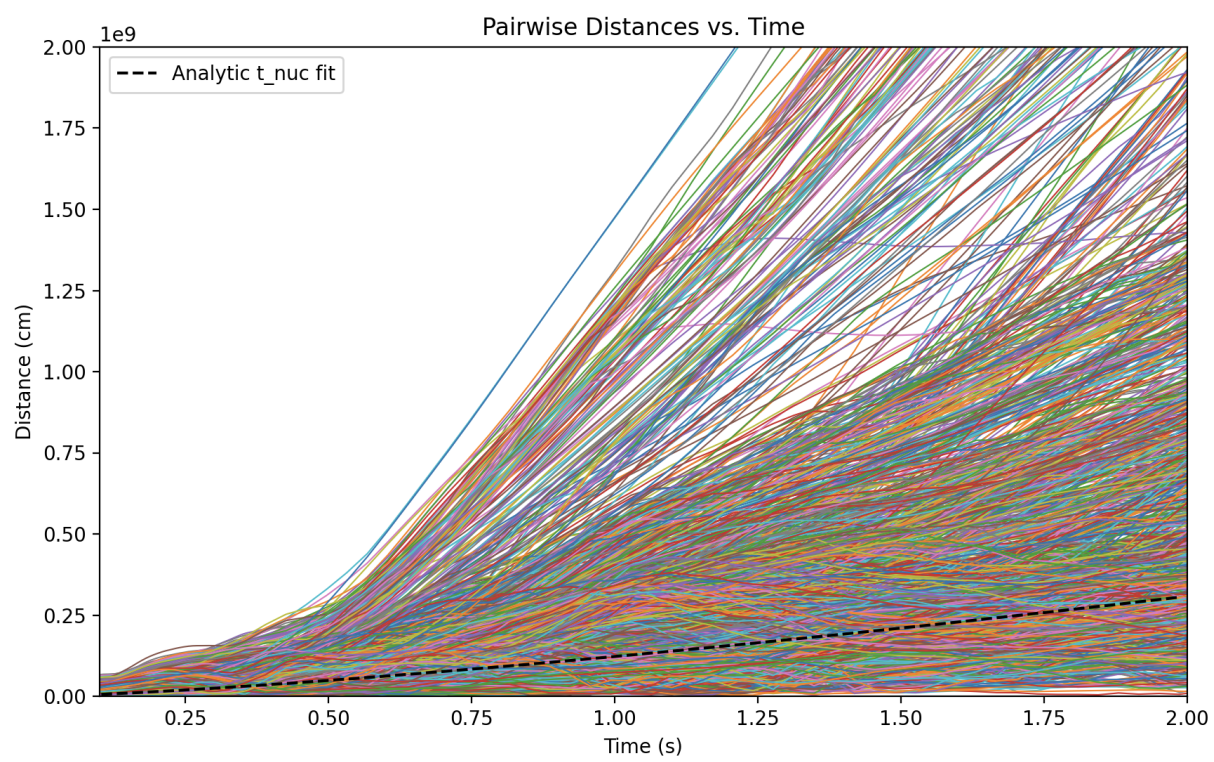


Figure 3.2: Pairwise distance.

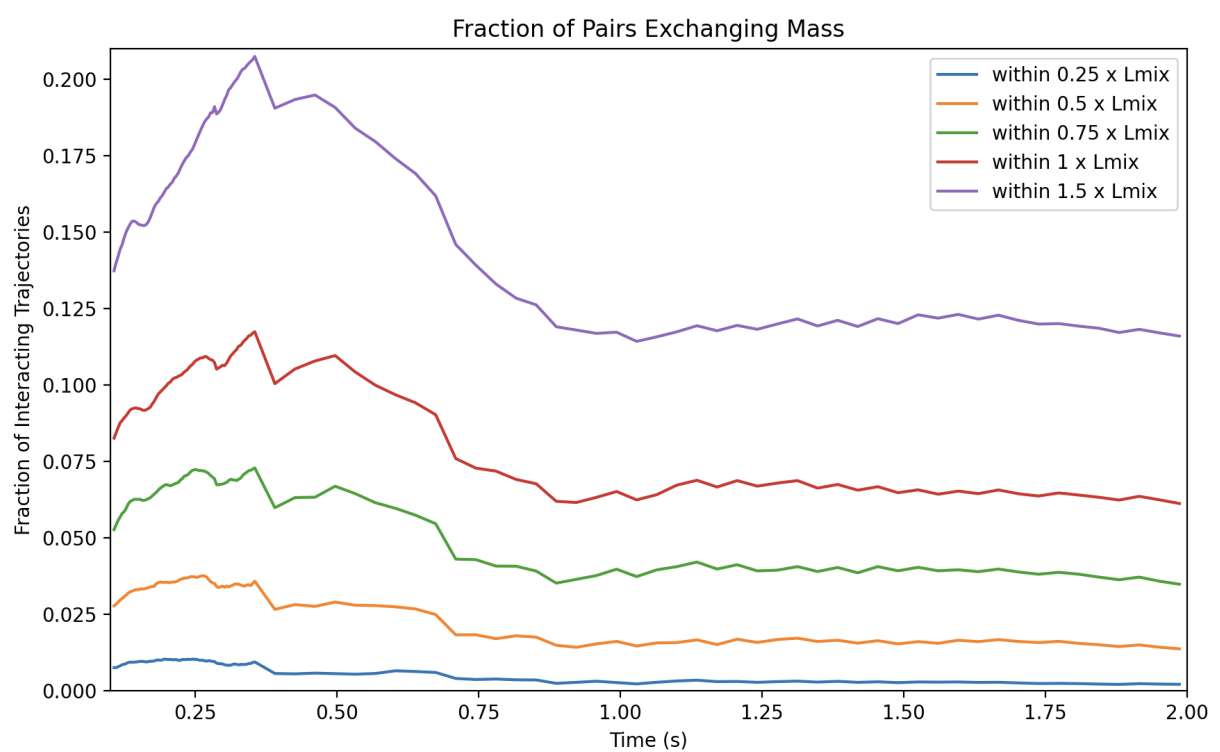


Figure 3.3: Fraction of exchanging mass.

Chapter 4

Summary and Conclusion

The conclusion

Bibliography

- Andrassy, R., Herwig, F., Woodward, P., and Ritter, C. (2020). 3D hydrodynamic simulations of C ingestion into a convective O shell. *Monthly Notices of the Royal Astronomical Society*, 491:972–992.
- Arcones, A. and Montes, F. (2011). Production of Light-element Primary Process Nuclei in Neutrino-driven Winds. *The Astrophysical Journal*, 731:5.
- Arnett, W. D., Meakin, C., Hirschi, R., Cristini, A., Georgy, C., Campbell, S., Scott, L. J. A., Kaiser, E. A., Viallet, M., and Mocák, M. (2019). 3D Simulations and MLT. I. Renzini’s Critique. *The Astrophysical Journal*, 882:18.
- Arnould, M. (1976). Possibility of synthesis of proton-rich nuclei in highly evolved stars. II. *Astronomy and Astrophysics*, 46:117–125.
- Arnould, M. and Goriely, S. (2003). The p-process of stellar nucleosynthesis: Astrophysics and nuclear physics status. *Physics Reports*, 384(1):1–84.
- Battino, U., Pignatari, M., Travaglio, C., Lederer-Woods, C., Denissenkov, P., Herwig, F., Thielemann, F., and Rauscher, T. (2020). Heavy elements nucleosynthesis on accreting white dwarfs: Building seeds for the p-process. *Monthly Notices of the Royal Astronomical Society*, 497:4981–4998.
- Battino, U., Tattersall, A., Lederer-Woods, C., Herwig, F., Denissenkov, P., Hirschi, R., Trappitsch, R., den Hartogh, J. W., Pignatari, M., and NuGrid Collaboration (2019). NuGrid stellar data set - III. Updated low-mass AGB models and s-process nucleosynthesis with metallicities $Z = 0.01$, $Z = 0.02$, and $Z = 0.03$. *Monthly Notices of the Royal Astronomical Society*, 489:1082–1098.
- Bazan, G. and Arnett, D. (1994). Convection, Nucleosynthesis, and Core Collapse. *The Astrophysical Journal*, 433:L41.

- Bisterzo, S., Gallino, R., Straniero, O., Cristallo, S., and Käppeler, F. (2011). The s-process in low-metallicity stars - II. Interpretation of high-resolution spectroscopic observations with asymptotic giant branch models. *Monthly Notices of the Royal Astronomical Society*, 418:284–319.
- Böhm-Vitense, E. (1958). Über die Wasserstoffkonvektionszone in Sternen verschiedener Effektivtemperaturen und Leuchtkräfte. Mit 5 Textabbildungen. *Zeitschrift für Astrophysik*, 46:108.
- Brauner, M., Masseron, T., García-Hernández, D. A., Pignatari, M., Womack, K. A., Lugaro, M., and Hayes, C. R. (2023). Unveiling the chemical fingerprint of phosphorus-rich stars: I. In the infrared region of APOGEE-2. *Astronomy & Astrophysics*, 673:A123.
- Brauner, M., Pignatari, M., Masseron, T., García-Hernández, D. A., and Lugaro, M. (2024). Unveiling the chemical fingerprint of phosphorus-rich stars II. Heavy-element abundances from UVES/VLT spectra.
- Burbidge, E. M., Burbidge, G. R., Fowler, W. A., and Hoyle, F. (1957). Synthesis of the Elements in Stars. *Reviews of Modern Physics*, 29(4):547–650.
- Collins, C., Müller, B., and Heger, A. (2018). Properties of convective oxygen and silicon burning shells in supernova progenitors. *Monthly Notices of the Royal Astronomical Society*, 473:1695–1704.
- Cox, J. P. and Giuli, R. T. (1968). *Principles of Stellar Structure*. Gordon and Breach Science Publishers.
- Denissenkov, P., Perdikakis, G., Herwig, F., Schatz, H., Ritter, C., Pignatari, M., Jones, S., Nikas, S., and Spyrou, A. (2018). The impact of (n, γ) reaction rate uncertainties of unstable isotopes near $N = 50$ on the i-process nucleosynthesis in He-shell flash white dwarfs. *Journal of Physics G Nuclear Physics*, 45:055203.
- Denissenkov, P. A., Herwig, F., Perdikakis, G., and Schatz, H. (2021). The impact of (n, γ) reaction rate uncertainties of unstable isotopes on the i-process nucleosynthesis of the elements from Ba to W. *Monthly Notices of the Royal Astronomical Society*, 503:3913–3925.
- Dillmann, I., Rauscher, T., Heil, M., Käppeler, F., Rapp, W., and Thielemann, F. K. (2008). P-Process simulations with a modified reaction library. *Journal of Physics G Nuclear Physics*, 35:014029.

- Fok, H. K., Pignatari, M., Côté, B., and Trappitsch, R. (2024). Silicon Isotopic Composition of Mainstream Presolar SiC Grains Revisited: The Impact of Nuclear Reaction Rate Uncertainties. *The Astrophysical Journal*, 977:L24.
- Frank, E. A., Meyer, B. S., and Mojzsis, S. J. (2014). A radiogenic heating evolution model for cosmochemically Earth-like exoplanets. *Icarus*, 243:274–286.
- Fröhlich, C., Martínez-Pinedo, G., Liebendörfer, M., Thielemann, F. K., Bravo, E., Hix, W. R., Langanke, K., and Zinner, N. T. (2006). Neutrino-Induced Nucleosynthesis of A>64 Nuclei: The Np Process. *Physical Review Letters*, 96:142502.
- Goriely, S., Arnould, M., Borzov, I., and Rayet, M. (2001). The puzzle of the synthesis of the rare nuclide ^{138}La . *Astronomy and Astrophysics*, 375:L35–L38.
- Goriely, S., José, J., Hernanz, M., Rayet, M., and Arnould, M. (2002). He-detonation in sub-Chandrasekhar CO white dwarfs: A new insight into energetics and p-process nucleosynthesis. *Astronomy and Astrophysics*, 383:L27–L30.
- Grevesse, N. and Noels, A. (1994). Atomic data and solar and stellar spectroscopy. *Physica Scripta Volume T*, 51:47–50.
- Henyey, L. G., Forbes, J. E., and Gould, N. L. (1964). A New Method of Automatic Computation of Stellar Evolution. *The Astrophysical Journal*, 139:306.
- Herwig, F. (2023). Astr 501: Stellar interiors. Lecture notes, University of Victoria.
- Herwig, F., Pignatari, M., Woodward, P. R., Porter, D. H., Rockefeller, G., Fryer, C. L., Bennett, M., and Hirschi, R. (2011). CONVECTIVE–REACTIVE PROTON– ^{12}C COMBUSTION IN SAKURAI’S OBJECT (V4334 SAGITTARII) AND IMPLICATIONS FOR THE EVOLUTION AND YIELDS FROM THE FIRST GENERATIONS OF STARS. *The Astrophysical Journal*, 727(2):89.
- Herwig, F., Woodward, P. R., Lin, P.-H., Knox, M., and Fryer, C. (2014). GLOBAL NON-SPHERICAL OSCILLATIONS IN THREE-DIMENSIONAL 4π SIMULATIONS OF THE H-INGESTION FLASH. *The Astrophysical Journal Letters*, 792(1):L3.
- Hynes, K. M. and Gyngard, F. (2009). The Presolar Grain Database: <http://presolar.wustl.edu/~pgd>. In *40th Annual Lunar and Planetary Science Conference*, page 1198.

- Jones, S., Andrassy, R., Sandalski, S., Davis, A., Woodward, P., and Herwig, F. (2017). Idealized hydrodynamic simulations of turbulent oxygen-burning shell convection in 4π geometry. *Monthly Notices of the Royal Astronomical Society*, 465:2991–3010.
- Joyce, M. and Tayar, J. (2023). A Review of the Mixing Length Theory of Convection in 1D Stellar Modeling. *Galaxies*, 11(3):75.
- Kippenhahn, R., Weigert, A., and Weiss, A. (2013). *Stellar Structure and Evolution*. Springer.
- Langer, N., El Eid, M. F., and Fricke, K. J. (1985). Evolution of massive stars with semi-convective diffusion. *Astronomy and Astrophysics*, 145:179–191.
- Masseron, T., García-Hernández, D. A., Santoveña, R., Manchado, A., Zamora, O., Man-teiga, M., and Dafonte, C. (2020). Phosphorus-rich stars with unusual abundances are challenging theoretical predictions. *Nature Communications*, 11:3759.
- Meakin, C. A. and Arnett, D. (2006). Active Carbon and Oxygen Shell Burning Hydrodynamics. *The Astrophysical Journal*, 637:L53–L56.
- Meakin, C. A. and Arnett, D. (2007). Turbulent Convection in Stellar Interiors. I. Hydrodynamic Simulation. *The Astrophysical Journal*, 667:448–475.
- Müller, B. (2016). The Status of Multi-Dimensional Core-Collapse Supernova Models. *Publications of the Astronomical Society of Australia*, 33:e048.
- Müller, B. (2020). Hydrodynamics of core-collapse supernovae and their progenitors. *Living Reviews in Computational Astrophysics*, 6:3.
- O'Neill, C., Lowman, J., and Wasiliev, J. (2020). The effect of galactic chemical evolution on terrestrial exoplanet composition and tectonics. *Icarus*, 352:114025.
- Paxton, B., Bildsten, L., Dotter, A., Herwig, F., Lesaffre, P., and Timmes, F. (2010). MODULES FOR EXPERIMENTS IN STELLAR ASTROPHYSICS (MESA). *The Astrophysical Journal Supplement Series*, 192(1):3.
- Pignatari, M., Gallino, R., Heil, M., Wiescher, M., Käppeler, F., Herwig, F., and Bis-terzo, S. (2010). THE WEAK s-PROCESS IN MASSIVE STARS AND ITS DEPENDENCE ON THE NEUTRON CAPTURE CROSS SECTIONS. *The Astrophysical Journal*, 710(2):1557.

- Pignatari, M., Göbel, K., Reifarth, R., and Travaglio, C. (2016a). The production of proton-rich isotopes beyond iron: The γ -process in stars. *International Journal of Modern Physics E*, 25(04):1630003.
- Pignatari, M., Herwig, F., Hirschi, R., Bennett, M., Rockefeller, G., Fryer, C., Timmes, F. X., Ritter, C., Heger, A., Jones, S., Battino, U., Dotter, A., Trappitsch, R., Diehl, S., Frischknecht, U., Hungerford, A., Magkotsios, G., Travaglio, C., and Young, P. (2016b). NuGrid Stellar Data Set. I. Stellar Yields from H to Bi for Stars with Metallicities $Z = 0.02$ and $Z = 0.01$. *The Astrophysical Journal Supplement Series*, 225:24.
- Prandtl, L. (1925). 7. Bericht über Untersuchungen zur ausgebildeten Turbulenz. *ZAMM - Journal of Applied Mathematics and Mechanics / Zeitschrift für Angewandte Mathematik und Mechanik*, vol. 5, issue 2, pp. 136-139, 5(2):136.
- Prialnik, D. (2009). *An Introduction to the Theory of Stellar Structure and Evolution*. Cambridge University Press.
- Rauscher, T., Dauphas, N., Dillmann, I., Fröhlich, C., Fülop, Z., and Gyürky, G. (2013). Constraining the astrophysical origin of the p-nuclei through nuclear physics and meteoritic data. *Reports on Progress in Physics*, 76(6):066201.
- Rauscher, T., Heger, A., Hoffman, R. D., and Woosley, S. E. (2002). Nucleosynthesis in Massive Stars with Improved Nuclear and Stellar Physics. *The Astrophysical Journal*, 576:323–348.
- Rauscher, T., Nishimura, N., Hirschi, R., Cescutti, G., Murphy, A. St. J., and Heger, A. (2016). Uncertainties in the production of p nuclei in massive stars obtained from Monte Carlo variations. *Monthly Notices of the Royal Astronomical Society*, 463(4):4153–4166.
- Rayet, M., Arnould, M., and Prantzos, N. (1990). The p-process revisited. *Astronomy and Astrophysics*, 227:271–281.
- Renzini, A. (1987). Some embarrassments in current treatments of convective overshooting. *Astronomy and Astrophysics*, 188:49–54.
- Ritter, C., Andrassy, R., Côté, B., Herwig, F., Woodward, P. R., Pignatari, M., and Jones, S. (2018a). Convective-reactive nucleosynthesis of K, Sc, Cl and p-process isotopes in O-C shell mergers. *Monthly Notices of the Royal Astronomical Society*, 474:L1–L6.

- Ritter, C., Herwig, F., Jones, S., Pignatari, M., Fryer, C., and Hirschi, R. (2018b). NuGrid stellar data set - II. Stellar yields from H to Bi for stellar models with MZAMS = 1-25 M \odot and Z = 0.0001-0.02. *Monthly Notices of the Royal Astronomical Society*, 480:538–571.
- Rizzuti, F., Hirschi, R., Varma, V., Arnett, W. D., Georgy, C., Meakin, C., Mocák, M., Murphy, A. S., and Rauscher, T. (2024a). Shell mergers in the late stages of massive star evolution: New insight from 3D hydrodynamic simulations. *Monthly Notices of the Royal Astronomical Society*, 533:687–704.
- Rizzuti, F., Hirschi, R., Varma, V., Arnett, W. D., Georgy, C., Meakin, C., Mocák, M., Murphy, A. S., and Rauscher, T. (2024b). Stellar Evolution and Convection in 3D Hydrodynamic Simulations of a Complete Burning Phase. *Galaxies*, 12:87.
- Robert, L., Pignatari, M., Brinkman, H. E., Jeena, S. K., Sieverding, A., Falla, A., Limongi, M., Chieffi, A., and Lugaro, M. (2025). The Occurrence and Impact of Carbon-Oxygen Shell Mergers in Massive Stars.
- Robert, L., Pignatari, M., Fryer, C., and Lugaro, M. (2024). The γ -process nucleosynthesis in core-collapse supernovae - II. Effect of the explosive recipe. *Astronomy & Astrophysics*, 686:L8.
- Robert, L., Pignatari, M., Psaltis, A., Sieverding, A., Mohr, P., Fülop, Zs., and Lugaro, M. (2023). The γ -process nucleosynthesis in core-collapse supernovae: I. A novel analysis of γ -process yields in massive stars. *Astronomy & Astrophysics*, 677:A22.
- Schatz, H., Aprahamian, A., Görres, J., Wiescher, M., Rauscher, T., Rembges, J. F., Thielemann, F. K., Pfeiffer, B., Möller, P., Kratz, K. L., Herndl, H., Brown, B. A., and Rebel, H. (1998). Rp-process nucleosynthesis at extreme temperature and density conditions. *Physics Reports*, 294(4):167–263.
- Sieverding, A., Martínez-Pinedo, G., Huther, L., Langanke, K., and Heger, A. (2018). The ν -Process in the Light of an Improved Understanding of Supernova Neutrino Spectra. *The Astrophysical Journal*, 865:143.
- Stephan, T., Davis, A. M., Gyngard, F., Hoppe, P., Hynes, K. M., Jadhav, M., Liu, N., Nittler, L. R., Ogiore, R. C., and Trappitsch, R. (2024a). The Presolar Grain Database Reloaded — Graphite. In *LPI Contributions*, volume 3036, page 6388.

- Stephan, T., Trappitsch, R., Hoppe, P., Davis, A. M., Bose, M., Boujibar, A., Gyngard, F., Hynes, K. M., Liu, N., Nittler, L. R., and Ogliore, R. C. (2024b). The Presolar Grain Database. I. Silicon Carbide. *The Astrophysical Journal Supplement Series*, 270:27.
- Travaglio, C., Gallino, R., Rauscher, T., Röpke, F. K., and Hillebrandt, W. (2015). Testing the Role of SNe Ia for Galactic Chemical Evolution of p-nuclei with Two-dimensional Models and with s-process Seeds at Different Metallicities. *The Astrophysical Journal*, 799:54.
- Travaglio, C., Röpke, F. K., Gallino, R., and Hillebrandt, W. (2011). Type Ia Supernovae as Sites of the p-process: Two-dimensional Models Coupled to Nucleosynthesis. *The Astrophysical Journal*, 739:93.
- Woosley, S. E. and Heger, A. (2007). Nucleosynthesis and remnants in massive stars of solar metallicity. *Physics Reports*, 442:269–283.
- Woosley, S. E., Heger, A., and Weaver, T. A. (2002). The evolution and explosion of massive stars. *Reviews of Modern Physics*, 74:1015–1071.
- Woosley, S. E. and Hoffman, R. D. (1992). The alpha -Process and the r-Process. *The Astrophysical Journal*, 395:202.
- Woosley, S. E. and Howard, W. M. (1978). The p-processes in supernovae. *The Astrophysical Journal Supplement Series*, 36:285–304.
- Xiong, Z., Martínez-Pinedo, G., Just, O., and Sieverding, A. (2024). Production of \$p\$ Nuclei from \$r\$-Process Seeds: The \$\nu_r\$ Process. *Physical Review Letters*, 132(19):192701.
- Yadav, N., Müller, B., Janka, H. T., Melson, T., and Heger, A. (2020). Large-scale Mixing in a Violent Oxygen–Neon Shell Merger Prior to a Core-collapse Supernova. *The Astrophysical Journal*, 890(2):94.